# NONLINEAR OPTICAL PROCESSES IN TWO-DIMENSIONAL SEMICONDUCTOR STRUCTURES

A Dissertation

by

YONGRUI WANG

Submitted to the Office of Graduate and Professional Studies of
Texas A&M University
in partial fulfillment of the requirements for the degree of

DOCTOR OF PHILOSOPHY

| | |
|---|---|
| Chair of Committee, | Alexey Belyanin |
| Committee Members, | Vitaly Kocharovsky |
| | Alexander Finkelstein |
| | Ohannes Eknoyan |
| Head of Department, | George Welch |

August 2015

Major Subject: Physics

ABSTRACT

The optical properties of two types of two-dimensional (2D) semiconductor structures are studied. One of them is for structures based on quantum wells (QWs), and the other is graphene.

We study the dynamics of optically excited electron-hole plasma or magneto-plasma in uncoupled QW structure. Experimentally we have observed a delayed burst of optical pulse, or superfluorescence (SF). Time and energy-resolved measurement shows the center frequency of the pulse is red-shifting with time. We explain this by developing the generalized semiconductor Bloch equations (SBEs), where Coulomb interaction between electrons is taken into account. For electron-hole plasma in quasi-equilibrium, the calculation shows the peak gain is near the Fermi-edge. So, the red-shifting is because of the decreasing of Fermi energy with time.

The effect of Coulomb interaction in intersubband transitions is also studied, where we have developed equations similar to the SBEs, and show that the Coulomb effect could enhance particular second-order nonlinear optical processes.

Quantum cascade lasers (QCLs) are well developed devices based on QWs. We study the active modulation in mid-infrared (mid-IR) QCLs. We show that QCLs with short gain recovery time can also generate short pulses by active modulation, while it is previously thought active modulation can only be applied for QCLs with long gain recovery time. Comparisons between the two cases show the performance of QCLs with short gain recovery time is more robust for active modulation. Also, mode-locking can be achieved by tuning the modulation period.

As a natural 2D material, graphene has linear energy dispersion near the Dirac

points. This leads to interesting electronic and optical properties. Under Landau quantization, we propose a scheme for achieving continuous-wave terahertz (THz) gain by mid-IR pumping. In this scheme, scattering of surface-optical (SO) phonons from the substrate is utilized to populate the upper laser state. All the important scattering processes are calculated to justify the design.

We also study the properties of second-harmonic generation (SHG) in graphene without magnetic field. The experimental measurement shows peculiar relations between the polarizations of fundamental light and second-harmonic (SH) light. We develop a quantum theory to explain the observations.

ACKNOWLEDGEMENTS

I would like to express my deep appreciation to Dr. Alexey Belyanin. He is enthusiastic about science, knowing wide range of knowledge, and with wisdom. During the research, we work side by side to solve problems. His patience and encouragement help to make the research enjoyable. Thank you for all your support and help. Your attitude to life is a great example for me to follow.

I also would like to thank my committee members, Dr. Vitaly Kocharovsky, Dr. Alexander Finkelstein, and Dr. Ohannes Eknoyan, for their guidance, interest, and time on my research. I have taken courses taught by Dr. Finkelstein and Dr. Eknoyan, from which I learned a lot about the basics of solid state physics, and properties of waveguides. Thank you for your teaching. Also, the collaboration with Dr. Kono has been a great experience, where interesting observations are studied together. And collaboration with Dr. Tokman has enlightened me a lot on the interaction between light and matters. Thanks go to both of them! Thanks also go to Dr. Yong-Hee Cho, Dr. Aleksander Wojcik, and Dr. Xianghan Yao for many helpful discussions.

Learning about physics at A&M is a great experience in my life. Physics courses I have taken have been taught by Dr. Allen, Dr. Pokrovsky, Dr. Becker, Dr. Chin, Dr. Pope, Dr. Finkel'stein, Dr. Zubairy, Dr. Ko, Dr. Hu, Dr. Belyanin, Dr. Keldysh, Dr. Hu, and Dr. Rapp. I would say, each course is a serious one. I have learned a lot from all these courses. Also, I have learned a lot of interesting stuff from professors in other departments, they are Dr. Zelenko, Dr. Hemmer, and Dr. Eknoyan. Thanks go to all these great teachers.

Also, I would like to thank all other faculty ans staff members in the Physics

department. The various activities in the department have made the time here very excited. And I would like to especially thank Dr. Kattawar for his guidance and support during my second year of study. Students in the department, especially those come in the same year as me, have made my time here full of happiness. Thank you for making the good memories.

Prior to entering A&M, I have been helped by a lot of teachers and classmates. Thank you all. I especially want to thank Dr. Tianjun Li, for his guidance in my research about high energy physics.

Finally, I would like to thank my wife, Xuezhen, and my Son, Yizhou. As a family, we have been encouraging each other, and life is good with you around. Also, thank my parents for your love, you are always the greatest ones. Thanks also go to other loved ones.

# NOMENCLATURE

| | |
|---|---|
| 2D | Two-dimensional |
| QW | Quantum Well |
| SF | Superfluorescence |
| QCL | Quantum Cascade Laser |
| SBEs | Semiconductor Bloch Equations |
| IR | Infrared |
| DFG | Difference-Frequency Generation |
| THz | Terahertz |
| SO | Surface Optical |
| SH | Second-harmonic |
| SHG | Second-harmonic generation |
| LL | Landau Level |
| AML | Active Mode Locking |
| SHB | Spatial Hole Burning |
| EM | Electromagnetic |

TABLE OF CONTENTS

Page

LIST OF FIGURES

FIGURE Page

# 1. INTRODUCTION

During the past few years, we have studied the optical properties of two types of two-dimensional (2D) semiconductor structures. One of them is based on semiconductor heterostructures, where semiconductors with different band gaps are grown layer by layer, so quantum wells (QWs) are formed. And the other is the natural 2D material, graphene. Here we give a brief introduction about them.

## 1.1 Semiconductor Quantum Wells

In a QW structure, the motion of electrons in the conduction band (or holes in the valence band) is confined by the potential well in the growth direction, so the energy is quantized. On the other hand, the electrons can move freely in the transverse directions. So, energy subbands are formed. See Fig. 1.1 for an illustration. The

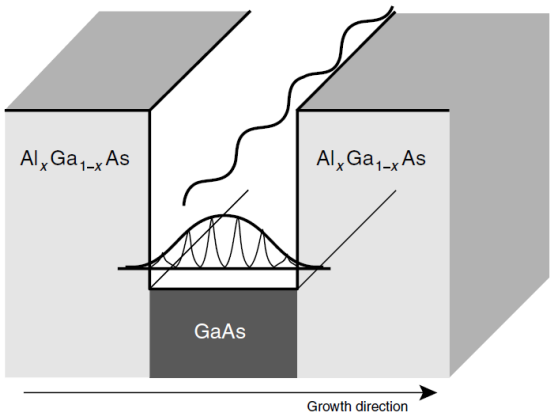


Figure 1.1: A potential well is resulted when a GaAs layer is grown between two $Al_xGa_{1-x}As$ barrier layers, which have larger band gap. [2]

energies of electrons in the conduction band can be expressed as

$$E_{n\vec{k}} = E_{n0} + \frac{\hbar^2 k^2}{2m^*}, \tag{1.1}$$

where $n$ is the index of energy level due to quantization in the growth direction, $\vec{k}$ is the in-plane wave vector, and $m^*$ is the effective mass. The expression for energies of holes in the valence band is similar. For semiconductors with direct band-gap, optical transitions can be either interband or intersubband, where electronic transitions are between the valence band and conduction band in the former case, while they are between the subbands of conduction band (or valence band), in the latter case. Both types of optical transitions are schematically shown in Fig. 1.2. These are the basics

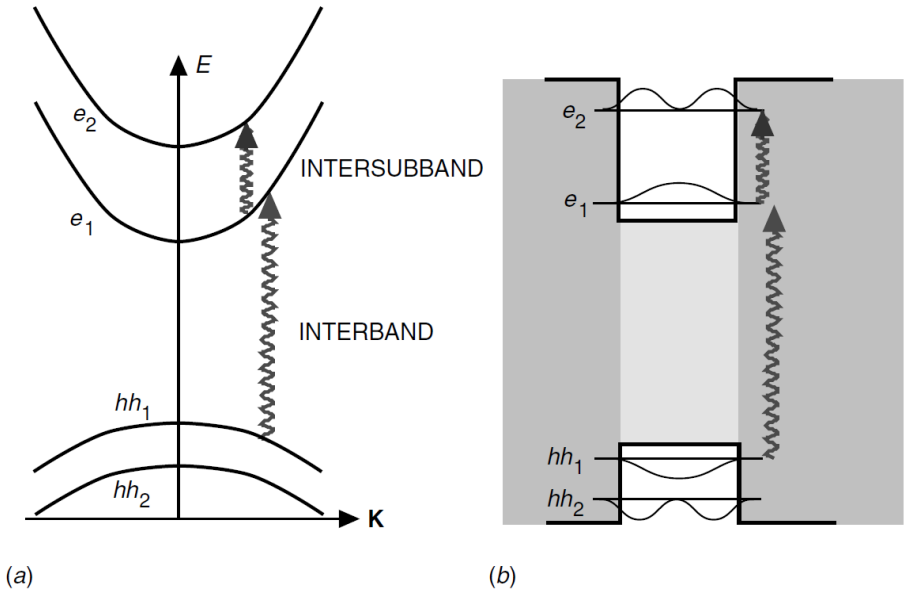


Figure 1.2: Optical transitions in direct band-gap semiconductors. The transitions are vertical in **K** space, since the momentum of a photon is small compared to the typical momentum of electrons, $\hbar k$. The transitions are represented (a) in reciprocal space and (b) in real space. [2]

of our work on optical properties of QW structures. More details can be found in the excellent review paper [1], and the textbook [2].

In a QW structure with high density of carriers, the electrons interact with each other due to the Coulomb potential, and this can lead to collective phenomenons. For example, superfluorescence (SF) from electron-hole plasma or magneto-plasma in QW structures has been observed by Dr. Kono's group in Rice university. As a collaboration, we have conducted numerical simulation to explain the observations. These will be presented in section 2.

While SF is due to optical recombination between electrons and holes, namely, interband transitions are involved, the interaction between electrons in the subbands of conduction band can also leads to collective excitations. We study the effect of Coulomb interaction on the second-order nonlinear optical processes, and it is presented in section 3.

Inter-subband lasing was proposed theoretically by Kazarinov and Suris [3], in which pumping by resonant tunneling is utilized. And it was first demonstrated by Faist *et al.* [4], which is called quantum cascade laser (QCL). The active region of QCL consists many ($\sim$50) periods of QWs. In each period, the electrons can be injected to the upper laser states, and go to the lower laser states by emitting photons, then they are scattered into a mini-band, and injected into the upper laser states of the next period. The concept of a typical QCL is shown in Fig. 1.3. For lasers, ultrashort pulses are usually generated by mode locking [6]. For passive mode locking, it is usually achieved by a saturable absorber. However, passive mode locking has not been achieved in QCLs, since a proper mechanism for introducing saturable absorber has not been found yet. For active mode locking, it is argued that only QCLs with long gain recovery time can be used [7]. Here we think this condition is not necessary for a two-section QCL, and we developed a model to show that active

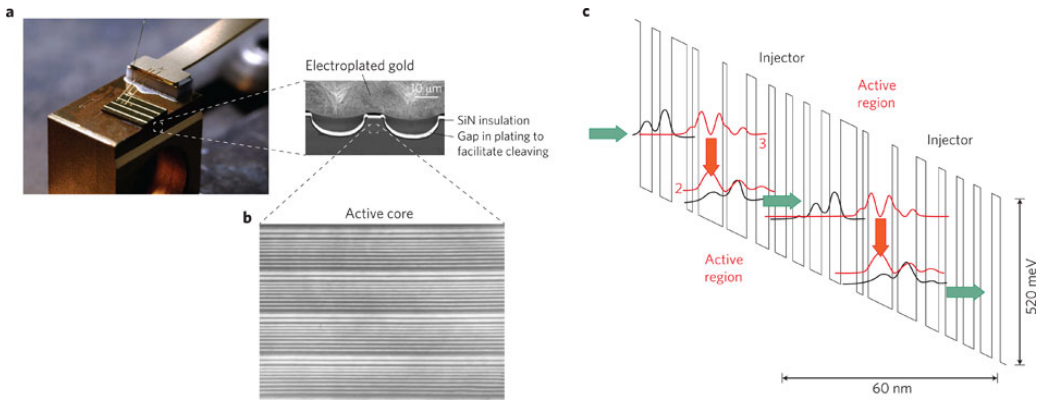


Figure 1.3: Concept of a typical QCL. (a), Photograph of a laser bar with four QCLs (left) and scanning electron microscopy image of the front facet of a QCL (right). (b), High-resolution transmission electron microscopy image of a QCL, showing four periods of active regions and injectors. (c), Simplified scheme of the conduction band structure for a basic QCL, where the laser transition is between sub-bands 3 and 2. [5]

mode locking can be achieved in normal mid-IR QCLs with short gain recovery time ($\sim 1\,\mathrm{ps}$) can be achieved, and the performance is even more robust. These will be presented in section 4.

## 1.2 Graphene

Graphene is a two dimensional allotrope of carbon atoms arranged in a honeycomb lattice due to their $sp^2$ hybridization [8], see Fig. 1.4 for details. The distance between neighboring carbon atoms is $a = 0.142\,\mathrm{nm}$. The honeycomb lattice contains two sublattices, marked A and B in Fig. 1.4. Both A and B sublattices are triangular Bravais lattices, and the honeycomb lattice can be viewed as a triangular Bravais lattice with a two-atom basis (A and B).

Using the tight-binding method, the electronic band of graphene can be calculated, which is shown in Fig. 1.5. We can see that the conduction and valence bands touch at the Dirac points $\mathbf{K}$ (or $\mathbf{K}'$). Near the Dirac point $\mathbf{K}$, we can write $\mathbf{k} = \mathbf{K}$

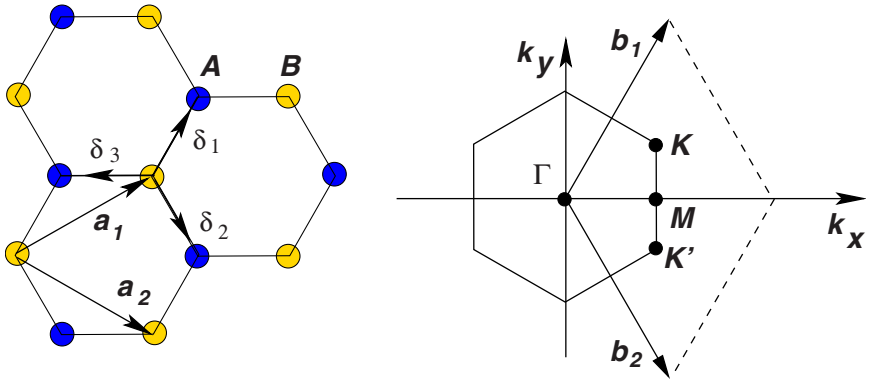


Figure 1.4: Left: Lattice of graphene, which contains two triangular Bravais lattices, A and B. $a_1$ and $a_2$ are the lattice unit vectors, and $\delta_i$ (i=1,2,3) are the nearest-neighbor vectors. Right: The first Brillouin zone, $b_1$ and $b_2$ are the reciprocal lattices, $K$ and $K'$ are the Dirac Points. [8]

+ $\mathbf{q}$, then the energy dispersion has the form

$$E_{\pm}(\mathbf{q}) \approx \pm\hbar v_F|\mathbf{q}| + O[(q/K)^2], \tag{1.2}$$

where + and - are for conduction and valence band respectively, and $v_F \approx 10^8 cm/s$ is the Fermi velocity. The Fermi level of intrinsic graphene is located at the energy of Dirac points, and it can be controlled by doping or applying a transverse electric field. When the next-nearest-neighbor hopping is neglected, the Hamiltonian can be written to the leading order of $q$ as,

$$H = v_F\vec{\sigma}\cdot\hat{\vec{p}} = v_F\begin{pmatrix} 0 & \hat{p}_x - i\hat{p}_y \\ \hat{p}_x + i\hat{p}_y & 0 \end{pmatrix}, \tag{1.3}$$

where the two by two matrix is a span of the two sublattices, and $\hat{p}$ is the momentum operator relative to $\mathbf{K}$ or $\mathbf{K}'$. The eigenenergies are $E_{\pm}(\mathbf{q}) = \pm\hbar v_F|\mathbf{q}|$, and

eigenstates are

$$\psi_s(\vec{q},\vec{r}) = \frac{1}{\sqrt{2L}} \exp(i\vec{q}\cdot\vec{r}) \begin{pmatrix} s \\ e^{i\theta(\vec{q})} \end{pmatrix}, \tag{1.4}$$

where $s = 1$ for conduction band, $s = -1$ for valence band, and $\theta(\vec{q})$ is the angle between the wave vector $\vec{q}$ and the x axis. Resonant optical transitions can occur

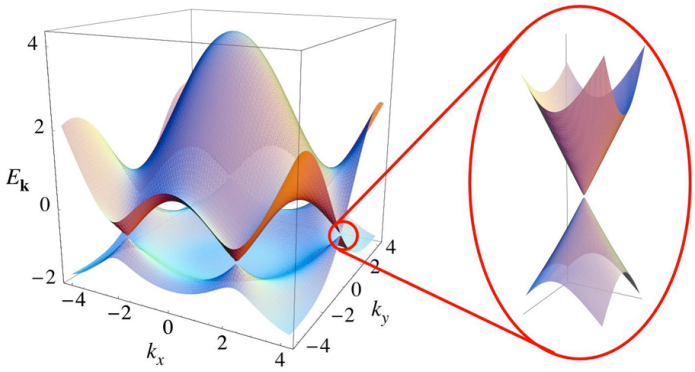


Figure 1.5: Electronic dispersion of graphene, with zoom in of the energy bands close to one of the Dirac points. It is shown the energy dispersion near the Dirac points is linear. [8]

between the conduction and valence bands of graphene.

When graphene is under a vertical magnetic field, its energy is quantized into Landau levels (LLs). For conventional semiconductors with parabolic dispersion, the energy separations between neighboring LLs are equal. However, the energy separations between neighboring LLs in graphene are unequal. Also, the optical selection-rules for graphene are different from conventional semiconductor materials. These properties give us the possibility to effectively control the populations in the LLs by optical field. We propose a scheme which can lead to Terahertz (THz) lasing

between graphene LLs. It is presented in section 5.

The nonlinear optical properties of graphene are also interesting. Second-harmonic generation (SHG) in graphene has been studied experimentally by Dr. Heinz's group in Columbia University (not published yet). The observation shows a relation between the polarizations of fundamental and second-harmonic (SH) lights. As a collaboration, we conducted theoretical calculation to explain the observation. We also have new predictions beyond the observed data. These are presented in section 6.

# 2. SUPERFLUORESCENCE FROM ELECTRON-HOLE PLASMA IN QUANTUM WELL STRUCTURES *

## 2.1 Introduction

Superradiance is a cooperative decay of excited dipoles, which was predicted by Dicke in 1954 [9]. For $N$ excited dipoles confined in a small volume, if the distance between dipoles is much smaller than the wavelength of light, then the dipoles can interact with the light coherently. This will lead the dipoles to emit light with intensity proportional to $N^2$, instead of being proportional to $N$ in the conventional exponential decay. See Fig. 2.1 for a schematic description. Superradiance was first observed in optically pumped HF gas in 1973 [10]. However, superradiance in solids has not been observed before our work in collaboration with Dr. Kono's group, where superfluorescence (delayed superradiance) is observed in electron-hole magneto-plasma [11]. The condition to have superradiance is that the cooperative frequency $\omega_c$ must exceed the dephasing rate of the optical polarization [12, 13],

$$\omega_c = \sqrt{\frac{8\pi^2 d^2 n \Gamma c}{\hbar \tilde{n}^2 \lambda L_{QW}}} \geq \frac{2}{T_2} \ , \tag{2.1}$$

where $d$ is the dipole moment, $n$ is the 2D electron-hole density, $\Gamma$ is the overlap factor of the radiation field with the quantum well structure, $\lambda$ is the wavelength, $c$ is the speed of light, $L_{QW}$ is the width of the quantum wells, and $T_2$ is the dephasing

*Part of the result reported in this section is reprinted with permission from "Giant superfluorescent bursts from a semiconductor magneto-plasma" by G. Timothy Noe II, Ji-Hee Kim, Jinho Lee, Yongrui Wang, Aleksander K. W ojcik, Stephen A. McGill, David H. Reitze, Alexey A. Belyanin and Junichiro Kono, 2012, Nature Physics **8**, 219-224, Copyright [2012] by Nature Publishing Group; and "Fermi-edge superfluorescence from a quantum-degenerate electron-hole gas" by Ji-Hee Kim, G. Timothy Noe II, Stephen A. McGill, Yongrui Wang, Aleksander K. W ojcik, Alexey A. Belyanin and Junichiro Kono, 2013, Scientific Reports **3**, 3283, Copyright [2013] by Nature Publishing Group.

time. In solids, dephasing time is generally quite small due to the various scattering processes. However, semiconductor quantum wells under magnetic field can have increased $d$, $n$ and $T_2$, making the condition be satisfied. This is because the energy of electrons is quantized in the growth direction, and the energy of the in-plane motion is also quantized to Landau levels due to the magnetic field. And we can see that both $d$ and $n$ increase with the magnetic field $B$. Furthermore, the scattering channel is suppressed, so $T_2$ also increases with $B$. This should be the main reason why superradiance is observed from the magneto-plasma in quantum wells. We will describe the experimental observation, and gives our theoretical explanations.

## 2.2 Experimental Observations

Before describing the experimental observations, we will give some basics related to this work. For electrons and holes in a QW structure under a transverse magnetic field, the energy is fully quantized. The energy of a Landau level is given by $E_n = (n + 1/2)\hbar\omega_c$, with $\omega_c = eB/m^*c$, where $m^*$ is the effective mass of the electrons or holes. Optical recombinations can only occur for electrons and holes with the same subband level, and the same Landau level index. In our study, both electrons and holes are in their lowest subbands, so we will only require them to have the same Landau level index for recombination to happen.

### *2.2.1 Experimental Observation of Superfluorescence from a Semiconductor Magneto-plasma*

The sample used in this study was a stack of fifteen undoped quantum wells consisting of 8 nm $In_{0.2}Ga_{0.8}As$ wells and 15 nm GaAs barriers. The confinement of the well resulted in quantized energy subbands for electrons in the conduction band and holes in the valence band. The strain present in this sample resulted in a large splitting of the heavy-hole ($H_1$) and light-hole ($L_1$) states (Fig. 2.2a), with only the

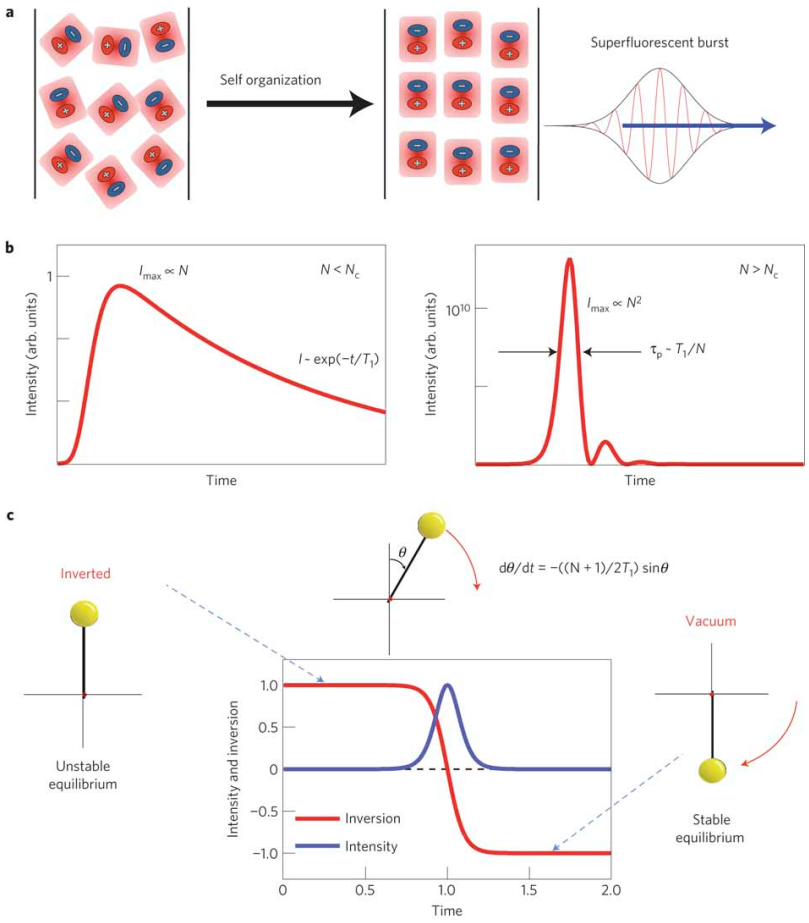


Figure 2.1: Superfluorescence from a collection of dipoles (atoms, molecules, ions or excitons). (a), Self-organization of dipoles and the resulting superfluorescent pulse. (b), Characteristics of light emission dynamics after pulse excitation for weak (left) and strong (right) excitation. When the number of dipoles, $N$, is smaller than a critical value ($N_c$), the peak intensity is proportional to $N$ and the intensity decays exponentially with a lifetime $T_1$. Under high excitation such that $N > N_c$, a delayed superfluorescent pulse appears with intensity proportional to $N^2$ and pulse width $\sim T_1/N$. (c), Population inversion and emitted light intensity (normalized to the peak intensity) versus time (normalized to the pulse delay) for a superfluorescent system, together with Bloch vector dynamics analogous to the dynamics of an over-damped pendulum going from an unstable equilibrium position ($\theta = 0°$) to the stable ground state ($\theta = 180°$) by releasing all its energy as a burst of superfluorescence.

heavy-hole states being relevant to the present study. On optical excitation using a Ti:sapphire laser with photon energy centered at 1.55 eV, carriers are excited above the bandgap of the GaAs barriers. Both the electrons and holes then experience many scattering events before relaxing into the quantum well to form two-dimensional magneto-excitons. We employ the high-field Landau level notation, (NM), to specify each magneto-exciton state, where N (M) is the electron (hole) Landau level index. The three lowest-energy, dipole-allowed transitions that we primarily study in this work are the (NM) = (00), (11) and (22) transitions, which correspond to the 1s, 2s and 3s transitions using the low-field excitonic notation [14].

Pump-probe measurements were made in a transmission geometry in the Faraday configuration (Fig. 2.2b), where the pump and probe beams were parallel to the magnetic field and incident normal to the quantum wells. The differential transmission, $\Delta T/T$, when tuned to a particular transition, is proportional to the population inversion for that transition, which is equal to the difference between the number of occupied and unoccupied exciton states. Figure 2.2c,d demonstrates that at the lowest temperature, 5 K, there is a sudden decrease in population inversion when the magnetic field, B, is higher than 10 T. At lower B, the population dynamics of the (11) transition exhibits a typical long exponential decay, as seen in Fig. 2.2c. With increasing B, the exponential decay transforms into a sudden decrease that becomes faster and occurs at a shorter time delay, $\sim$80 ps, for the (11) transition at 17.5 T. The (22) transition under the same conditions shows similar results, except that the sudden decrease in population occurs at an even shorter delay time, 60 ps, for the highest B, as shown in Fig. 2.2d. Finally, Fig. 2.2e shows that decreasing the temperature, T, and increasing B have a similar effect, that is, the change in population becomes more sudden and occurs at a shorter time delay when T changes from 150 K to 5 K.

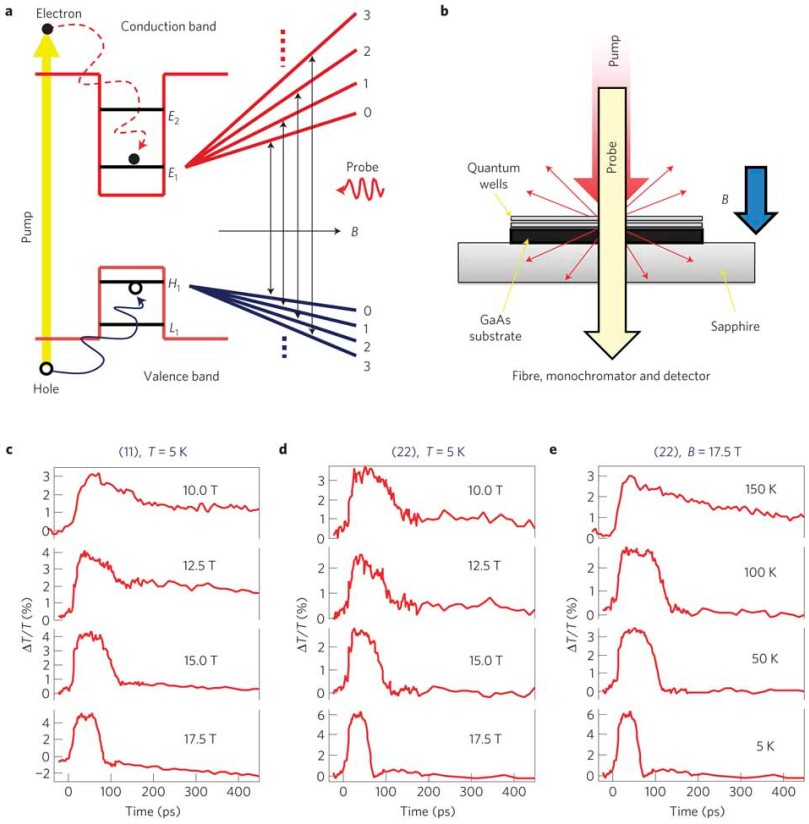


Figure 2.2: Observation of a sudden population drop through ultrafast pump-probe spectroscopy. (a), Sample studied and schematic diagram of energy levels in the system. (b), Experimental configuration of pump-probe measurements. (c), Pump-probe data for the (11) level at different magnetic fields at 5 K. (d), Pump-probe data for the (22) level at different magnetic fields at 5 K. (e), Pump-probe data for the (22) level at 17.5 T at different temperatures.

Spectrally and temporally resolved photoluminescence, collected in the geometry depicted in Fig. 2.3a, revealed superfluorescent pulses under various B, T and pump conditions, as shown in Fig. 2.3b−g. Figure 2.3b shows time-resolved photoluminescence data at 17.5 T and 5 K, spectrally selected for the (00) transition, taken with pump pulse energies, 0.25 nJ and 10 $\mu$J, to be compared with Fig. 2.1b. For weak excitation (0.25 nJ), the photoluminescence, measured from the centre fibre, shows an initial slow increase due to exciton formation, followed by interband relaxation with an exponential decay time of hundreds of picoseconds. The photoluminescence measured from the edge fibre provided a similar decay, but the signal was ∼40 times lower, indicating that the emission under weak excitation is typical spontaneous emission radiated in all directions with equal probability. In contrast, for strong excitation (10 $\mu$J), we observe a giant, delayed pulse of radiation from the edge fiber. The photoluminescence measured in the centre fibre showed no pulse of radiation and the peak intensity was ∼100 times lower. Quantitatively, Fig. 2.3b shows that an increase in pump pulse energy by roughly four orders of magnitude results in a peak emission intensity that is roughly six orders of magnitude larger. This is in agreement with the expected N3/2-dependence for superfluorescence in extended samples14, where N is the number of excited dipoles (electron-hole pairs in the present case). These results indicate that with increasing magnetic field strength, increasing pump pulse energy and decreasing temperature, the regime of light emission undergoes a transition from ordinary spontaneous emission to superfluorescence dominating the in-plane emission at high pump-pulse energy. Figure 3c overlays pump-probe and time-resolved photoluminescence data taken under the same conditions for the (22) transition, where we see that the appearance of the giant emission pulse coincides in time with the abrupt population drop from its maximum value to zero. This is in stark contrast with the dynamics of ordinary single-pass amplifiers,

where a pulse of the amplified spontaneous emission would consume at most half of the population.

Figure 2.3d shows a photoluminescence intensity map as a function of delay time and photon energy at 17.5 T, 5 K and 5 $\mu$J. Pulses of superfluorescence coming from the (00), (11) and (22) transitions are clearly resolved, both in time and energy. For each transition, a large pulse of radiation appears after some delay time. The highest-energy transition, (22), emits a pulse first, and each lower-energy transition emits a pulse directly after the transition just above it. Figure 2.3e shows the effects of lowering B to 15 T: (1) the separation between Landau levels decreases (compare the left-hand panels of Fig. 2.3d,e), (2) the emission of superfluorescence occurs at later delay times for a given transition (compare the right-hand panels of Fig. 2.3d,e), and (3) the superfluorescent pulse intensity decreases (compare Fig. 2.3d,e). With decreasing pump pulse energy, we see the emission decrease dramatically (compare Fig. 2.3d,f). With increasing T, the emission from all transitions weakens significantly and moves to later delay times (Fig. 2.3g); the emission energies decrease with increasing T owing to bandgap shrinkage.

The sudden drop of population inversion, together with the burst of a pulse, indicate that superfluorescence is achieved in the electron-hole magneto-plasma.

### *2.2.2 Time-resolved Measurement of Superfluorescence from a Quantum-degenerate Electron-hole Gas*

Furthermore, time-resolved photoluminescence of the electron-hole plasma or magneto-plasma is measured.

Figure 2.4a shows the experimental geometry used in this work. Photoluminescence (PL) travels in all directions, but some of the emission travels in the plane of the quantum wells, which is reflected by the micro-prism towards our collection op-

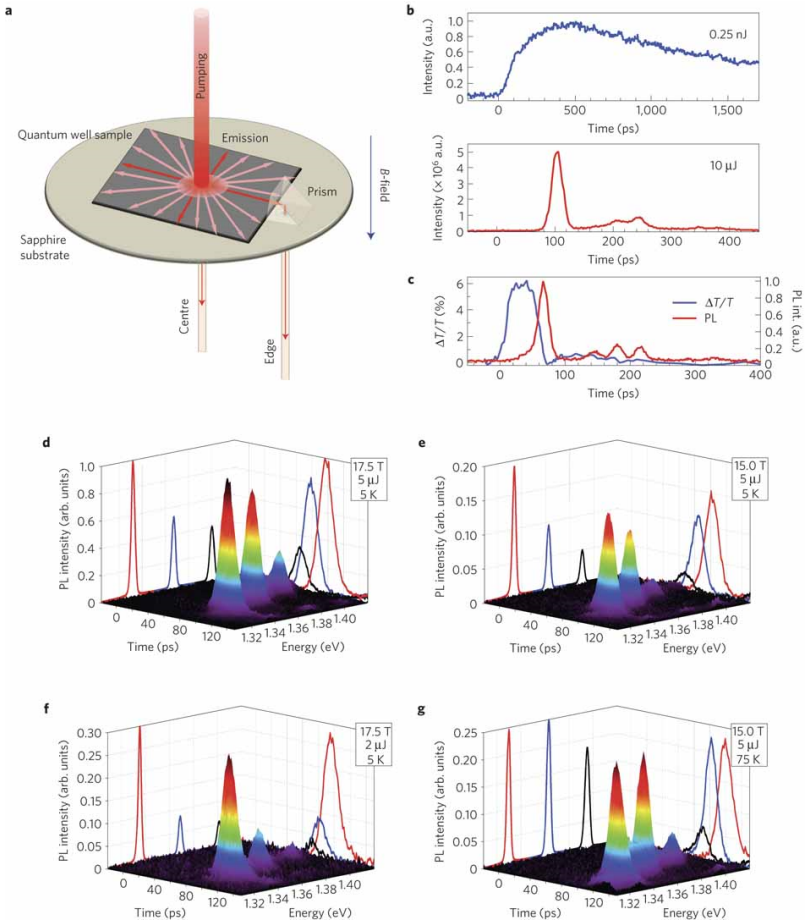


Figure 2.3: Observation of delayed bursts of radiation through time-resolved photoluminescence spectroscopy. (a), Set-up. (b), Time-resolved emission for weak (top) and strong (bottom) excitation for the (00) transition at 17.5 T and 5 K. This should be compared with Fig. 2.1b. (c), Comparison between pump-probe data and time-resolved photoluminescence (PL) for the (22) level at 17.5 T and 5 K, demonstrating the temporal coincidence between the population drop in pump-probe differential transmission and emission of the giant pulse of radiation. This should be compared with Fig. 2.1c. (d)−(g), Streak camera images of emission intensity as a function of photon energy and delay time at 17.5 T, 5 $\mu$J pump pulse energy and 5 K (d), 15.0 T, 5 $\mu$J pump pulse energy and 5 K (e), 17.5 T, 2 $\mu$J pump pulse energy and 5 K (f) and 17.5 T, 5 $\mu$J pump pulse energy and 75 K (g). In d−g, the left hand panels show the time-integrated emission spectra, with the (00) peak in red, (11) in blue and (22) in black, while the right hand panels show time-resolved slices at the peak positions of the (00), (11) and (22) transitions.

tics. Figure 2.4b shows the result of time-resolved measurements of in-plane-emitted PL taken at 15 K at zero magnetic field with a pump pulse energy of 5 $\mu$J. The dominant feature is a line of emission starting from $\sim$1.45 eV and ending at $\sim$1.325 eV, i.e., the emitted photon energy changes continuously with time. There is a kink in the line at $\sim$1.42 eV, which corresponds to the $E_1L_1$ transition; the curvature of the line also changes slightly at that kink. Figure 2.4c shows some vertical slices of the data in Fig. 2.4b at various time delays. We see that for a given time delay there is an emission peak with a spectral width of 5$-$10 meV, which dynamically shifts to lower energy as time passes. Figure 2.4d shows some horizontal slices of the data in Fig. 2.4b at various photon energies, demonstrating an ultrashort pulse of light emitted at a given photon energy at a certain time delay after excitation.

We found that the spectral and temporal behavior of the emission line sensitively depends on the excitation pulse energy and temperature. Figures 2.5a$-$c show time-resolved PL maps taken with different excitation pulse energies at zero magnetic field. The map constructed with 2.1 $\mu$J pulse energy looks very similar to the map constructed with 5 $\mu$J (Fig. 1b). When the power is further decreased, there is a non-monotonic temporal shift in the line of emission. For a given photon energy close to the middle of the line, say 1.37 eV, we see that the line moves to earlier time from 2.1 to 1 $\mu$J and then back to a later time at 0.5 $\mu$J excitation pulse energy with a change in curvature. At the highest photon energy for strong emission in the line, at $\sim$1.45 eV, the emission moves to earlier time delays with decreasing power and then stays there for the lowest power. For all excitation powers, the emission line ends at 1.325 eV, which corresponds to the $E_1H_1$ band-edge. We also varied the temperature while fixing the excitation pulse energy at 5 $\mu$J, as shown in Figs. 2.5d$-$f. With increasing temperature, there is a smearing of the emission line at the lowest photon energies of the line, until all of the emission from the $E_1H_1$ contribution of the line

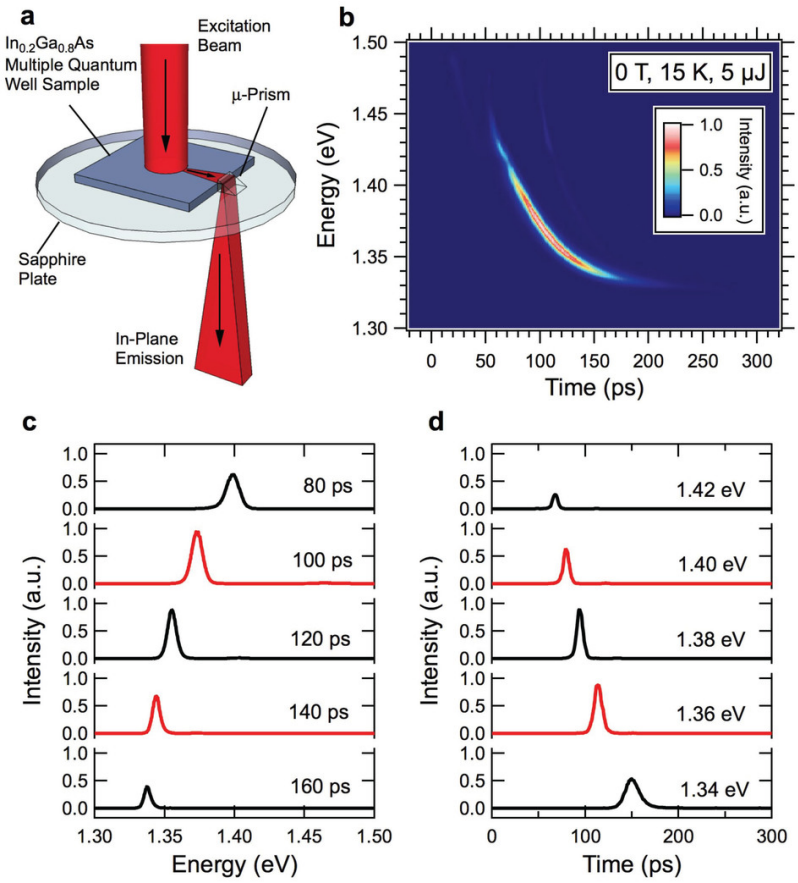


Figure 2.4: Observation of intense ultrashort pulses of radiation from a photo-excited InGaAs quantum well sample with photon energy and time delay continuously changing with time. (a), The experimental geometry. The in-plane emission is redirected with a micro-prism towards the collection optics. The sample was kept at 15 K and 0 T. The excitation photon energy, pulse width, and pulse energy were ∼1.6 eV, ∼150 fs, and 5 $\mu$J, respectively. (b), Photoluminescence intensity as a simultaneous function of time delay and photon energy. The peak emission red-shifts as a function of time. (c), Spectral slices of the map in (b) for various time delays. (d), Temporal slices of the map in (b) for various photon energies, showing pulses of radiation whose delay time with respect to the pump pulse becomes longer with decreasing photon energy.

is 'washed out', and only the slightest signal at the $E_1L_1$ portion remains at 100 K. It is clear that the emission burst moves to later times as it is 'washed out' at high temperatures.

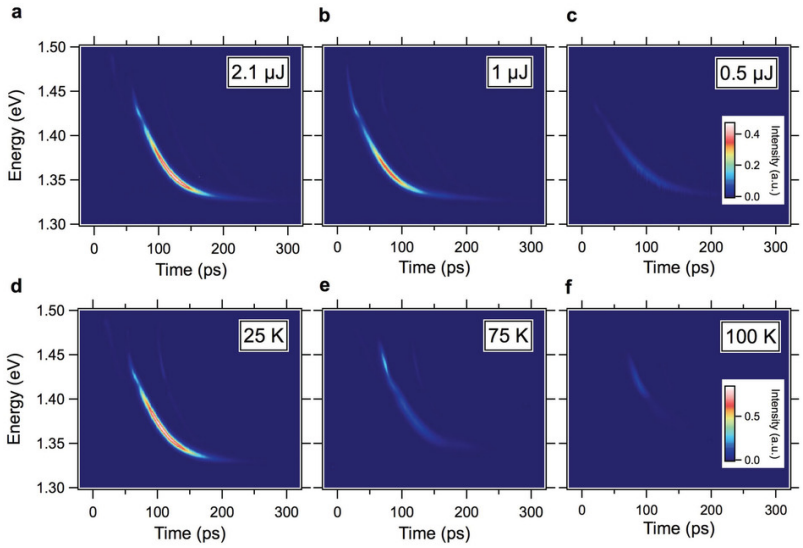


Figure 2.5: Excitation pulse energy and temperature dependence of the observed pulsed radiation at zero magnetic field. Photoluminescence intensity versus time delay and photon energy for excitation pulse energies of (a) 2.1 $\mu$J, (b) 1 $\mu$J, and (c) 0.5 $\mu$J at 15 K and 0 T. Photoluminescence intensity versus time delay and photon energy at (d) 25 K, (c) 75 K, and (e) 100 K, with 5 $\mu$J excitation pulse energy at 0 T. The intense pulsed emission of radiation becomes weaker with decreasing (increasing) excitation power (temperature) and eventually disappears when the excitation power (temperature) becomes too low (high).

The emission spectrum and dynamics drastically change when a magnetic field perpendicular to the quantum well plane is applied. Figures 2.6a−e show streak camera images of emission as a function of photon energy and time delay at different magnetic fields. With increasing magnetic field, the number of peaks decreases, and the energy separation between adjacent peaks increases due to increasing Landau quantization energy (i.e., the cyclotron energy). Previously we demonstrated the

superradiant nature of the individual emission peaks by streak-camera and pump-probe measurements [11]. Here we observe that at a given magnetic field the delay is longer for emission from lower Landau levels, and the (NN) = (00) SF emission occurs only after the higher-energy SF emissions occur. This means that the relative timing of the bursts coming from different Landau levels is not random. Rather, these data clearly indicate that e-h pairs in the highest occupied energy states near the quasi-Fermi edge at a given time always recombine first; e-h pairs in lower and lower energy states then emit bursts sequentially. Figure 2.6f summarizes the peak positions of the SF bursts as a function of photon energy and time.

## 2.3 Theoretical Explanation

At the linear stage of SF, when the fields grow exponentially, the field experiencing the maximum gain will dominate over fields with other frequencies. So, we may explain the red-shifting observed by calculating the dependence of gain spectrum on the carrier density. Here we use the semiconductor Bloch equations (SBEs) to study SF from a high-density electronhole (e-h) plasma. In this method the many-body Coulomb interaction is included. The usual form of the SBEs [15] is for bulk semiconductors or 2D electron gas, where the states can be labeled by 3D or 2D wave vectors $\vec{k}$. For QWs under transverse magnetic field, the eigen-states are not plane waves. So, we rederive SBEs following the same basic approximations but in a more general form, which accommodates the effects of a finite well width and the quantization of motion in a strong magnetic field. We begin with a general

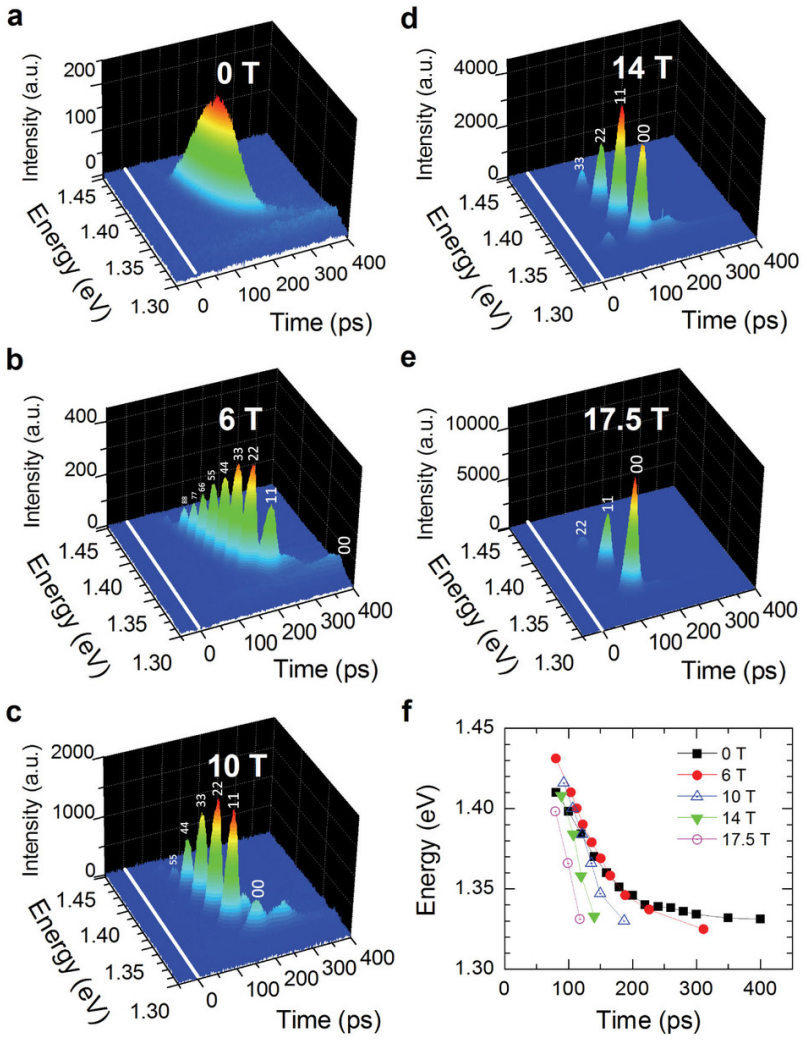


Figure 2.6: Magnetic-field evolution of the observed pulsed coherent emission as a function of photon energy and time delay. Time-resolved emission spectra at (a), 0 T, (b), 6 T, (c), 10 T, (d), 14 T, and (e), 17.5 T with 2 $\mu$J of excitation pulse energy at 5 K. Each (N, N) recombination is observed as a delayed burst of superfluorescence (N: Landau level index). With increasing magnetic field, the number of peaks decreases, and the energy separation between adjacent peaks increases due to increasing Landau quantization energy. At a fixed magnetic field, the delay is longer for smaller N. Note that the N = 0 state is the last to burst. (f), Peak shift of emission as a function of time at different magnetic fields.

Hamiltonian in the two-band approximation and e-h representation,

$$\begin{aligned}\mathcal{H} &= \sum_{\alpha}\left[\left(E_g^0+E_\alpha^e\right)a_\alpha^\dagger a_\alpha + E_\alpha^h b_{\bar{\alpha}}^\dagger b_{\bar{\alpha}}\right] \\ &+ \frac{1}{2}\sum_{\alpha\beta\gamma\delta}\left(V_{\alpha\beta\gamma\delta}^{ee}a_\alpha^\dagger a_\beta^\dagger a_\delta a_\gamma + V_{\bar{\alpha}\bar{\beta}\bar{\gamma}\bar{\delta}}^{hh}b_{\bar{\alpha}}^\dagger b_{\bar{\beta}}^\dagger b_{\bar{\delta}} b_{\bar{\gamma}} + 2V_{\alpha\bar{\beta}\gamma\bar{\delta}}^{eh}a_\alpha^\dagger b_{\bar{\beta}}^\dagger b_{\bar{\delta}} a_\gamma\right) \\ &- \mathcal{E}(t)\sum_{\alpha}\left(\mu_\alpha a_\alpha^\dagger b_{\bar{\alpha}}^\dagger + \mu_\alpha^* b_{\bar{\alpha}} a_\alpha\right)\ , \end{aligned} \tag{2.2}$$

where $E_g^0$ is the unperturbed bandgap, $a_\alpha^\dagger$ and $b_{\bar{\alpha}}^\dagger$ are the creation operators for the electron state $\alpha$ and hole state $\bar{\alpha}$, respectively, $\mathcal{E}(t)$ is the optical field, $\mu_\alpha$ is the dipole matrix element, and $V_{\alpha\beta\gamma\delta}$ are Coulomb matrix elements, for example, $V_{\alpha\beta\gamma\delta}^{ee} = \int d\vec{r}_1 \int d\vec{r}_2 \Psi_\alpha^{e*}(\vec{r}_1)\Psi_\beta^{e*}(\vec{r}_2)\frac{e^2}{\epsilon|\vec{r}_1-\vec{r}_2|}\Psi_\gamma^e(\vec{r}_1)\Psi_\delta^e(\vec{r}_2)$. Here we denote the hole state which can be recombined with a given electron state $\alpha$ optically by $\bar{\alpha}$, and assume that there is a one-to-one correspondence between them. For the interband Coulomb interaction, $V_{\alpha\bar{\beta}\gamma\bar{\delta}}^{eh}a_\alpha^\dagger b_{\bar{\beta}}^\dagger b_{\bar{\delta}} a_\gamma$ is the only non-zero matrix element due to the orthogonality between the Bloch functions of the conduction and valence bands [16]. The electron and hole wave functions can be written as $\Psi_\alpha^e(\vec{r}) = \psi_\alpha^e(\vec{r})u_{c0}(\vec{r})$ and $\Psi_{\bar{\alpha}}^h(\vec{r}) = \psi_{\bar{\alpha}}^h(\vec{r})u_{v0}^*(\vec{r})$, respectively. In the problems we study, the conduction band and valence band states connected by an optical transition always have the same envelope wave function, so we take $\psi_{\bar{\alpha}}^h(\vec{r}) = \psi_\alpha^{e*}(\vec{r})$). Then the Coulomb matrix elements are related with each other through $V_{\bar{\alpha}\bar{\beta}\bar{\gamma}\bar{\delta}}^{hh} = V_{\gamma\delta\alpha\beta}^{ee}$ and $V_{\alpha\bar{\beta}\gamma\bar{\delta}}^{eh} = -V_{\alpha\delta\gamma\beta}^{ee}$, and we can drop the superscript by defining $V_{\alpha\beta\gamma\delta} \equiv V_{\alpha\beta\gamma\delta}^{ee}$.

Using the above Hamiltonian, we can obtain the equations of motion for the distribution functions $n_\alpha^e = \langle a_\alpha^\dagger a_\alpha\rangle$ and $n_\alpha^h = \langle b_{\bar{\alpha}}^\dagger b_{\bar{\alpha}}\rangle$, and the polarization $P_\alpha = \langle b_{\bar{\alpha}} a_\alpha\rangle$. Using the Hartree-Fock approximation (HFA) and the random phase approximation

(RPA), we arrive at the SBEs:

$$i\hbar\frac{d}{dt}P_\alpha = \left(E_g^0 + E_\alpha^{eR} + E_\alpha^{hR}\right)P_\alpha + \left(n_\alpha^e + n_\alpha^h - 1\right)\left[\mu_\alpha\mathcal{E}(t) + \sum_\beta V_{\alpha\beta\beta\alpha}P_\beta\right] + i\hbar\frac{d}{dt}P_\alpha\Big|_{scatt}, \tag{2.3}$$

$$\hbar\frac{d}{dt}n_\alpha^e = -2\ \mathrm{Im}\left[\left(\mu_\alpha\mathcal{E}(t) + \sum_\beta V_{\alpha\beta\beta\alpha}P_\beta\right)P_\alpha^*\right] + \hbar\frac{d}{dt}n_\alpha^e\Big|_{scatt}, \tag{2.4}$$

$$\hbar\frac{d}{dt}n_\alpha^h = -2\ \mathrm{Im}\left[\left(\mu_\alpha\mathcal{E}(t) + \sum_\beta V_{\alpha\beta\beta\alpha}P_\beta\right)P_\alpha^*\right] + \hbar\frac{d}{dt}n_\alpha^h\Big|_{scatt}, \tag{2.5}$$

where $E_\alpha^{eR} = \left(E_\alpha^e - \sum_\beta V_{\alpha\beta\beta\alpha}n_\beta^e\right)$ and $E_\alpha^{hR} = \left(E_\alpha^h - \sum_\beta V_{\alpha\beta\beta\alpha}n_\beta^h\right)$ are the renormalized energies, and the scattering terms account for higher-order contributions beyond the HFA and other scattering processes such as scattering with LO-phonons.

These equations, together with Maxwells equations for the electromagnetic field, can be applied to study the full nonlinear dynamics of interaction between the e-h plasma and radiation. Here we derive the gain for given carrier distributions $n_\alpha^e$ and $n_\alpha^h$. Assuming a monochromatic and sinusoidal time dependence for the field $\mathcal{E}(t) = \mathcal{E}_0 e^{-i\omega t}$ and the polarization $P_\alpha = P_{0\alpha}e^{-i\omega t}$, we can find $P_\alpha$ from Eq. 2.3 and define the quantity $\chi_\alpha(\omega) = P_{0\alpha}/\mathcal{E}_0$, which satisfies the equation below:

$$\chi_\alpha(\omega) = \chi_\alpha^0(\omega)\left[1 + \frac{1}{\mu_\alpha}\sum_\beta V_{\alpha\beta\beta\alpha}\chi_\beta(\omega)\right], \tag{2.6}$$

where

$$\chi_\alpha^0(\omega) = \frac{\mu_\alpha\left(n_\alpha^e + n_\alpha^h - 1\right)}{\hbar\omega - \left(E_g^0 + E_\alpha^{eR} + E_\alpha^{hR}\right) + i\hbar\gamma_\alpha}, \tag{2.7}$$

where $V$ is the normalization volume. The gain spectrum is given by [15]

$$g(\omega) = \frac{4\pi\omega}{n_b c}\mathrm{Im}[\chi(\omega)], \tag{2.8}$$

where $n_b$ is the background refractive index, and $c$ is the speed of light. We use the above general results to analyze optical properties under different conditions.

In a quantum well of thickness $L_w$, the envelope functions for electrons and holes are $\psi^{e,h}_{n,\vec{k}}(\vec{r}) = \varphi_n(z)\exp\left(i\vec{k}\cdot\vec{\rho}\right)/\sqrt{A}$, where $\vec{\rho} = (x, y)$, $\varphi_n(z)$ is the envelope wave function in the growth direction for the n-th subband, and $A$ is the normalization area. To calculate the Coulomb matrix element $V_{\alpha\beta\beta\alpha}$, we define $\tilde{V}_{\alpha\beta} \equiv V_{\alpha\beta\beta\alpha}$, and put $\alpha = \left\{n, \vec{k}, s\right\}$, $\beta = \left\{n', \vec{k}', s'\right\}$, where $s$ denotes the spin quantum index. Then one gets

$$\tilde{V}_{n,\vec{k},s;n',\vec{k}',s'} = V^{2D}(q)F_{nn'n'n}(q)\delta_{ss'}, \tag{2.9}$$

where $q = |\vec{q}| = |\vec{k} - \vec{k}'|$, $V^{2D}(q) = 2\pi e^2/\epsilon_0 A q$, with $\epsilon_0$ the dielectric constant and $A$ the normalization area, and the form factor $F_{nn'n'n}(q)$ is defined as

$$F_{n1,n2,n3,n4}(q) = \int dz_1 \int dz_2 \varphi^*_{n1}(z_1)\varphi^*_{n2}(z_2)\exp\left(-q\left|z_1 - z_2\right|\right)\varphi_{n3}(z_1)\varphi_{n4}(z_2). \tag{2.10}$$

Throughout the paper, we will assume that only the lowest subband for electrons and holes is occupied. In this case, we can define $\tilde{V}(q) = V^{2D}(q)F_{1111}(q)$. The dielectric function $\epsilon(\vec{q}, \omega)$, which describes the screening of the Coulomb potential, is given by the Lindhard formula for a pure 2D case [15]; it can be generalized to the quasi-2D case as

$$\epsilon(\vec{q}, \omega) = 1 + \tilde{V}(q)\left(\Pi_e(\vec{q}, \omega) + \Pi_h(\vec{q}, \omega)\right), \tag{2.11}$$

where $\Pi_{e(h)}(\vec{q},\omega)$ is the polarization function of an electron or hole, which is given by

$$\Pi(\vec{q},\omega) = 2\sum_{\vec{k}} \frac{n_{\vec{k}+\vec{q}} - n_{\vec{k}}}{\omega + i0^+ - E_{\vec{k}+\vec{q}} + E_{\vec{k}}}. \tag{2.12}$$

Here, we dropped the subscripts $e$ or $h$, $n_{\vec{k}}$ is the distribution function, the factor of 2 accounts for the summation over spin, and the spin index is suppressed. For simplicity, we will choose the static limit, namely, $\omega = 0$.

Given the dielectric function $\epsilon(q;0)$, the screened Coulomb matrix element is $\tilde{V}_s(q) = \tilde{V}(q)/\epsilon(q,0)$. For simplicity, we will still write it as $V(q)$. Applying Eq. 2.6 to the case above, we get the equation for $\chi_{\vec{k}}(\omega)$:

$$\chi_{\vec{k}}(\omega) = \chi^0_{\vec{k}}(\omega)\left[1 + \frac{1}{\mu_{\vec{k}}}\sum_{\vec{k}'}\tilde{V}\left(\left|\vec{k}-\vec{k}'\right|\right)\chi_{\vec{k}'}(\omega)\right], \tag{2.13}$$

where $\chi^0_{\vec{k}}(\omega)$ becomes

$$\chi^0_{\vec{k}}(\omega) = \frac{\mu_{\vec{k}}\left(n^e_{\vec{k}} + n^h_{\vec{k}} - 1\right)}{\hbar\omega - \left(E^0_g + E^{eR}_{\vec{k}} + E^{hR}_{\vec{k}}\right) + i\hbar\gamma_{\vec{k}}}, \tag{2.14}$$

To solve Eq. 2.13, we notice that $\chi^0_{\vec{k}}(\omega)$ does not depend on the direction of $\vec{k}$, so $\chi_{\vec{k}}(\omega)$ will not depend on it, either. Then, after converting the summation in Eq. 2.13 into the integral, the integration over the azimuthal angle is acting on $\tilde{V}\left(\left|\vec{k}-\vec{k}'\right|\right)$ only. If we define

$$\tilde{V}_s(k,k') = \frac{1}{2\pi}\int_0^{2\pi} d\phi \tilde{V}_s\left(\sqrt{k^2 + k'^2 - 2kk'\cos\phi}\right), \tag{2.15}$$

then Eq. 2.13 can be written as

$$\chi_k(\omega) = \chi_k^0(\omega)\left[1 + \frac{A}{2\pi\mu_k}\int_0^\infty k'dk'\tilde{V}_s\left(k,k'\right)\chi_k'(\omega)\right]. \tag{2.16}$$

After discretizing the integral, we have a system of linear equations for $\chi_k(\omega)$, which can be solved by using LAPACK [17]. The band structure for our sample consisting of undoped 8-nm $In_{0.2}Ga_{0.8}As$ wells and 15-nm GaAs barriers on a GaAs substrate is calculated using the parameters given by Vurgaftman *et al.* [18]. The strain effect is included using the results of Sugawara *et al.* [19]. Examples of calculated gain spectra are shown in Figs. 2.7a,b.

For a quantum well structure in a strong perpendicular magnetic field, the electronic states are fully quantized. Considering only the lowest subband in the quantum well, the equation for the susceptibility is written as

$$\chi_{n,s} = \chi_{n,s}^0\left[1 + \frac{1}{\mu_{n,s}}\sum_{n'} V_{n,n'}\chi_{n',s}\right], \tag{2.17}$$

where $n$ is the Landau level index, $s$ is the spin index, and $V_{n,n'}$ is the Coulomb matrix element given by

$$V_{n,n'} = \frac{e^2}{2\pi\epsilon_0}\int_0^{2\pi} d\theta \int_0^\infty dq \left|\int dx e^{iqx\cos\theta}\phi_n(x)\phi_{n'}^*(x + qa_H^2\sin\theta)\right|^2, \tag{2.18}$$

where $\phi_n(x)$ is the x-dependent part of the wavefunction of the $n$-th Landau level and $a_H^2 = \hbar c/eB$. The renormalized electronic energies in the expression for $\chi_{n,s}^0$ are

$$E_{n,s}^{eR} = E_{n,s}^e - \sum_{n'} V_{n,n'}n_{n'}^e, \tag{2.19}$$

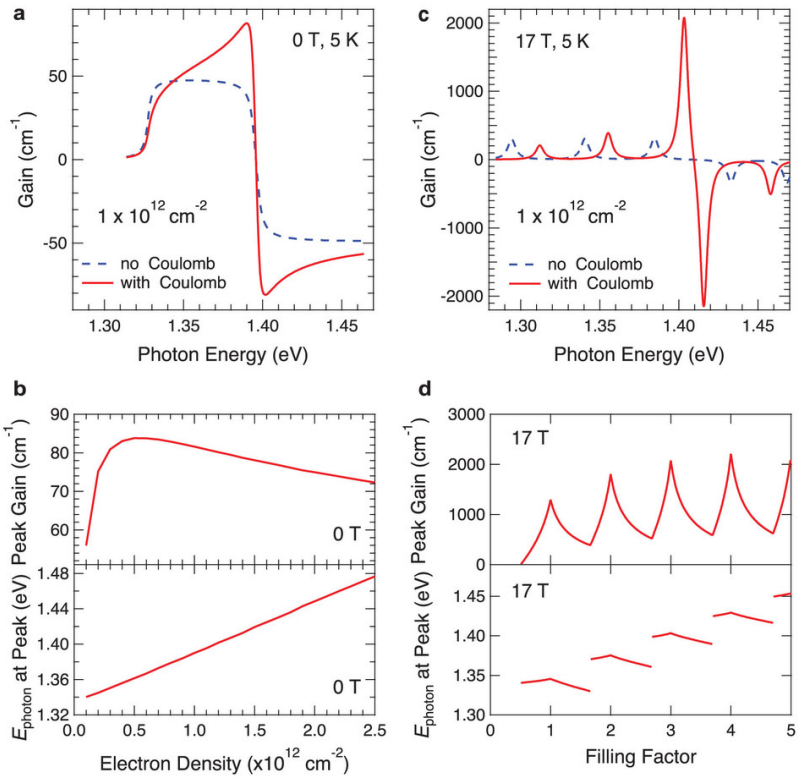


Figure 2.7: Theoretical calculations of Coulomb-induced many-body enhancement of gain at the Fermi energy at zero magnetic field and 17 T. (a), Gain spectrum for the InGaAs sample without a magnetic field, calculated using Eq.2.6 (solid line), in comparison with the spectrum obtained by replacing $\chi_\alpha(\omega) \rightarrow \chi^0_\alpha(\omega)$, i.e., neglecting all Coulomb effects except band-gap renormalization (dashed line). Separate Fermi distributions for electrons and holes of density $1 \times 10^{12}\, cm^2$ and temperature 5 K are assumed. A relaxation rate of 2 meV is assumed. (b), Peak gain (upper panel) and peak gain energy (lower panel) as a function of e-h density at zero magnetic field. Other parameters are the same as in (a). (c), Calculated gain spectrum in a magnetic field of 17 T (solid line), in comparison with the spectrum obtained by replacing $\chi_\alpha(\omega) \rightarrow \chi^0_\alpha(\omega)$, i.e., neglecting all Coulomb effects except band-gap renormalization (dashed line). A filling factor $\nu = 3$ and a temperature of 5 K are assumed. A relaxation rate of 3 meV is adopted. (d), Peak gain (upper panel) and peak gain energy (lower panel) at 17 T as a function of filling factor, defined as the number of filled Landau levels. Other parameters are the same as in (c).

and a similar equation holds for holes. The gain is calculated as

$$g(\omega) = \frac{4\pi\omega}{n_b c} \frac{1}{\pi a_H^2} \mathrm{Im} \left[ \sum_n \mu_{n,s}^* \chi_{n,s} \right]. \tag{2.20}$$

An example of the calculated gain for B = 17 T is shown in Figs. 2.7c,d.

It is seen that Coulomb interactions lead to an enhancement of gain just below the energy that corresponds to the difference between the quasi-Fermi levels of electrons and heavy holes. Previously, a related effect of "Fermi-edge singularity" has been observed in the spontaneous PL spectra of n-doped quantum wells in a steady state [20]. In the present case, the many-body gain enhancement is completely due to a nonequilibrium photo-excited e-h plasma. Stimulated emission occurs in the quantum well plane, and the light intensity grows exponentially, both in space and time. As a result, the rather broad many-body enhancement in the gain spectrum around Fermi energy translates into a sharp peak in the instantaneous intensity spectrum. The subsequent time evolution of the spectrum is dominated by an ultrafast collective recombination process: the peak continuously follows the red-shift of the quasi-Fermi level as the carriers at the Fermi edge are consumed by the SF. This behavior, observed in our samples according to Fig. 2.5, is in agreement with Fig. 2.7b, which shows the calculated evolution of the peak gain and peak gain energy as a function of e-h pair density. Furthermore, the highest gain, which leads to the fastest decay, is seen to be achieved at some intermediate density, which explains the observed non-monotonic temporal shift as a function of pump power (Figs. 2.5a-c).

In a strong magnetic field, the gain spectrum exhibits strong peaks when the Landau level filling factor is an integer, and for a given filling factor, the gain is largest for the highest filled Landau level (Figs. 2.7c,d). A snapshot of the gain for a fixed filling factor $\nu = 3$, corresponding to three filled Landau levels, is shown in

Fig. 2.7c for a magnetic field of 17 T. A relaxation time of 3 meV is adopted. It can be seen that the peak gain for e-h pairs at the N = 3 Landau level is much higher than that for completely filled, lower Landau levels. Note that the peak gain value is strongly enhanced compared to quantum wells without a magnetic field due to an increase in the transition matrix element and density of states. This provides a natural explanation for the trend observed in Fig. 2.6f, i.e., SF develops faster in a stronger magnetic field. Figure 2.7d shows the calculated peak gain and peak gain energy as a function of filling factor at a fixed magnetic field of 17 T. The peculiar many-body dynamics of the peak gain lead to isolated SF bursts that are fired consecutively from higher to lower Landau levels, as observed in Fig. 2.6.

## 2.4 Summary

In summary, the results of this study not only provide new insight into the nonequilibrium dynamics of Coulomb-correlated e-h pairs in semiconductors but also open up new possibilities of controlling, and enhancing, collective emission properties of many-body states. Specifically, we showed that superfluorescence, a well-known phenomenon in quantum optics of atoms based on photon exchange between inverted atomic dipoles, takes a new turn when it occurs in a condensed matter system, where Coulomb correlations (i.e., virtual-photon exchange) create enormous gain concentrated at the Fermi edge, which becomes better defined at lower temperatures (Figs. 2.5d−f). Thus, this work demonstrates a unique method of producing ultrashort pulses of radiation from a semiconductor, based on the existence of Fermi-degenerate, nonequilibrium electrons and holes.

# 3. ENHANCEMENT OF SECOND-ORDER NONLINEAR OPTICAL PROCESSES FOR INTERSUBBAND TRANSITIONS BY COULOMB EFFECT

## 3.1 Introduction

Intersuband optical transitions are usually described in a single-particle picture. However, the carriers inside a QW interact with each other due to the Coulomb potential from electrons, which can lead to collective excitations. For example, in a QW with high density of electrons, the response to the optical field is modified from the single-particle picture, because the electrons are affected by the induced field of the excited electrons, which is called the depolarization field [1, 16]. The collective mode is given the name of intersubband plasmon [21]. It was found that the absorption has a blue shift when the effect of intersubband plasmon is included [22]; see Figs. 3.1 and 3.2 for details. In the work by the same group, the intersubband plasmon effects are calculated in the picture of dipole-dipole interaction [23]. Here we use density matrix equations to calculate the Coulomb effect on intersubband optical transitions, and find that it can enhance the second-order nonlinear optical processes.

## 3.2 Hamiltonian

In second quantization, the Hamiltonian can be written as

$$H = H_0 + H_{ee} + H_{ei} + H_{ii}, \tag{3.1}$$

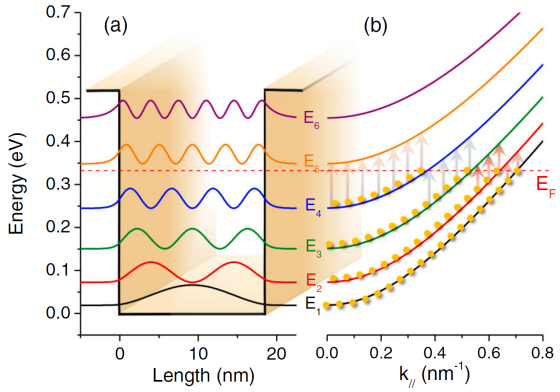


Figure 3.1: The single particle picture of optical absorption in a highly doped quantum well system. [22]

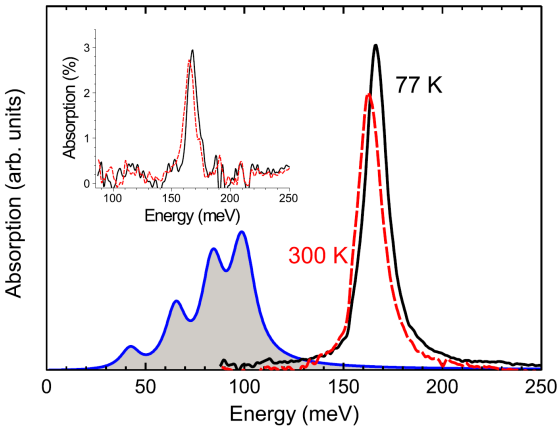


Figure 3.2: Absorption spectra of the doped quantum well measured at 77 K (continuous line) and 300 K (dashed line). The inset presents the 77 K (continuous line) and 300 K (dashed line) spectra measured on the same sample at Brewster angle. The blue line in the main panel represents the simulated absorption spectrum, resulting from a single particle description and Lorentzian line broadening of the allowed transitions. [22]

with

$$H_0 = \int d^3\vec{r}\Psi_e^\dagger(\vec{r}) \left( \frac{\vec{p}^2}{2m^*} + V_e(z) \right) \Psi_e(\vec{r}), \tag{3.2}$$

$$H_{ee} = \frac{1}{2} \int d^3\vec{r} \int d^3\vec{r}' \Psi_e^\dagger(\vec{r}) \Psi_e^\dagger(\vec{r}') V(|\vec{r} - \vec{r}'|) \Psi_e(\vec{r}') \Psi(\vec{r}), \tag{3.3}$$

$$H_{ei} = -\int d^3\vec{r} \int d^3\vec{r}' \Psi_e^\dagger(\vec{r}) \Psi_e(\vec{r}) V(|\vec{r} - \vec{r}'|) \rho_i(\vec{r}'), \tag{3.4}$$

$$H_{ii} = \frac{1}{2} \int d^3\vec{r} \int d^3\vec{r}' \rho_i(\vec{r}) V(|\vec{r} - \vec{r}'|) \rho_i(\vec{r}'), \tag{3.5}$$

where $V_e(z)$ is the confinement potential, $V(|\vec{r} - \vec{r}'|) = e^2/\kappa_0|\vec{r} - \vec{r}'|$ is the Coulomb interaction, and $\rho_i(\vec{r}')$ is the density of ions, which is only a function of z. $\Psi_e(\vec{r}')$ can be expanded using the wave functions which diagonalize $H_0$,

$$\Psi_e(\vec{r}') = \sum_{n\vec{k}} \varphi_n(z) \frac{e^{i\vec{k}\cdot\vec{\rho}}}{\sqrt{A}} a_{n\vec{k}}. \tag{3.6}$$

Then we get

$$H_0 = \sum_{n\vec{k}} \epsilon_{n\vec{k}} a^\dagger_{n\vec{k}} a_{n\vec{k}}, \tag{3.7}$$

$$H_{ee} = \frac{1}{2} \sum_{n_1 n_2 n_3 n_4} \sum_{\vec{k}_3 \vec{k}_4 \vec{q}} V^{ee}_{n_1 n_2 n_3 n_4}(q) a^\dagger_{n_1, \vec{k}_3 - \vec{q}} a^\dagger_{n_2, \vec{k}_4 + \vec{q}} a_{n_4, \vec{k}_4} a_{n_3, \vec{k}_3}, \tag{3.8}$$

$$H_{ei} = -A \sum_{n_1 n_2} \sum_{\vec{k}_2} V^{ei}_{n_1 n_2}(q)\big|_{q=0} \, a^\dagger_{n_1 \vec{k}_2} a_{n_2 \vec{k}_2}, \tag{3.9}$$

$$H_{ii} = \frac{1}{2} A^2 \, V^{ii}(q)\big|_{q=0}, \tag{3.10}$$

where

$$V^{ee}_{n_1n_2n_3n_4}(q) = \int dz \int dz' \varphi^*_{n_1}(z)\varphi^*_{n_2}(z')\frac{2\pi e^2}{\kappa_0 Aq}e^{-q|z-z'|}\varphi_{n_3}(z)\varphi_{n_4}(z'), \tag{3.11}$$

$$V^{ei}_{n_1n_2}(q) = \int dz \int dz' \varphi^*_{n_1}(z)\varphi_{n_2}(z)\frac{2\pi e^2}{\kappa_0 Aq}e^{-q|z-z'|}\rho_i(z'), \tag{3.12}$$

$$V^{ii}(q) = \int dz \int dz' \rho_i(z)\frac{2\pi e^2}{\kappa_0 Aq}e^{-q|z-z'|}\rho_i(z'). \tag{3.13}$$

The q = 0 terms should be interpreted as

$$\begin{aligned}\frac{2\pi e^2}{\kappa_0 Aq}e^{-q|z-z'|}\bigg|_{q=0} &= \lim_{q\to 0}\frac{2\pi e^2}{\kappa_0 Aq}e^{-q|z-z'|} \\ &= V^{2D}(q)\big|_{q=0} - \frac{2\pi e^2}{\kappa_0}|z-z'|,\end{aligned} \tag{3.14}$$

where $V^{2D}(q) = 2\pi e^2/\kappa_0 Aq$ is the two dimensional Fourier transform of the Coulomb potential. So, we can divide the Coulomb interaction Hamiltonian into several terms,

$$\begin{aligned}H_{ee} &= H^{(1)}_{ee} + H^{(2)}_{ee} + H^{(3)}_{ee}, \\ H_{ei} &= H^{(1)}_{ei} + H^{(2)}_{ei}, \\ H_{ii} &= H^{(1)}_{ii} + H^{(2)}_{ii},\end{aligned} \tag{3.15}$$

where the terms are given below,

$$H_{ee}^{(1)} = \frac{1}{2}\, V^{2D}(q)\big|_{q=0} \sum_{n_1 n_2} \sum_{\vec{k}_1 \vec{k}_2} \times a^{\dagger}_{n_1,\vec{k}_1} a^{\dagger}_{n_2,\vec{k}_2} a_{n_2,\vec{k}_2} a_{n_1,\vec{k}_1}, \tag{3.16}$$

$$H_{ee}^{(2)} = -\frac{1}{2} \sum_{n_1 n_2 n_3 n_4} \sum_{\vec{k}_3 \vec{k}_4} \tilde{V}^{ee}_{n_1 n_2 n_3 n_4} a^{\dagger}_{n_1,\vec{k}_3} a^{\dagger}_{n_2,\vec{k}_4} a_{n_4,\vec{k}_4} a_{n_3,\vec{k}_3}, \tag{3.17}$$

$$H_{ee}^{(3)} = \frac{1}{2} \sum_{n_1 n_2 n_3 n_4} \sum_{\vec{k}_3 \vec{k}_4 \vec{q}}^{q\neq 0} V^{ee}_{n_1 n_2 n_3 n_4}(q) a^{\dagger}_{n_1,\vec{k}_3-\vec{q}} a^{\dagger}_{n_2,\vec{k}_4+\vec{q}} a_{n_4,\vec{k}_4} a_{n_3,\vec{k}_3}, \tag{3.18}$$

$$H_{ei}^{(1)} = -N_d\, V^{2D}(q)\big|_{q=0} \sum_{n_1 \vec{k}_1} a^{\dagger}_{n_1\vec{k}_1} a_{n_1\vec{k}_1}, \tag{3.19}$$

$$H_{ei}^{(2)} = A \sum_{n_1 n_2} \sum_{\vec{k}_2} \tilde{V}^{ei}_{n_1 n_2} a^{\dagger}_{n_1\vec{k}_2} a_{n_2\vec{k}_2}, \tag{3.20}$$

$$H_{ii}^{(1)} = \frac{1}{2} N_d^2\, V^{2D}(q)\big|_{q=0}\,, \tag{3.21}$$

$$H_{ii}^{(2)} = -\frac{1}{2} A^2 \tilde{V}^{ii}, \tag{3.22}$$

where

$$\begin{aligned}
\tilde{V}^{ee}_{n_1 n_2 n_3 n_4} &= \int dz \int dz' \varphi^*_{n_1}(z)\varphi^*_{n_2}(z') \frac{2\pi e^2}{\kappa_0 A} |z-z'| \varphi_{n_3}(z)\varphi_{n_4}(z'), \\
\tilde{V}^{ei}_{n_1 n_2} &= \int dz \int dz' \varphi^*_{n_1}(z)\varphi_{n_2}(z) \frac{2\pi e^2}{\kappa_0 A} |z-z'| \rho_i(z'), \\
\tilde{V}^{ii} &= \int dz \int dz' \rho_i(z) \frac{2\pi e^2}{\kappa_0 A} |z-z'| \rho_i(z'),
\end{aligned} \tag{3.23}$$

and $N_d = A\int dz \rho_i(z)$ is the total number of ions, which it is equal to the total number of electrons: $N_d = \sum_{n\vec{k}} n_{n\vec{k}}$, where $n_{n\vec{k}} = \langle a^{\dagger}_{n\vec{k}} a_{n\vec{k}} \rangle$. We can see that if we want to find the total energy of the system, the summation of $H_{ee}^{(1)}$, $H_{ei}^{(1)}$ and $H_{ii}^{(1)}$ vanishes.

In the presence of optical field $\mathcal{E}(t)$, the Hamiltonian contains another term

$$H_{e-ph} = -\mathcal{E}(t) \sum_{n_1 n_2}^{n_1 \neq n_2} \sum_{\vec{k}} \mu_{n_1 n_2}(\vec{k}) a^{\dagger}_{n_1 \vec{k}} a_{n_2 \vec{k}}, \tag{3.24}$$

where $\mu_{n_1 n_2}(\vec{k})$ is the dipole matrix element.

## 3.3 Dynamics of Optical Polarization

In order to get the optical response, we need to calculate the dynamics of the polarization $P_{mn}(\vec{k}) \equiv \langle a^{\dagger}_{m\vec{k}} a_{n\vec{k}} \rangle$. This is given by the Heisenberg equation

$$i\hbar \frac{d}{dt} \langle a^{\dagger}_{m\vec{k}} a_{n\vec{k}} \rangle = \left\langle \left[ a^{\dagger}_{m\vec{k}} a_{n\vec{k}},\ H_0 + H_{e-ph} + H_C \right] \right\rangle, \tag{3.25}$$

where $H_C$ contains all the Coulomb interaction terms. The commutation with $H_0 + H_{e-ph}$ gives

$$\begin{aligned} \left\langle \left[ a^{\dagger}_{m\vec{k}} a_{n\vec{k}},\ H_0 + H_{e-ph} \right] \right\rangle &= P_{mn}(\vec{k}) \left( \epsilon_n(\vec{k}) - \epsilon_m(\vec{k}) \right) \\ &\quad - \mathcal{E}(t) \mu_{nm}(\vec{k}) \left( n_m(\vec{k}) - n_n(\vec{k}) \right) \\ &\quad - \mathcal{E}(t) \sum_{l}^{l \neq m,n} \left( \mu_{nl}(\vec{k}) P_{ml}(\vec{k}) - \mu_{lm}(\vec{k}) P_{ln}(\vec{k}) \right). \end{aligned} \tag{3.26}$$

It shows the intersubband optical polarizations are coupled with each other nonlinearly.

For the commutation with $H_C$, it can be shown the terms corresponding to $H^{(1)}_{ee}$,

$H_{ei}^{(1)}$, $H_{ii}^{(1)}$ and $H_{ii}^{(2)}$ are zero. The commutation with $H_{ee}^{(2)}$ to be

$$
\begin{aligned}
&\left\langle \left[ a^{\dagger}_{m\vec{k}} a_{n\vec{k}},\ H_{ee}^{(2)} \right] \right\rangle \\
&= - \sum_{n_1 n_2 n_3 n_4} \sum_{\vec{k}_3 \vec{k}_4} \tilde{V}^{ee}_{n_1 n_2 n_3 n_4} \left( \delta_{n\vec{k}, n_1 \vec{k}_3} \langle a^{\dagger}_{m\vec{k}} a^{\dagger}_{n_2,\vec{k}_4} a_{n_4,\vec{k}_4} a_{n_3,\vec{k}_3} \rangle + \delta_{m\vec{k}, n_4 \vec{k}_4} \langle a^{\dagger}_{n_1 \vec{k}_3} a^{\dagger}_{n_2,\vec{k}_4} a_{n_3,\vec{k}_3} a_{n,\vec{k}} \rangle \right) \\
&= - \sum_{n_2 n_3 n_4} \tilde{V}^{ee}_{n n_2 n_3 n_4} \langle a^{\dagger}_{m\vec{k}} a_{n_3 \vec{k}} \rangle \sum_{\vec{k}_4} \langle a^{\dagger}_{n_2,\vec{k}_4} a_{n_4,\vec{k}_4} \rangle + \sum_{n_1 n_2 n_3} \tilde{V}^{ee}_{n_1 n_2 n_3 m} \langle a^{\dagger}_{n_2 \vec{k}} a_{n\vec{k}} \rangle \sum_{\vec{k}_3} \langle a^{\dagger}_{n_1,\vec{k}_3} a_{n_3,\vec{k}_3} \rangle \\
&= \left( n_n(\vec{k}) - n_m(\vec{k}) \right) \sum_{n_2} \tilde{V}^{ee}_{n n_2 m n_2} N_{n_2} + \left( n_n(\vec{k}) - n_m(\vec{k}) \right) \sum_{n_2 n_4}^{n_2 \neq n_4} \tilde{V}^{ee}_{n n_2 m n_4} P_{n_2 n_4} \\
&+ P_{mn}(\vec{k}) \left( \sum_{n_1} \tilde{V}^{ee}_{n_1 m n_1 m} N_{n_1} - \sum_{n_2} \tilde{V}^{ee}_{n n_2 n n_2} N_{n_2} \right) \\
&+ \sum_{n_2 \neq m,n} P_{n_2 n}(\vec{k}) \sum_{n_1} \tilde{V}^{ee}_{n_1 n_2 n_1 m} N_{n_1} - \sum_{n_3 \neq m,n} P_{m n_3}(\vec{k}) \sum_{n_2} \tilde{V}^{ee}_{n n_2 n_3 n_2} N_{n_2} \\
&+ \sum_{n_1 n_2 n_3} \tilde{V}^{ee}_{n_1 n_2 n_3 m} P_{n_2 n}(\vec{k}) P_{n_1 n_3} - \sum_{n_2 n_3 n_4} \tilde{V}^{ee}_{n n_2 n_3 n_4} P_{m n_3}(\vec{k}) P_{n_2 n_4},
\end{aligned}
\tag{3.27}
$$

where $P_{n_2 n_4} = \sum_{\vec{k}_4} P_{n_2 n_4}(\vec{k}_4)$, and $N_{n_1} = \sum_{\vec{k}_1} n_{n_1}(\vec{k}_1)$. And the commutation with $H_{ei}^{(2)}$ is

$$
\begin{aligned}
&\left\langle \left[ a^{\dagger}_{m\vec{k}} a_{n\vec{k}},\ H_{ei}^{(2)} \right] \right\rangle \\
&= A P_{mn}(\vec{k}) \left( \tilde{V}^{ei}_{nn} - \tilde{V}^{ei}_{mm} \right) \\
&+ A \sum_{n_2 \neq m,n} \tilde{V}^{ei}_{n n_2} P_{m n_2}(\vec{k}) - A \sum_{n_1 \neq m,n} \tilde{V}^{ei}_{n_1 m} P_{n_1 n}(\vec{k}) \\
&+ \tilde{V}^{ei}_{nm} \left( n_m(\vec{k}) - n_n(\vec{k}) \right).
\end{aligned}
\tag{3.28}
$$

The commutation with exchange interaction $H_{ee}^{(3)}$ is

$$
\begin{aligned}
&\left\langle \left[ a^{\dagger}_{m\vec{k}} a_{n\vec{k}},\ H_{ee}^{(3)} \right] \right\rangle \\
&= \left( n_n(\vec{k}) - n_m(\vec{k}) \right) \sum_{n_2} \sum_{\vec{q}\neq 0} V^{ee}_{nn_2n_2m}(q) n_{n_2}(\vec{k}+\vec{q}) \\
&+ \left( n_n(\vec{k}) - n_m(\vec{k}) \right) \sum_{n_2n_3}^{n_2\neq n_3} \sum_{\vec{q}\neq 0} V^{ee}_{nn_2n_3m}(q) P_{n_2n_3}(\vec{k}+\vec{q}) \\
&+ P_{mn}(\vec{k}) \sum_{n_2} \sum_{\vec{q}\neq 0} \left( V^{ee}_{mn_2n_2m}(q) - V^{ee}_{nn_2n_2n}(q) \right) n_{n_2}(\vec{k}+\vec{q}) \\
&+ \sum_{n_2} \sum_{\vec{q}\neq 0} \left( \sum_{n_1}^{n_1\neq m,n} V^{ee}_{n_1n_2n_2m}(q) P_{n_1n}(\vec{k}) - \sum_{n_4}^{n_4\neq m,n} V^{ee}_{nn_2n_2n_4}(q) P_{mn_4}(\vec{k}) \right) n_{n_2}(\vec{k}+\vec{q}) \\
&+ \sum_{n_1n_2n_3} \sum_{\vec{q}\neq 0} V^{ee}_{n_1n_2n_3m}(q) P_{n_1n}(\vec{k}) P_{n_2n_3}(\vec{k}+\vec{q}) \\
&- \sum_{n_2n_3n_4} \sum_{\vec{q}\neq 0} V^{ee}_{nn_2n_3n_4}(q) P_{mn_4}(\vec{k}) P_{n_2n_3}(\vec{k}+\vec{q}).
\end{aligned}
\tag{3.29}
$$

Group all the terms together, and drop those terms which do not contribute to the optical polarization, we get the equation for intersubband polarization as

$$
\begin{aligned}
&i\hbar \frac{d}{dt} P_{mn}(\vec{k}) \\
&= (\tilde{\epsilon}_n(\vec{k}) - \tilde{\epsilon}_m(\vec{k})) P_{mn}(\vec{k}) + \left( n_n(\vec{k}) - n_m(\vec{k}) \right) \left( \tilde{V}^{ee}_{nmmn} P_{mn} + \sum_{\vec{q}\neq 0} V^{ee}_{nmnm}(q) P_{mn}(\vec{k}+\vec{q}) \right) \\
&- \mathcal{E}(t) \mu_{nm}(\vec{k}) \left( n_m(\vec{k}) - n_n(\vec{k}) \right) - \mathcal{E}(t) \sum_{l}^{l\neq m,n} \left( \mu_{nl}(\vec{k}) P_{ml}(\vec{k}) - \mu_{lm}(\vec{k}) P_{ln}(\vec{k}) \right) \\
&+ \sum_{n_2} \tilde{V}^{ee}_{mn_2n_2m} P_{n_2n}(\vec{k}) P_{mn_2} - \sum_{n_2} \tilde{V}^{ee}_{nn_2n_2n} P_{mn_2}(\vec{k}) P_{n_2n} \\
&+ \sum_{n_1} \sum_{\vec{q}\neq 0} V^{ee}_{n_1mn_1m}(q) P_{n_1n}(\vec{k}) P_{mn_1}(\vec{k}+\vec{q}) - \sum_{n_2} \sum_{\vec{q}\neq 0} V^{ee}_{nn_2nn_2}(q) P_{mn_2}(\vec{k}) P_{n_2n}(\vec{k}+\vec{q}),
\end{aligned}
\tag{3.30}
$$

where

$$\tilde{\epsilon}_n(\vec{k}) = \epsilon_n(\vec{k}) - \sum_{n_2} \tilde{V}^{ee}_{nn_2nn_2} N_{n_2} + A\tilde{V}^{ei}_{nn} - \sum_{n_2}\sum_{\vec{q}\neq 0} V^{ee}_{nn_2n_2n}(q) n_{n_2}(\vec{k}+\vec{q}). \tag{3.31}$$

If we neglect the terms corresponding to exchange interaction, namely those $\vec{q} \neq 0$ terms, and assume parabolic dispersion in each subband with the same effective mass, then we can sum over $\vec{k}$, and get the dynamics of polarization like below

$$\begin{aligned}
& i\hbar \frac{d}{dt} P_{mn} \\
&= \left( \tilde{\epsilon}_n - \tilde{\epsilon}_m + (N_n - N_m)\, \tilde{V}^{ee}_{nmmn} \right) P_{mn} \\
&- \mathcal{E}(t)\mu_{nm}\,(N_m - N_n) - \mathcal{E}(t) \sum_{l}^{l\neq m,n} (\mu_{nl} P_{ml} - \mu_{lm} P_{ln}) \\
&+ \sum_{n_2} \left( \tilde{V}^{ee}_{mn_2n_2m} - \tilde{V}^{ee}_{nn_2n_2n} \right) P_{mn_2} P_{n_2n}.
\end{aligned} \tag{3.32}$$

The last term in the above equation corresponds to the Coulomb contribution to second-order nonlinear optical processes. We will analyze it in the next section.

## 3.4 Three-wave Mixing

In second-order nonlinear optical processes, optical fields with new frequency are generated when lights interact with the matter. We will develop the general case where two optical fields interact with a three-subband system. The three subband are labeled as $|m\rangle$, $|p\rangle$ and $|n\rangle$, and the optical fields are written as

$$\mathcal{E}(t) = \mathcal{E}_{mp} e^{i\omega_{mp}t} + \mathcal{E}_{pn} e^{i\omega_{pn}t}, \tag{3.33}$$

then we have the linear polarization to be

$$P_{mp} = \frac{\mu_{pm}(N_m - N_p)\mathcal{E}_{mp}e^{i\omega_{mp}t}}{\hbar\omega_{mp} - \tilde{\epsilon}_{mp} - i\hbar\gamma_{mp}}, \qquad P_{pn} = \frac{\mu_{np}(N_p - N_n)\mathcal{E}_{pn}e^{i\omega_{pn}t}}{\hbar\omega_{pn} - \tilde{\epsilon}_{pn} - i\hbar\gamma_{pn}}. \tag{3.34}$$

So, the nonlinear polarization at frequency $\omega_{mp} + \omega_{pn}$ is

$$\begin{aligned} P_{mn} = & \frac{\mu_{np}\mu_{pm}\mathcal{E}_{mp}\mathcal{E}_{pn}e^{i(\omega_{mp}+\omega_{pn})t}}{\hbar\omega_{mp} + \hbar\omega_{pn} - \tilde{\epsilon}_{mn} - i\hbar\gamma_{mn}} \\ & \times \left[\frac{N_m - N_p}{\hbar\omega_{mp} - \tilde{\epsilon}_{mp} - i\hbar\gamma_{mp}} - \frac{N_p - N_n}{\hbar\omega_{pn} - \tilde{\epsilon}_{pn} - i\hbar\gamma_{pn}}\right. \\ & \left. - \left(\tilde{V}^{ee}_{mppm} - \tilde{V}^{ee}_{nppn}\right)\frac{(N_m - N_p)}{\hbar\omega_{mp} - \tilde{\epsilon}_{mp} - i\hbar\gamma_{mp}}\frac{(N_p - N_n)}{\hbar\omega_{pn} - \tilde{\epsilon}_{pn} - i\hbar\gamma_{pn}}\right]. \end{aligned} \tag{3.35}$$

Here the first two terms correspond to the conventional nonlinear polarization, while the third term is for the nonlinearity from the intersubband plasmon. An interesting feature is that the three optical fields cannot be in resonant with the transitions simultaneously, this is because the transition energy $\tilde{\epsilon}_{mn} = \tilde{\epsilon}_m - \tilde{\epsilon}_n + (N_m - N_n)\,\tilde{V}^{ee}_{mnnm}$ cannot be expressed as the difference between two definite energy levels. So, we have

$$\begin{aligned} & \tilde{\epsilon}_{mn} - (\tilde{\epsilon}_{mp} + \tilde{\epsilon}_{pn}) \\ & = (N_m - N_n)\,\tilde{V}^{ee}_{mnnm} - (N_m - N_p)\,\tilde{V}^{ee}_{mppm} - (N_p - N_n)\,\tilde{V}^{ee}_{pnnp}, \end{aligned} \tag{3.36}$$

which is usually nonzero. The nonlinear dipole moment is just $\mu_{mn}P_{mn}/L_p$, where $L_p$ is the length of one period of the QW system. So, we get the nonlinear susceptibility

$\chi^{(2)}$ given below,

$$\begin{aligned}\chi^{(2)} = & \frac{\mu_{mn}\mu_{np}\mu_{pm}\mathcal{E}_{mp}\mathcal{E}_{pn}}{\hbar\omega_{mp}+\hbar\omega_{pn}-\tilde{\epsilon}_{mn}-i\hbar\gamma_{mn}} \\ & \times\left[\frac{N_m-N_p}{\hbar\omega_{mp}-\tilde{\epsilon}_{mp}-i\hbar\gamma_{mp}}-\frac{N_p-N_n}{\hbar\omega_{pn}-\tilde{\epsilon}_{pn}-i\hbar\gamma_{pn}}\right. \\ & \left.-\left(\tilde{V}^{ee}_{mppm}-\tilde{V}^{ee}_{nppn}\right)\frac{(N_m-N_p)}{\hbar\omega_{mp}-\tilde{\epsilon}_{mp}-i\hbar\gamma_{mp}}\frac{(N_p-N_n)}{\hbar\omega_{pn}-\tilde{\epsilon}_{pn}-i\hbar\gamma_{pn}}\right]. \end{aligned} \tag{3.37}$$

Now we analyze the effect of intersubband plasmon on the difference-frequency generation (DFG) in a QW structure. The structure was designed by Yong-Hee Cho, and it consists two QWs, with barrier material $Al_{0.48}In_{0.52}As$, well material $Ga_{0.47}In_{0.53}As$, and substrate InP. The energy levels and wave functions for this structure is shown in Fig. 3.3. In Fig. 3.4, we show the dependence of $\chi^{(2)}$ on the doping densities, and contributions from the conventional nonlinear coupling and intersubband plasmon are separated for comparison. As we can see, the $\chi^{(2)}$ increases with doping density for both contributions. So, intersubband plasmon can enhance the DFG efficiency in a QW structure when the doping density is high.

## 3.5 Conclusion

In conclusion, the carriers in a QW structure interact with each other via Coulomb interaction, and it leads to intersubband plasmons. We developed a theory in Hartree-Fock approximation to study the effect of intersubband plasmon on second order nonlinear optical processes. We show that intersubband plasmonic effect can enhance the DFG efficiency, and its contribution increases with doping density.

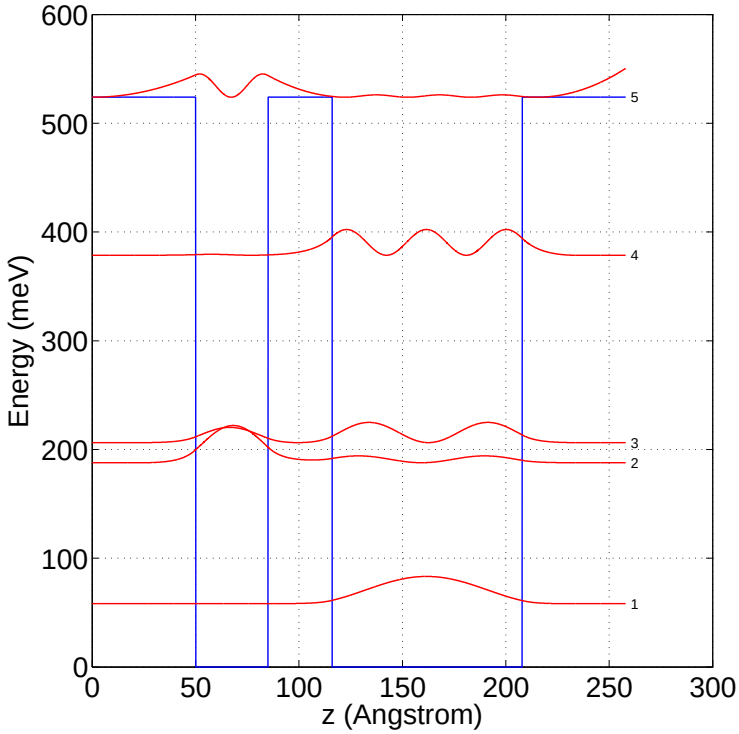


Figure 3.3: The energy levels and wave functions of the QW structure. The device consists $Al_{0.48}In_{0.52}As$ barrier, $Ga_{0.47}In_{0.53}As$ well, and InP substrate. Starting from the barrier, the layer thicknesses of one period is 50/35/31/92, in unit Å. Two optical fields with frequency in resonant with $1 \leftrightarrow 3$ and $2 \leftrightarrow 3$ are used to generate optical field with the difference-frequency.

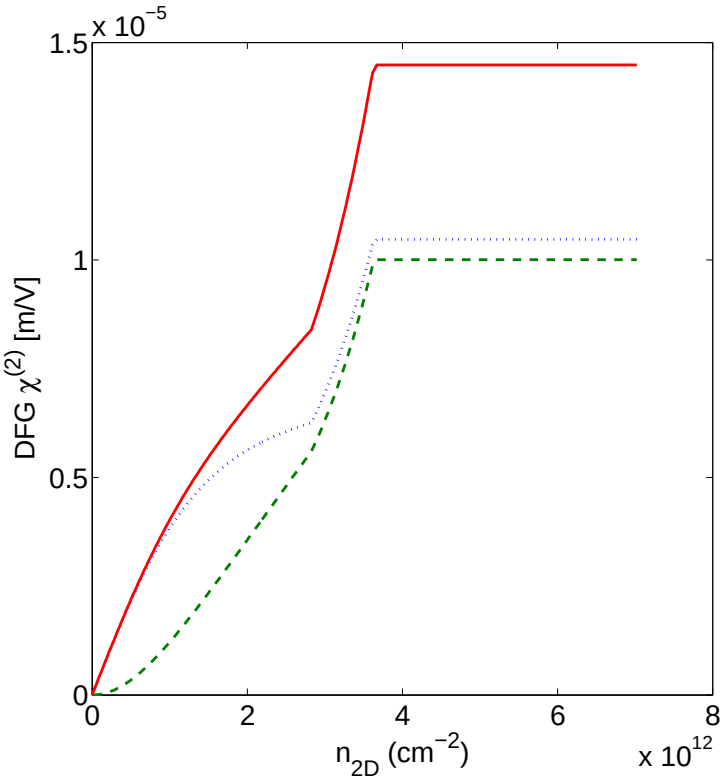


Figure 3.4: The nonlinear susceptibility $\chi^{(2)}$ for the DFG process. Dotted line: conventional nonlinear contribution. Dashed line: intersubband plasmonic contribution. Solid line: Both contributions. The broadening $\hbar\gamma$ is set to be 5 meV. When $n_{2D} = 2.8 \times 10^{12} cm^{-2}$, n = 2 subband becomes occupied, and when $n_{2D} = 3.6 \times 10^{12} cm^{-2}$, n = 3 subband becomes occupied.

# 4. ACTIVE MODE-LOCKING OF MID-INFRARED QUANTUM CASCADE LASERS WITH SHORT GAIN RECOVERY TIME *

## 4.1 Introduction

Generation of ultrashort pulses in mid-infrared (mid-IR) QCLs is one of the last remaining fundamental challenges in QCL physics and laser physics in general. The gain recovery time of a typical QCL is of the order of 1 ps, which is much shorter than the cavity round-trip time of order 50 ps. This effectively prohibits passive mode locking with a saturable absorber of any kind. Indeed, any initial intensity fluctuation in a cavity will quickly get damped if the gain recovers to its small-signal value immediately after the passage of the pulse, leading to preferential amplification of the tails of the pulse.

The situation with active mode locking (AML) is not so obvious, although there is a widespread belief that a long gain recovery time is essential in this case as well. AML has been observed in terahertz QCLs where the gain recovery time is believed to be significantly longer than in the mid-IR QCLs; see e.g. [24, 25]. AML was also observed in two-section mid-IR QCLs of a "super-diagonal" design in which the laser transition is diagonal in real space so that the upper-state lifetime can be as long as 40-50 ps [26, 7]. The latter papers also pointed out that active mode locking in monolithic Fabry-Perot lasers appears to be limited by the spatial hole burning (SHB), i.e. a transient population grating created by a standing wave pattern inside the cavity. Scattering of the laser field off the population grating leads to the proliferation of modes with uncorrelated phases, which destroys single-pulse

*Part of the result reported in this section is reprinted with permission from "Active mode-locking of mid-infrared quantum cascade lasers with short gain recovery time" by Yongrui Wang and Alexey Belyanin, 2015, Optics Express **23**, 4173-4185, Copyright [2015] by the Optical Society of America (OSA).

operation and leads to a chaotic output [26, 7, 27]. To avoid the detrimental effects of the SHB, [28] proposed active modulation of an external ring cavity QCL where the field propagates in only one direction and the population grating is not formed. The active device modeled in [28] was assumed to have a vertical laser transition and a short gain recovery time. Simulations in [28] showed a stable and robust generation of mode-locked pulses, but the pulse duration was very long for modulation at the round-trip period. Reaching the output pulse duration of $\sim 5$ ps required the gain modulation with ultrashort current pulses of 20-30 ps, which would be difficult to synthesize.

The studies in [28] revealed that short gain recovery does not prevent mode locking as long as the net gain window is opened for a short time as compared to the cavity round-trip time. To achieve this, the modulation of only a small part of the laser cavity seems to be crucial. Indeed if the gain responds to modulation instantaneously, modulation of the whole cavity will destroy an isolated pulse as it will experience both gain and loss during each roundtrip. According to our simulations below, in this case the steady-state output is either intensity modulated or simply dies out.

Opening a short gain window is straightforward in an external cavity. However, for many applications a compact monolithic design is preferable. Here we show that generation of mode-locked pulses of a few ps duration is feasible in a monolithic Fabry-Perot cavity even for QCLs with a short gain recovery time, as long as only a short section of the cavity is modulated at the cavity round-trip time. The cavity design is similar to the one employed in [26, 7]. However in contrast to those works we focus on a high-performance active region design with a vertical laser transition and a short gain recovery time. We compare the performance of lasers with long and short gain recovery times and find that standard QCLs with gain relaxation times

of the order of 1 ps are in fact preferable for the AML. Indeed, in super-diagonal lasers electrons accumulate in the upper laser state and the modulation of injection is rather weak. The gain modulation could possibly be achieved by varying bias, which leads to variation of the oscillator strength. However, the DC bias modulation in the active region of a super-diagonal laser is reduced by a strong space charge effect and is accompanied by the modulation of the upper state lifetime and the shift of the intersubband transition energy. These effects can reduce the resulting gain modulation and are not easy to control and utilize. In vertical transition lasers the density of upper-state electrons is much smaller than the electron density in the injector. The dominant effect of the bias modulation is the modulation of injection current and gain.

We use a more realistic model of the QCL active region and transport which includes resonant tunneling injection, electron distribution over in-plane k-vectors, and space charge. We also perform time-domain and space-domain simulations of the propagating field, in which we can directly follow the pulse formation and the pulse instabilities in time. Note that all previous studies cited above used the frequency-domain modal approach and a two- or three-level laser model without current injection. We find the single-pulse operation to be quite robust to the variation of parameters such as the DC bias, bias modulation, and the length of the modulated section. At the same time the phase coherence and pulse duration are sensitive to even slight variations the modulation period: at the level of 0.3%. Moreover the optimal modulation period values for the shortest pulse and longest phase coherence time do not coincide.

## 4.2 The Model of the Active Region and Main Equations

We use a four-subband model to describe the QCL active region. It includes the injector/extractor states (hereafter the ground state), upper laser state, and lower laser state, denoted as $g$, $u$ and $l$, respectively. A schematic diagram of the model and the two-section cavity are shown in Fig. 4.1.

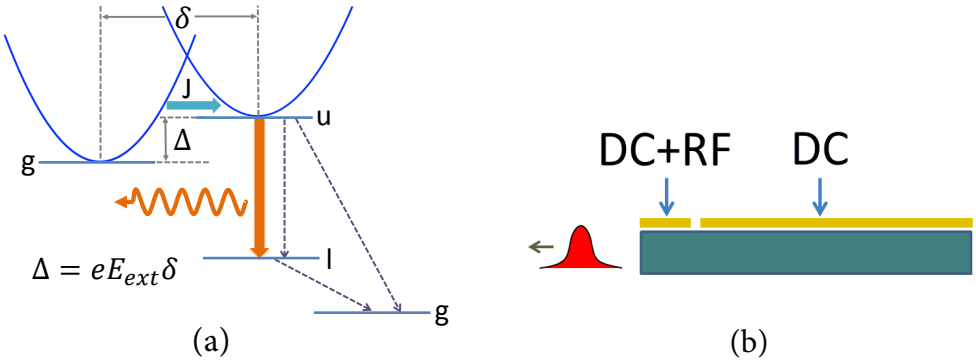


Figure 4.1: (a) A schematic of the active region model. The current $J$ (thick horizontal line) is due to resonant tunneling between aligned $k_{\|}$ states of injector $g$ and the upper laser subband $u$. The distance $\delta$ is the separation between the centroids of electron states in $g$ and $u$, and $\Delta$ is the detuning between the bottoms of these two subbands. The bias electric field is defined to be zero when $g$ and $u$ are aligned. Dashed arrows denote the non-radiative transitions, mostly due to LO phonons. (b) A schematic of a two-section cavity with an RF modulation at the cavity round-trip time applied to a shorter section.

The system dynamics is described by coupled density matrix and Maxwell equa-

tions:

$$
\begin{aligned}
\partial_t n_g &= \frac{n_u}{T_{ug}} + \frac{n_l}{T_{lg}} - J + D\frac{\partial^2 n_g}{\partial z^2} \ , \\
\partial_t n_u &= J - \frac{n_u}{T_{ul}} - \frac{n_u}{T_{ug}} - i\frac{dE}{\hbar}\left(\rho_{ul} - \rho_{ul}^*\right) + D\frac{\partial^2 n_u}{\partial z^2} \ , \\
\partial_t n_l &= \frac{n_u}{T_{ul}} - \frac{n_l}{T_{lg}} + i\frac{dE}{\hbar}\left(\rho_{ul} - \rho_{ul}^*\right) + D\frac{\partial^2 n_l}{\partial z^2} \ , \\
\partial_t \rho_{ul} &= -\left(i\omega + \frac{1}{T_2}\right)\rho_{ul} - i\frac{dE}{\hbar}\left(n_u - n_l\right) \ , \\
\partial_z^2 E - \frac{n^2}{c^2}\partial_t^2 E &= \frac{\Gamma d}{\epsilon_0 c^2 L_p}\partial_t^2(\rho_{ul} + \rho_{ul}^*) \ ,
\end{aligned}
\tag{4.1}
$$

where $n_g$, $n_u$ and $n_l$ are the sheet densities of the corresponding states, $\rho_{ul}$ is the off-diagonal density matrix element for a laser transition, $d$ is the dipole moment, $E$ is the electric field of the laser mode, $n$ is the refractive index, $L_p$ is the thickness of one period, $\Gamma$ is the overlap factor, $\hbar\omega$ is the resonance energy of optical transition, and $D$ is the diffusion coefficient, which we will take to be zero in simulations in order to consider the most unfavorable for AML case of a strong SHB. The injection current $J$ is given by [29]

$$
J = \frac{e\Omega^2\gamma}{\hbar(\Delta^2 + \gamma^2)}\left\{\theta(\Delta)\left(n_g - n_u e^{-|\Delta|/k_B T}\right) + \theta(-\Delta)\left(n_g e^{-|\Delta|/k_B T} - n_u\right)\right\} \ . \tag{4.2}
$$

Here $\Omega$ and $\gamma$ are the coupling energy and the broadening of the states across the injection barrier, $\theta(x)$ is the Heaviside function, and $\Delta$ is the energy detuning from alignment. If we define the bias at alignment to be 0, then $\Delta = eE_{ext}\delta$, where $E_{ext}$ is the bias electric field, and $\delta$ is the separation between the centroids of states $g$ and $u$.

Next, we generalize the ansatzes made in [27]:

$$
\begin{aligned}
E(z,t) &= \frac{1}{2}\left[E_+(z,t)e^{-i(\omega t-kz)} + E_+^*(z,t)e^{i(\omega t-kz)}\right] \\
&+\frac{1}{2}\left[E_-(z,t)e^{-i(\omega t+kz)} + E_+^*(z,t)e^{i(\omega t+kz)}\right] \ , \\
\rho_{ul}(z,t) &= \eta_+ e^{-i(\omega t-kz)} + \eta_- e^{-i(\omega t+kz)} \ , \\
n_g(z,t) &= n_{g0} + n_{g2}e^{2ikz} + n_{g2}^* e^{-2ikz} \ , \\
n_u(z,t) &= n_{u0} + n_{u2}e^{2ikz} + n_{u2}^* e^{-2ikz} \ , \\
n_l(z,t) &= n_{l0} + n_{l2}e^{2ikz} + n_{l2}^* e^{-2ikz} \ ,
\end{aligned} \tag{4.3}
$$

where $k = n\omega/c$. $E_+$ and $E_-$ are amplitudes of the fields traveling in right and left directions respectively. All populations contain the slowly varying average part and the grating part, denoted by subscripts 0 and 2. The injection current $J$ is a linear combination of $n_g$ and $n_u$ when the space charge effect is not included. So, $J(z,t)$ should have the same form as electron populations:

$$
J(z,t) = J_0 + J_2 e^{2ikz} + J_2^* e^{-2ikz} \ . \tag{4.4}
$$

Although we include the space charge in our work, if we ignore the effect of the population grating on energy detuning $\Delta$ as the first order approximation, the conclusion above still holds.

Substituting these expressions into the density matrix equations, and making the slowly varying envelope approximation, we get the following equations for the

envelope functions,

$$\partial_t n_{g0} = \frac{n_{u0}}{T_{ug}} + \frac{n_{l0}}{T_{lg}} - J_0 \ , \tag{4.5}$$

$$\partial_t n_{g2} = \frac{n_{u2}}{T_{ug}} + \frac{n_{l2}}{T_{lg}} - J_2 - 4k^2 D n_{g2} \ , \tag{4.6}$$

$$\partial_t n_{u0} = J_0 - \frac{n_{u0}}{T_{ul}} - \frac{n_{u0}}{T_{ug}} + i\frac{d}{2\hbar}\left[E_+\eta_+^* + E_-\eta_-^* - c.c.\right] \ , \tag{4.7}$$

$$\partial_t n_{u2} = J_2 - \frac{n_{u2}}{T_{ul}} - \frac{n_{u2}}{T_{ug}} - 4k^2 D n_{u2} + i\frac{d}{2\hbar}\left[E_+\eta_-^* - E_-^*\eta_+\right] \ , \tag{4.8}$$

$$\partial_t n_{l0} = \frac{n_{u0}}{T_{ul}} - \frac{n_{l0}}{T_{lg}} - i\frac{d}{2\hbar}\left[E_+\eta_+^* + E_-\eta_-^* - c.c.\right] \ , \tag{4.9}$$

$$\partial_t n_{l2} = \frac{n_{u2}}{T_{ul}} - \frac{n_{l2}}{T_{ug}} - 4k^2 D n_{l2} - i\frac{d}{2\hbar}\left[E_+\eta_-^* - E_-^*\eta_+\right] \ , \tag{4.10}$$

$$\partial_t \eta_+ = -i\frac{d}{2\hbar}\left[\left(n_{u0} - n_{l0}\right)E_+ + \left(n_{u2} - n_{l2}\right)E_-\right] - \frac{\eta_+}{T_2} \ , \tag{4.11}$$

$$\partial_t \eta_- = -i\frac{d}{2\hbar}\left[\left(n_{u0} - n_{l0}\right)E_- + \left(n_{u2}^* - n_{l2}^*\right)E_+\right] - \frac{\eta_-}{T_2} \ , \tag{4.12}$$

$$\left(\frac{n}{c}\partial_t + \partial_z\right)E_+ = i\frac{\Gamma d\omega}{n\epsilon_0 c L_p}\eta_+ - l_w E_+ \ , \tag{4.13}$$

$$\left(\frac{n}{c}\partial_t - \partial_z\right)E_- = i\frac{\Gamma d\omega}{n\epsilon_0 c L_p}\eta_- - l_w E_- \ . \tag{4.14}$$

Here the waveguide loss $l_w$ is added in the equations for the fields. These are the partial differential equations we solve numerically. The derivatives are approximated by the 2nd order expression, e.g. a quantity $f(t)$ is updated at each step as

$$f((n+1)\Delta t) = f(n\Delta t) + \Delta t\dot{f}(n\Delta t) + \frac{1}{2}(\Delta t)^2\ddot{f}(n\Delta t) \ . \tag{4.15}$$

In experiment the laser oscillations in a cavity grow starting from the spontaneous noise, i.e. quantum fluctuations of the field and polarization. To include them in our modeling in a rigorous way we would have to perform second quantization of the field and electrons which would make the problem intractable. To adequately simulate the spontaneous noise we add a complex random source term to the right-

hand side of the polarization equations Eqs. (4.11) and (4.12) which has zero average and is delta-correlated in space and time within the accuracy of the space-time numerical grid. The maximum magnitude of the random source is $\beta n_{u0}/T_{rad}$ where $T_{rad} \simeq 10^{-7}$ s is the spontaneous radiative lifetime of the laser transition and $\beta$ is the small geometric factor measuring the fraction of spontaneous emission coupled to the transverse laser mode. We also added a random delta-correlated electric field along the cavity at the initial moment of time to model initial fluctuations of the field. We performed numerous simulations with different values of the $\beta$ parameter and initial noise. Figure 4.5 below shows one example of simulations for $\beta = 10^{-4}$ and the initial random field of magnitude $10^{-3}$ V/cm. We found that the magnitude of fluctuations only affects the field dynamics during the initial transient stage of the laser field formation. The resulting pulses are not sensitive to the spontaneous noise level. We start observing noticeable changes to the shape of the pulses only when $\beta$ approaches 1.

## 4.3 Base Set of Parameters

For QCLs with a short gain recovery time, the parameters used in our simulation are: (1) Resonant tunneling: $\Omega = 1.5$ meV, $\gamma = 6.58$ meV, $\delta = 10$ nm; (2) Lifetimes: $T_{ul} = 1$ ps, $T_{ug} = 3$ ps, $T_{lg} = 0.1$ ps, $T_2 = 0.05$ ps, $D = 0$; (3) Optical parameters: $n = 3.3$, $l_w = 10$ cm$^{-1}$, $\Gamma = 1$, $d = e \times 2$ nm, $\lambda_0 = 6.2$ $\mu$m; (4) QCL structure parameters: $L_p = 580$ Å, $n_{doping} = 8.0 \times 10^{10}$ cm$^{-2}$, $T_e = 300$ K, cavity length $L_{act} = 3$ mm, facet reflection coefficients $R_l = 0.5$ and $R_r = 0.5$. Those parameters are typical for mid-IR QCLs. The threshold bias field obtained is 8.31 kV/cm below the alignment bias. In this paper, we use the bias at alignment as a reference, defined to be 0, then the threshold bias field is $V_{th} = -8.31$ kV/cm. For a laser with a long gain recovery time $T_{ul} = 50$ ps, three parameters in the active region are different

from the short gain recovery time design, namely $\Omega = 0.15 \times 1.5$ meV, $T_{ul} = 50$ ps, and $T_{ug} = 100$ ps. The corresponding threshold bias is $V_{th} = -9.31$ kV/cm, which is close to the threshold in the $T_{ul} = 1$ ps case.

We choose the modulated section near the left facet, so that the modulation needs to be applied at the cavity round-trip time. The modulated section length is denoted by $l_{mod}$, in units of $L_{act}$. The DC bias $V_{DC}$ is applied to the remaining part of the cavity. The bias on the modulated section is written as

$$V_{Mod} = V_{Mod,DC} + V_{Mod,Amp} \sin\left(2\pi t / T_{mod}\right). \tag{4.16}$$

All biases are normalized to the threshold bias $V_{th}$. The modulation period $T_{mod}$ and all times on the plots are normalized to the phase roundtrip time $T_{round} = 2n_r L_{act}/c = 66$ ps. In order to study the dependence of the QCL performance on modulation parameters, we choose the following base set of parameters: $l_{mod} = 0.1$, $V_{DC} = 1.0$, $V_{Mod,DC} = 1.0$, $V_{Mod,Amp} = 0.5$, and $T_{mod} = 1.0$. We will change only one parameter at a time. Note that the threshold bias $V_{th}$ is negative, so $V > 1$ ($V < 1$) means below (above) threshold.

## 4.4 The Effects of Injection Pumping and Spatial Hole Burning

First, we analyze the effect of resonant tunneling. In previous works [26, 7], the current or gain were assumed to be uniform in each section of the cavity and sinusoidally modulated. This assumption looks reasonable at small modulation amplitudes but becomes problematic with deeper modulation. In particular a large modulation amplitude as compared to the DC pumping level in [7] would create large negative swings in the current and gain, which is unrealistic for QCLs. Here we adopt a more realistic point of view that the injection current to the upper laser state results from electron transport under the applied bias and cannot be directly con-

trolled. We assume that the input parameter that we can control and modulate is an applied bias whereas the current is calculated from Eqs. (4.2) and (5)-(14) assuming the Fermi-Dirac distribution of electrons in the injector with a given temperature $T_e$. In this case a large modulation amplitude would move the injector out of resonance with the upper laser state, thus decreasing the gain but not flipping its sign and not reversing the current.

Figure 4.2 shows the spectrum of the bias, injection current, and gain (c) near the left facet assuming a sinusoidal modulation of the bias at a relatively large amplitude $V_{Mod,Amp} = 0.9$. The zero frequency part has been subtracted, since it only contains information about the average of the corresponding quantities. From this picture we can see that the response of the current to the sinusoidal modulation of the bias is noticeably nonlinear as it contains a number of higher harmonics. For a smaller modulation amplitude $V_{Mod,Amp} = 0.5$ only the second harmonic remains in the spectrum at a magnitude smaller than -10 dB; therefore a sinusoidal modulation of the current would be a reasonable approximation.

The effect of the spatial hole burning (SHB) described by the population and injection current gratings at the half-wavelength period in Eqs. (4.3) and (4.4) is significant, although in contrast to statements in previous studies, we do not find SHB in a monolithic Fabry-Perot cavity to be the main obstacle for the AML. The effect of SHB is more nuanced as illustrated in Figs. 4.3 and 4.4 which show the dependence of the pulse shape on the DC bias for lasers with short and long relaxation time. Here we keep the DC part of the bias in the modulation section $V_{mod,DC}$ equal to the bias in the DC section $V_{DC}$, to minimize the number of free parameters. For a laser with $T_{ul} = 1$ ps, both the intensity and pulse duration increase when the DC bias is increased. Also, rapid oscillations within the pulse envelope are developed at high enough bias. Comparison with simulations carried out in the absence of the

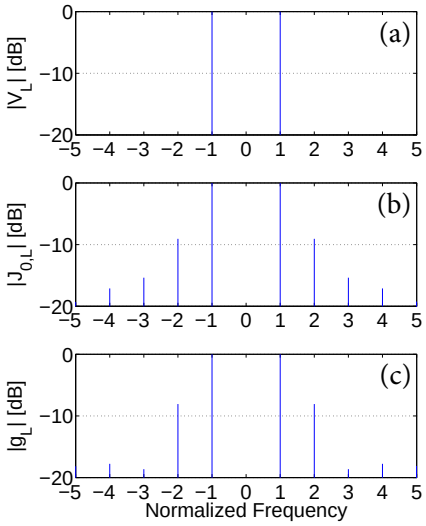


Figure 4.2: The spectrum of the modulated bias (a), injection current (b), and gain (c) at the point adjacent to the left facet. All parameters are taken at base values except for a higher modulation amplitude $V_{Mod,Amp} = 0.9$. Although the modulation of the bias is at a single frequency, the injection current and gain contain higher harmonics.

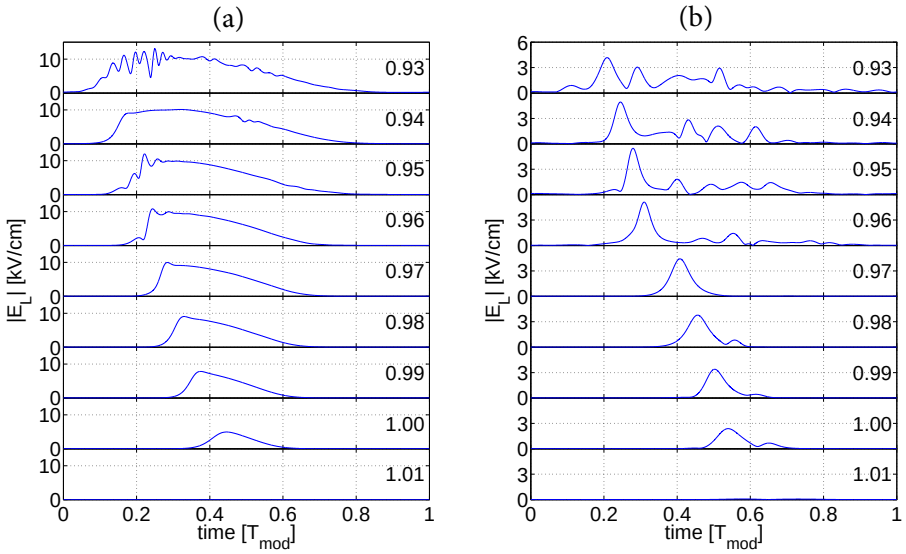


Figure 4.3: The output field amplitude over one roundtrip time taken close to the end of the simulation time for different values of the DC bias $V_{DC}$ in units of threshold bias for lasers with (a) $T_{ul} = 1$ ps and (b) $T_{ul} = 50$ ps. The DC biases in the modulated section and DC section are set to be equal.

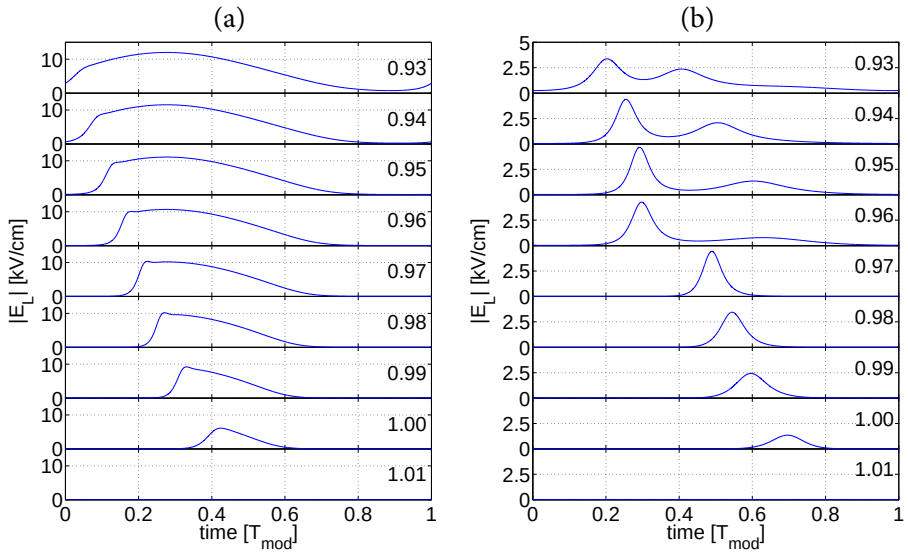


Figure 4.4: Same as Fig. 4.3, but without population grating.

populations grating, $n_{(u,l,g)2} = 0$ and $J_2 = 0$ (Fig. 4.4) show that the substructure is due to the SHB instability because it is not present in the absence of SHB. The same conclusion is true for the case of $T_{ul} = 50\,\text{ps}$, where the multiple pulsations disappear when $n_{(u,l,g)2} = 0$. At the same time, an overall increase in the pulse duration is due to an increase in the net gain window and resulting amplification of the tails of the pulse. We again notice that in a laser with a short gain recovery time the single pulse regime is more robust.

## 4.5 The Effect of the Modulation Period on the Pulse Duration and Phase Coherence

An apparent optimal choice of the modulation period is the phase round-trip time, i.e. normalized $T_{mod} = 1$ in Eq. (4.16). However, this turns out to be not the best choice for the long-time stability of the output. In Fig. 4.5 we plot the output field at the left facet for the whole simulation range of 10,000 roundtrips . As one can see, it takes a long time before the output intensity eventually stabilizes,

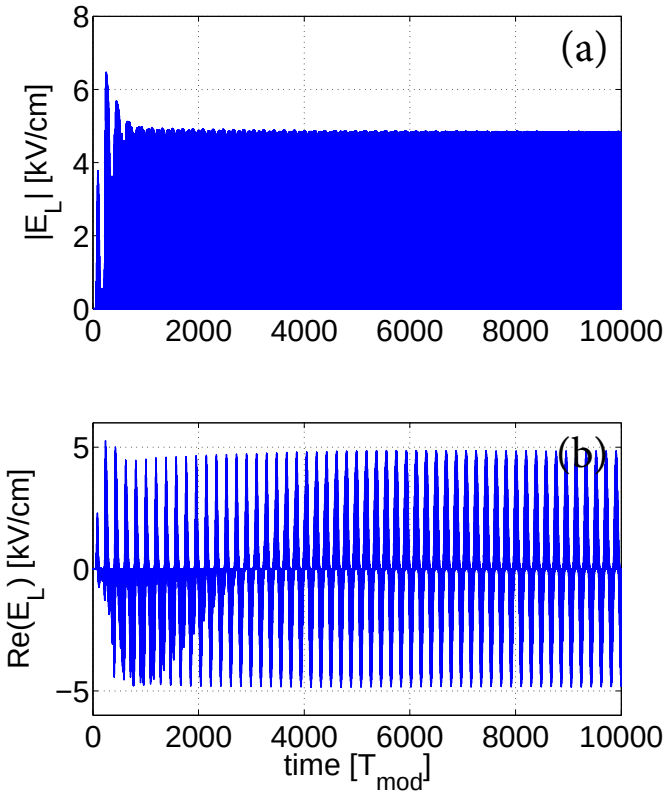


Figure 4.5: (a) The output field amplitude and (b) real part of the field at the left facet for the whole simulation range of 10,000 roundtrips and the base set of parameters. After the output is stable, there are still some small oscillations in the pulse amplitude. The real part of the field is not periodic in the modulation period, indicating that the phase is not locked.

although there is still a slight long-term variation in the magnitude of the pulses. Furthermore, although the amplitude of the output field is nearly periodic, the real (Fig. 4.5(b)) and imaginary (not shown) parts of the field are not. This means that the spectrum of the output field is not phase locked. The autocorrelation function for the real part of the field, defined as

$$R_E(\tau) = \int_{t_1}^{t_2} \mathrm{Re}[E(t)]\mathrm{Re}[E(t+\tau)]dt \Big/ \int_{t_1}^{t_2} \left(\mathrm{Re}[E(t)]\right)^2 dt \quad , \tag{4.17}$$

experiences oscillations between 1 and 0 with a period of about 200 round-trips.

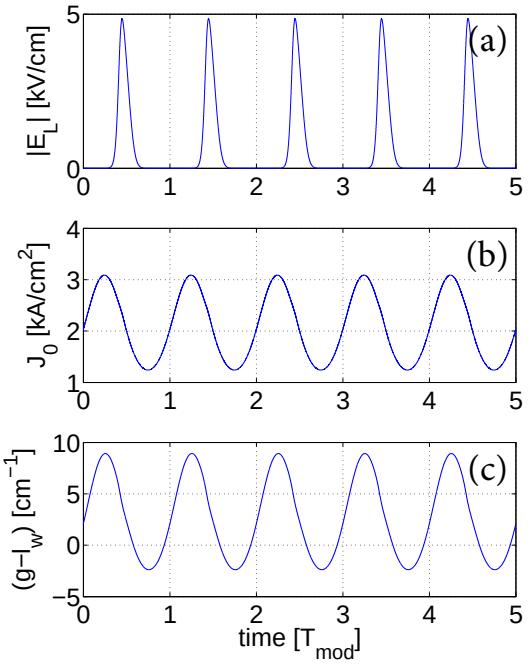


Figure 4.6: (a) The amplitude of the output laser field on the left facet. (b) The injection current at the point adjacent to the left facet. (c) The difference between the gain and waveguide loss $g - l_w$ at the point adjacent to the left facet. The gain follows the injection current almost instantaneously, due to the short gain recovery time. The peak of the pulse has a delay with respect to the maximum of the gain.

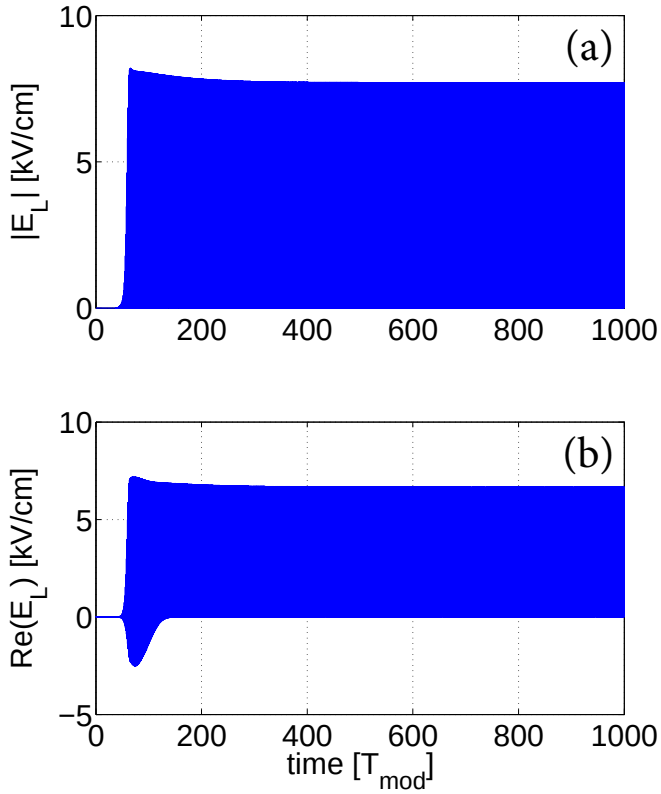


Figure 4.7: (a) The output field amplitude and (b) real part of the field at the left facet over 1,000 roundtrips in a laser with a short gain recovery time for the base set of parameters but a slightly longer modulation period $T_{mod} = 1.003$, which matches the group roundtrip time of the pulse. Both the field amplitude and the real part of the field become strictly periodic after about 200 roundtrips.

To understand the reason for these long-time variations, in Fig. 4.6 we show the output laser field from the left facet for the base set of parameters over the time interval of 5 periods, taken close to the end of the simulation time. Along with the laser field we show the injection current and net waveguide gain $g - l_w$ (excluding mirror losses) near the left facet. The duration of intensity pulses is about 10% of the round-trip time, which is around 7 ps. Although the injection current and gain are shown for a point near the left facet, this point can represent the

whole modulated section since the gain saturation effect is small at these intensities. From Fig. 4.6(a) we can see that the gain follows the injection current, while the peak of the pulse is delayed with respect to the gain maximum, namely the pulse is experiencing the tailing edge of the gain. This can be explained by the fact that the group velocity of the pulse is smaller than the phase velocity and therefore the gain modulation is slightly out of phase with the circulating pulse. Therefore, the gain modulation is slightly out of resonance with the circulating pulse which causes long-period oscillations in the output.

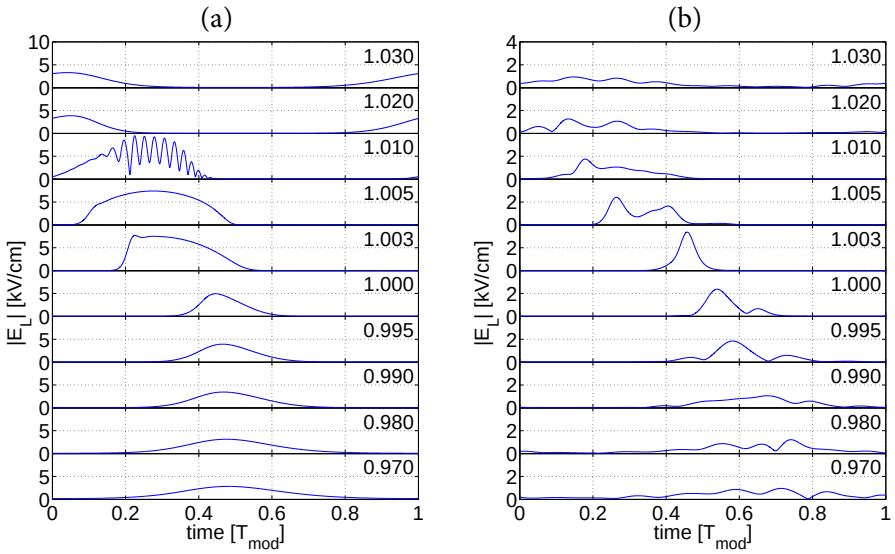


Figure 4.8: The output field amplitude over one roundtrip time taken close to the end of the simulation time for different values of the modulation period $T_{mod}$ measured in units of phase roundtrip time for lasers with (a) $T_{ul} = 1$ ps and (b) $T_{ul} = 50$ ps and the base set of parameters.

To eliminate the phase mismatch we slightly increase the modulation period to $T_{mod} = 1.003$ to compensate for the group delay of the pulses. As shown in Fig. 4.7, this leads to the stable output after the laser field build-up time of about 200 round-

trips. Moreover, the real and imaginary parts of the field are also exactly periodic as can be verified by the autocorrelation function which has a constant value equal to 1. At the same time, the pulse duration is longer in this case as illustrated in Fig. 4.8 which shows the pulse shape as a function of the modulation period $T_{mod}$. When $T_{mod} = 1$, the pulses generated by a laser with a short gain recovery time have the shortest duration. When $T_{mod} = 1.003$, the intensity of the pulse increases significantly as it has the best overlap with the maximum of the gain in a modulated section. At the same time, the time window of the net gain is increased in this case, leading to a longer pulse duration.

## 4.6 The Output Dependence on the Modulation Amplitude and Length of the Modulated Section

Two other parameters that strongly affect the output pulses are the modulation amplitude and length of the modulated section. Figure 4.9 shows the effect of varying modulation amplitude. As expected, for both $T_{ul} = 1$ ps and $T_{ul} = 50$ ps cases, the peak intensity of the pulse increases with the modulation amplitude. At the same time, the pulse becomes more asymmetric in the $T_{ul} = 1$ ps case, which is the result of the phase mismatch between the modulation period and group round-trip time. For a laser with a long gain recovery time, the $T_{mod} = 1$ modulation period is closer to resonance with the group round trip time and the pulses are more symmetric. Also the gain saturation effect is stronger, so the tailing edge of pulse is not amplified.

With increasing length of the modulated section, the pulse experiences a stronger round-trip gain but at the same time the window of the net gain becomes wider which leads to the pulse broadening. Fig. 4.10 shows the dependence of the output on the length of a modulated section. In the $T_{ul} = 1\,\text{ps}$ case, when $l_{mod}$ increases from 0.1 to 0.5, the intensity and duration of the pulse increase at the same time. For longer

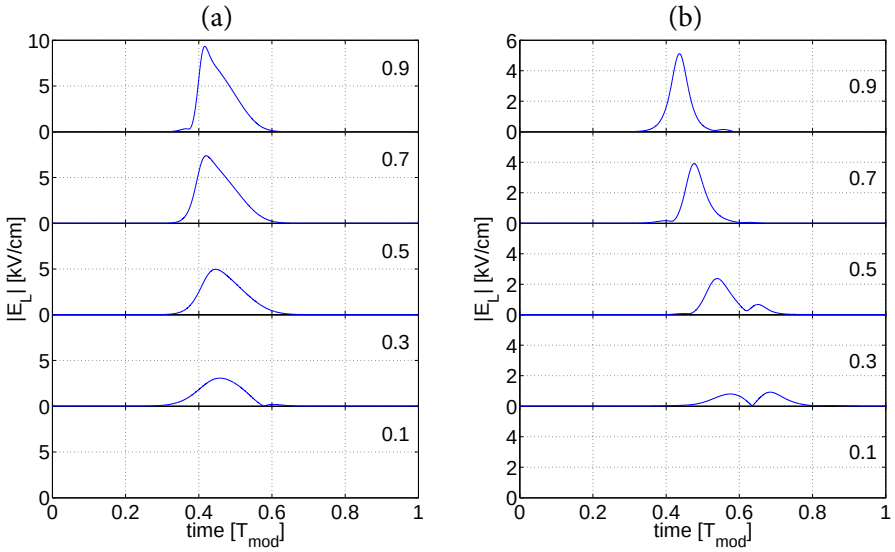


Figure 4.9: The output field amplitude over one roundtrip time taken close to the end of the simulation time for different values of the modulation amplitude $V_{Mod,Amp}$ in Eq. (4.16), measured in units of threshold bias for lasers with (a) $T_{ul} = 1\,\text{ps}$ and (b) $T_{ul} = 50\,\text{ps}$ and the base set of parameters. No significant output is generated when $V_{Mod,Amp} \leq 0.1$.

$l_{mod}$ the pulse eventually broadens to the whole cavity and its peak intensity drops. However, the pulsation still exists even when the modulated section is 90% of the whole chip. In the $T_{ul} = 50\,\text{ps}$ case, one only gets a good pulse around $l_{mod} = 0.3$, and this pulse is shorter as compared to the $T_{ul} = 1\,\text{ps}$ design. However, with increasing $l_{mod}$ the output quickly turns into multiple chaotic pulsations. It is indeed expected that a laser with a long population relaxation time comparable to the round-trip time is more prone to instabilities than the laser with a short recovery time in which the pulsations of the population inversion are strongly damped.

When the whole QCL cavity is modulated, no isolated pulses are obtained in both cases, and only the intensity is modulated. We checked that this conclusion remains true for the parameters typical for THz QCLs. The observation of isolated pulses in [24, 25] could be the result of the nonuniform injection of modulated pumping along

the cavity. Indeed the THz waveguide forms a microstrip transmission line for the microwave modulation which forms a standing wave along the cavity.

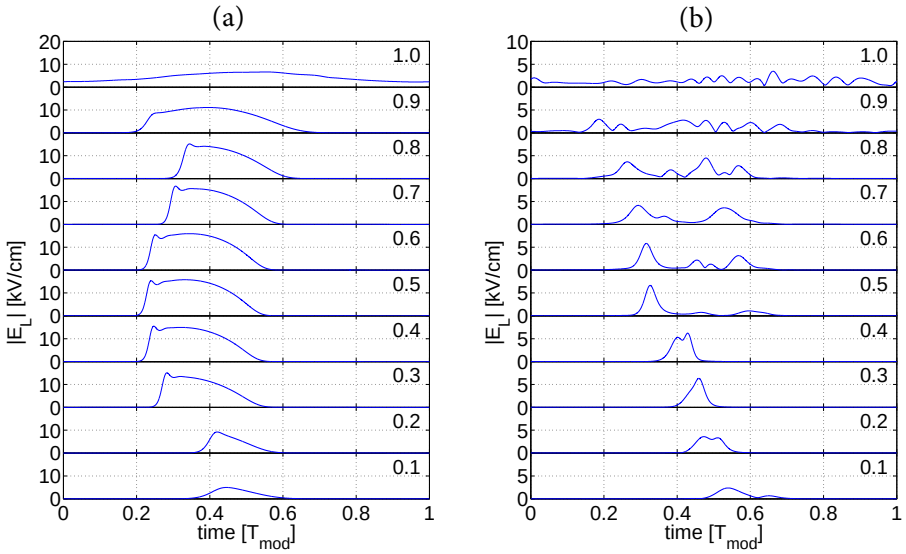


Figure 4.10: The output field amplitude over one roundtrip time taken close to the end of the simulation time for different lengths of the modulated section $l_{mod}$ measured in units of the total cavity length $L_{act}$ for lasers with (a) $T_{ul} = 1$ ps and (b) $T_{ul} = 50$ ps and the base set of parameters.

## 4.7 Conclusion

In conclusion, we showed that standard high-performance mid-IR QCLs with a short gain recovery time can be actively modulated to generate mode-locked pulses of a few ps duration when the modulation is applied only to a short section of a monolithic Fabry-Perot cavity to create a net gain window for a circulating pulse. The performance of QCL with a short gain recovery time is more robust to varying parameters as compared to QCLs with a long gain recovery time. By fine tuning the modulation period to the group round-trip time of the pulse, one can phase lock the

electric field of the pulse and use its spectrum as a frequency comb.

The peak power of the generated pulses grows with increasing modulation amplitude and DC bias, but is limited by the concomitant pulse broadening due to widening gain window, as is seen in Figs. 4.9 and 4.3. For a base set of parameters the peak power of the pulses is about 16 times higher than the CW output power for the DC bias equal to the time-averaged modulated bias of Eq. (4.16).

# 5. CONTINUOUS-WAVE LASING BETWEEN LANDAU LEVELS IN GRAPHENE *

## 5.1 Introduction

Free nonrelativistic electrons in a magnetic field behave as a system of harmonic oscillators, with selection rules allowing only the transitions between neighboring states with equal probabilities. Therefore they cannot be used as an active medium for lasers and masers. One way to get around this limitation is to accelerate electrons to high enough speeds that the relativistic effects become important. This leads to an anharmonicity in the electron spectrum and possibility of the maser action by accelerated electron beams, which has been so impressively implemented in vacuum electronic devices such as gyrotrons [30]. Free carriers in semiconductors seem to offer a similar opportunity as the electron dispersion can show significant nonparabolicity above the bottom of the conduction band. Moreover, semiconductors offer a flexibility to grow heterostructures with different cyclotron transition energies which could be used for carrier injection into a given LL; see the proposal for a LL laser in the quantum Hall regime [31]. In practice, however, ultrafast energy and momentum relaxation in semiconductors would quickly destroy population inversion between the Landau levels (LLs). Although Landau level quantization does help with reducing scattering rate and improving performance of quantum cascade lasers [32] that operate through population inversion between quantum well subbands, the only "solid state gyrotrons" so far are p-Ge lasers operating between light-hole LLs at liquid helium temperatures in strong electric and magnetic fields [33, 34].

*Part of the result reported in this section is reprinted with permission from "Continuous-wave lasing between Landau levels in graphene" by Yongrui Wang, Mikhail Tokman, and Alexey Belyanin, 2015, Phys. Rev. A **91**, 033821, Copyright [2015] by the American Physical Society (APS).

Graphene seems to be an ideal material for the realization of LL lasers. Low energy excitations near the Dirac points in graphene have a linear conical spectrum which is obviously extremely nonparabolic. In a transverse magnetic field the 2D conical spectrum splits into a series of non-equidistant LLs with energies scaling as a square root of the magnetic field and the principal quantum number. It was suggested in [35] that the optical pumping to an arbitrary excited state $n \geq 1$ will lead to electrons cascading down the LLs preferentially emitting photons, which would potentially lead to the EM field amplification on any of these downward transitions. Unfortunately, the proposal [35] assumed that the radiative transitions are the fastest ones in graphene. It did not include most important nonradiative relaxation channels and did not attempt to calculate actual LL populations. In particular, it turns out that the Auger relaxation is a very powerful relaxation mechanism for Dirac electrons in a magnetized graphene that proceeds much faster than radiative transitions and washes out any population inversion over the time scale of few ps; see below and also recent theoretical calculations of the Auger relaxation rate [36] and experimental measurements in [37]. A recently proposed, more sophisticated pumping scheme [38] takes into account Auger relaxation processes and still leads to only a transient population inversion existing over a ps timescale.

Here we propose what we believe is a viable LL laser scheme for graphene that takes into account all relevant relaxation processes and in fact utilizes them to reach a steady-state population inversion, vital for any viable laser. Our scheme is transferable to thin ($\lambda \gg \Delta z \geq 5$ nm) films of 3D topological insulators such as $Bi_2Se_3$ where the Landau levels associated with massless metallic surface states [39, 40] should demonstrate similar coupling to the EM field despite different chirality [41]. Note that our scheme provides the population inversion *in a steady state*, i.e. under a continuous-wave pumping, in contrast to previous proposals, with or without the

magnetic field, that could provide only a transient gain during a picosecond time interval [35, 42, 38].

We solve kinetic and density matrix equations coupled with Maxwell's equations to calculate populations, gain and laser threshold conditions as a function of the optical pumping power. The calculation details are in the sections below. Here we present a general idea of the laser scheme. It is illustrated in Fig. 1. It shows one specific implementation of the scheme with an optical pumping originated from level $n = -2$ to obtain maximum population inversion between levels $-1$ and $-2$. However, the scheme can be implemented for any pair of LLs $(-n, -n-1)$ as long as level $-n$ stays deep enough below the Fermi level. The lasing wavelength can be from sub-THz to the mid-infrared range, depending on the value of $n$, the magnetic field, and the substrate used.

The general idea is as follows. In the equilibrium (without pumping) levels $n = -1$ and $-2$ are fully occupied to degeneracy surface density $N_s = g_s g_v / 2\pi {l_c}^2$, where spin and valley degeneracy factors are $g_s = 2$ and $g_v = 2$ for graphene, and $l_c = \sqrt{c\hbar/eB}$ is the magnetic length. The Fermi level is placed at the Dirac point in the figure, assuming intrinsic graphene. However, this can be changed, as long as level $n = -1$ is fully occupied in equilibrium. An optical pumping resonant to the transition $-2 \to 1$ moves part of the carriers up from level $n = -2$ creating a population inversion between a fully occupied level $n = -1$ and level $-2$. In order for this population inversion to exist in a steady state, i.e. under a continuous-wave optical pumping, the relaxation of carriers back to lower laser state $-2$ should be slower than the relaxation rate to the upper laser state $-1$. Unfortunately, the Auger mechanism does not satisfy this criterion. Our simulations show that there is no population inversion in the steady state, no matter how strong the optical pumping power is. This is because an increase in the depopulation rate of level $-2$

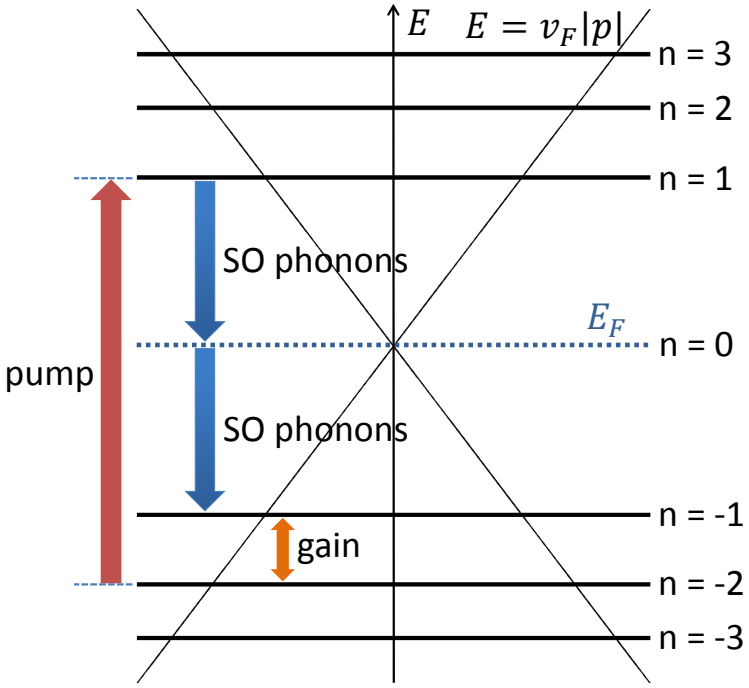


Figure 5.1: The scheme to obtain population inversion between the electron states below the Fermi level by using a continuous-wave optical pumping. Electrons excited by a pump preferentially relax to the upper laser state $-1$ due to resonant emission of surface optical phonons at the graphene-substrate interface.

by an optical pumping is compensated by an increase in the Auger scattering rate to level 2, primarily through the scattering of electrons from states in levels 1 and $-1$ to states in levels 2 and $-2$, respectively. In order to overcome this obstacle, the magnetic field needs to be tuned in order to bring the transitions $1 \to 0$ and $0 \to -1$ (of the same energy) in resonance with an LO phonon energy. This will greatly increase the rate of electron relaxation from excited states to the upper laser state $n = -1$ through LO phonon emission, whereas the transitions to state $-2$ will be out of resonance and not affected much.

The LO phonon energy in graphene is close to 200 meV, which would require a magnetic field of almost 30 T to bring the transition frequency $\omega_{10}$ close to $\omega_{LO}$. In order to reduce the required magnetic field one can utilize the scattering on bulk, surface, or interface optical phonons of the substrate, and choose the substrate with a lower optical phonon energy, for example a polar semiconductor such as GaAs or InGaAs [43]. For definiteness, below we assume the substrate to be GaAs, which leads to the surface optical (SO) phonon energy of $\hbar\omega_{SO} = 36$ meV [44]. This is equal to $\omega_{01} = \omega_c = \sqrt{2}v_f/l_c$ in a magnetic field of 1 T. The laser transition wavelength would be then around 82 $\mu$m, i.e. around 3 THz, which is the range where there is a shortage of laser sources. We will also assume the optical pumping between levels $-2$ and 1, although the pumping resonant to the transition from $-2$ to 3 would be equally efficient and lead to a similar value for the gain. Moreover, the transition frequency for the latter transition in a magnetic field of 1 T would correspond to a $CO_2$ laser wavelength around 10 $\mu$m, which could be more convenient than the 14-$\mu$m wavelength corresponding to the transition $-2 \to 1$. Of course all energies can be changed as needed by choosing different substrates or different LLs for the lower laser state, for example $n = -3$ instead of $-2$.

The scheme in Fig. 1 provides population inversion between hole states $-1$ and

$-2$. Its "mirror image" provides a similar population inversion between electron states 1 and 2 when the optical pump is applied between states $-1$ and 2. In this case the SO phonons depopulate the lower laser state instead of populating the upper one.

## 5.2 Electron States and Optical Transitions between the Landau Levels in Graphene

For completeness, we give a brief summary of the electron states and optical transitions between the LLs in graphene, since this information is extensively used below. They have been calculated many times before and observed both in monolayer and multilayer samples [45].

Neglecting intervalley scattering, we will only need electron states in one of the two equivalent $K, K'$ valleys, for example the $K$ valley. Without a magnetic field, the low-energy Hamiltonian in the vicinity of the $\vec{K}$ Dirac point is given by [46]

$$H = v_F \vec{\sigma} \cdot \hat{\vec{p}} = v_F \begin{pmatrix} 0 & \hat{p}_x - i\hat{p}_y \\ \hat{p}_x + i\hat{p}_y & 0 \end{pmatrix}, \tag{5.1}$$

where $v_F = 10^8$ cm/s. In the presence of a transverse magnetic field or any EM field described by the vector-potential $A$, we replace $\hat{\vec{p}}$ with $\hat{\vec{\Pi}} = \hat{\vec{p}} + e\vec{A}/c$. For a magnetic field in the $+z$ direction, we can write $\vec{A} = (0,\ Bx,\ 0)$ in the Landau gauge, then the eigenfunctions are expressed as [47]

$$F^K_{nk}(\vec{r}) = \frac{1}{\sqrt{L}} e^{iky} \Phi_n(k, x), \tag{5.2}$$

with

$$\Phi_n(k,x) = C_n \begin{pmatrix} \mathrm{sgn}(n) i^{|n|-1} \phi_{|n|-1}(x + l_c^2 k) \\ i^{|n|} \phi_{|n|}(x + l_c^2 k) \end{pmatrix}, \tag{5.3}$$

where $C_n = 1$ when n = 0, and $C_n = 1/\sqrt{2}$ when n $\neq$ 0; sgn($x$) = 1, 0, $-1$ for x $>$ 0, x = 0, x $<$ 0 respectively. The function $\phi_{|n|}(x)$ has the same form as the eigenfunction in the massive electron case:

$$\phi_{|n|}(x) = \frac{1}{\sqrt{2^{|n|}|n|!\sqrt{\pi} l_c}} \exp\left[-\frac{1}{2}\left(\frac{x}{l_c}\right)^2\right] H_{|n|}\left(\frac{x}{l_c}\right), \tag{5.4}$$

where $H_{|n|}(x)$ is the Hermite polynomial. The corresponding eigenenergy is $\epsilon_n$ = sgn($n$)$\hbar\omega_c\sqrt{|n|}$, with $\omega_c = \sqrt{2} v_f / l_c$.

In this manuscript, an electron state will be labeled by $|n, k, s, \xi\rangle$, where s = $\{\uparrow, \downarrow\}$ denotes spin, $\xi = \{K, K'\}$ denotes valley; $k$, $s$, $\xi$ are degenerate quantum numbers, and the total degeneracy density of a Landau level $n$ is $2/\pi l_c^2$.

The interaction Hamiltonian for an optical field with an in-plane polarization can be written as

$$\hat{H}_{int}^{op} = v_F \frac{e}{c} \vec{\sigma} \cdot \vec{A}^{op}, \tag{5.5}$$

where $\vec{A}^{op}$ is the vector potential of the optical field, which is related to the electric field by $\vec{E}^{op} = (-1/c)\partial\vec{A}^{op}/\partial t$. If we define two circular polarization vectors, $\hat{l}_\oplus = (\hat{x} + i\hat{y})/\sqrt{2}$ and $\hat{l}_\ominus = (\hat{x} - i\hat{y})/\sqrt{2}$, the vector potential of a single frequency optical field can be written as

$$\vec{A}^{op} = \frac{1}{2}\left(A_\oplus \hat{l}_\oplus + A_\ominus \hat{l}_\ominus\right) e^{-i\omega t} + c.c.\ . \tag{5.6}$$

Plugging this expression into the Schrödinger equation and using the rotating wave approximation, we get the same selection rules as in [48]: Transitions between $n_1$ and $n_2$ ($n_2 > n_1$) are coupled by photons with $\hat{l}_{\oplus}$ polarization if $|n_2| = |n_1| + 1$, and with $\hat{l}_{\ominus}$ polarization if $|n_2| = |n_1| - 1$.

By expressing $\vec{A}^{op}$ through $\vec{E}^{op}$ in $\hat{H}^{op}_{int}$, we can get the magnitude of the dipole moment for a resonant transition between Landau levels $n_1$ and $n_2$:

$$|\mu_{n_1 n_2}| = \sqrt{2} C_{n_1} C_{n_2} e v_F / \omega \ . \tag{5.7}$$

The two dimensional linear optical susceptibility near the resonance to the transition between $n_1$ and $n_2$ ($n_1 < n_2$) is

$$\chi_{n_1 n_2} = \frac{2}{\pi l_c^2} \frac{|\mu_{n_1 n_2}|^2 (f_{n_2} - f_{n_1})}{\hbar\omega - (\epsilon_{n_2} - \epsilon_{n_1}) + i\hbar/T_2}, \tag{5.8}$$

where $T_2$ is the phenomenological dephasing time, which we take to be equal to 100 fs. It is strongly affected by disorder. The gain at resonance scales $\propto T_2$ so it is important to maximize this time. The factors $f$ in the numerator are occupation numbers of given Landau levels. The optical transition rate between $n_1$ and $n_2$ ($n_1 < n_2$) is

$$\Gamma^{op}_{n_1 n_2} = \frac{1}{2} \left| \frac{\mu_{n_1 n_2} E^{op}}{\hbar} \right|^2 \frac{1/T_2}{(1/T_2)^2 + ((\epsilon_{n_2} - \epsilon_{n_1})/\hbar - \omega)^2} \ . \tag{5.9}$$

## 5.3 Laser Threshold Condition

To determine the threshold condition for a LL graphene laser we consider the simplest geometry resembling a quantum-well vertical cavity laser, in which an active layer consisting of one or several graphene monolayers on a polar substrate is located

between the two mirrors of given reflection factors $r_{1,2}$; see Fig. 2. We will assume that there are two media with dielectric constants $\kappa_1$ and $\kappa_2$ from both sides of the active layer. We will also assume for simplicity that the thickness of an active layer is much smaller than the wavelength of the THz laser field. For a field of amplitude $E_i$ incident on the graphene layer, the amplitudes of reflected and transmitted waves $E_r$ and $E_t$ can be related using the Maxwell's equations with proper boundary conditions as

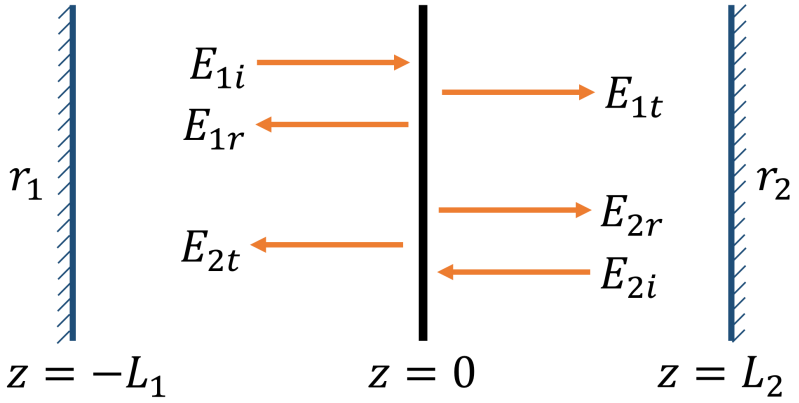


Figure 5.2: A vertical-cavity configuration of the graphene laser.

$$E_t = \frac{2}{1+\sqrt{\frac{\kappa_2}{\kappa_1}}-\frac{4\pi i\omega}{\sqrt{\kappa_1}c}\chi}E_i,$$
$$E_r = \left(\frac{2}{1+\sqrt{\frac{\kappa_2}{\kappa_1}}-\frac{4\pi i\omega}{\sqrt{\kappa_1}c}\chi}-1\right)E_i\ . \tag{5.10}$$

To make equations even simpler, we will take $\kappa_1 = \kappa_2 = \kappa$. It is straightforward to include more complex cavity structures if needed for a particular design.

The fields also need to satisfy the boundary conditions at the mirrors:

$$E_{1i}e^{-ikL_1} = r_1(E_{1r} + E_{2t})e^{ikL_1},$$
$$E_{2i}e^{-ikL_2} = r_2(E_{1t} + E_{2r})e^{ikL_2} \ . \tag{5.11}$$

From the boundary conditions Eqs. (5.10) and (5.11), the condition to have stable nonzero optical fields inside the cavity is

$$-\frac{2\pi i\omega}{\sqrt{\kappa}c}\chi = \frac{r_1r_2 - e^{-2ik(L_1+L_2)}}{r_1r_2 + r_1e^{-2ikL_2} + r_2e^{-2ikL_1} + e^{-2ik(L_1+L_2)}} \ . \tag{5.12}$$

To get the threshold, we assume that the optical fields are in resonance with respective transitions and the lengths $L_1$ and $L_2$ are adjusted so that every term in the denominator has the same sign. Then the minimum required imaginary part of the susceptibility in the active layer can be found from the real part of Eq. (5.12):

$$-\frac{2\pi\omega}{\sqrt{\kappa}c}\mathrm{Im}[\chi] = \frac{1 - |r_1r_2|}{1 + |r_1| + |r_2| + |r_1r_2|} \ . \tag{5.13}$$

We will discuss the feasibility of reaching the lasing threshold below, after calculating the rates of scattering processes, the non-equilibrium populations of the LLs, and the resulting graphene susceptibility at the laser transition in the presence of an optical pumping.

The carriers excited by an optical pumping relax through a variety of scattering processes. The steady state populations are determined by a balance between relaxation and the continuous wave pumping. In the next two sections we give a detailed description of most important processes that determine the redistribution of populations and the resulting steady-state gain.

## 5.4 Auger processes

A strong magnetic field suppresses scattering processes due to energy quantization and reduction in the phase space available for scattered carriers. However, Auger processes remain very efficient: due to the symmetry between electron and hole LLs there is always resonance for scattering of carriers from $(0,0)$ LLs into $(1,-1)$ states and for all other combinations allowed by the energy conservation: $(1,-1) \leftrightarrow (2,-2)$, $(0,0) \leftrightarrow (2,-2)$, $(-1,1) \leftrightarrow (2,-2)$, etc.; see Fig. 3. Recently the Auger relaxation rates were measured to be in a few ps range in pump-probe experiments [37], which agrees with our simulations. Below we outline the general derivation of the Auger scattering rate and then apply it to our problem.

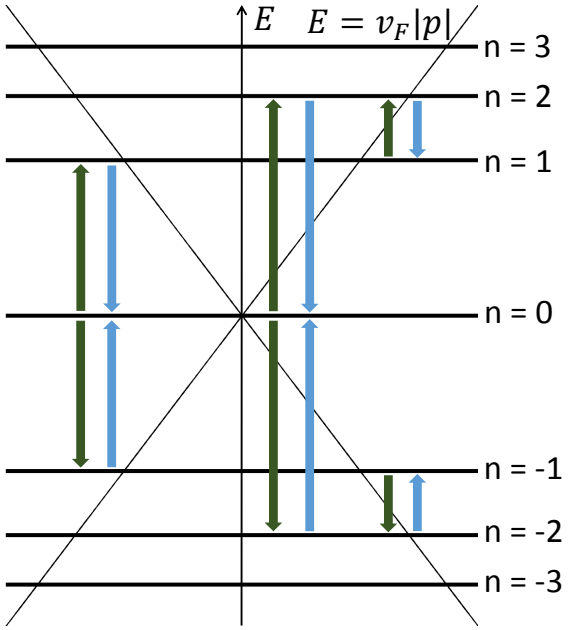


Figure 5.3: Examples of the Auger scattering processes between $n = 0, \pm 1, \pm 2$ LLs.

### *5.4.1 General formulas*

Auger processes are mediated by the Coulomb interaction between carriers. The general Coulomb interaction Hamiltonian for electrons can be written as [49]

$$V_C = \frac{1}{2} \sum_{\alpha\beta\gamma\delta} V_{\alpha\beta\gamma\delta} a^\dagger_\alpha a^\dagger_\beta a_\delta a_\gamma, \tag{5.14}$$

where

$$V_{\alpha\beta\gamma\delta} = \langle\alpha(1)|\langle\beta(2)|V_{Coul}(\vec{r}_1 - \vec{r}_2)|\gamma(1)\rangle|\delta(2)\rangle \ . \tag{5.15}$$

In order to simplify this expression and include the effect of screening, we expand $V_{Coul}(\vec{r}_1 - \vec{r}_2)$ in Fourier series

$$V_{Coul}(\vec{r}_1 - \vec{r}_2) = \sum_{\vec{q}} V_{\vec{q}} \ e^{i\vec{q}\cdot(\vec{r}_1 - \vec{r}_2)}, \tag{5.16}$$

where $V_{\vec{q}} = 2\pi e^2/\kappa_0 A q$ for a 2-dimensional case. Using this expression, we get

$$V_{\alpha\beta\gamma\delta} = \sum_{\vec{q}} V_{\vec{q}} \langle\alpha(1)|e^{i\vec{q}\cdot\vec{r}_1}|\gamma(1)\rangle\langle\beta(2)|e^{-i\vec{q}\cdot\vec{r}_2}|\delta(2)\rangle \ . \tag{5.17}$$

To include screening by carriers in graphene, we replace $V_{\vec{q}}$ with $V_s(\vec{q},\omega) = V_{\vec{q}}/\varepsilon(\vec{q},\omega)$, where the dielectric function $\varepsilon(\vec{q},\omega)$ in the random phase approximation is given by the Lindhard formula

$$\varepsilon(\vec{q},\omega) = 1 - V_{\vec{q}}\Pi^0(\vec{q},\omega), \tag{5.18}$$

and the polarizability $\Pi^0(\vec{q},\omega)$ is written as

$$\Pi^0(\vec{q},\omega) = \sum_{\alpha\beta} \frac{f_\alpha - f_\beta}{\epsilon_\alpha - \epsilon_\beta + \hbar\omega + i\gamma} |F_{\alpha\beta}(\vec{q})|^2, \tag{5.19}$$

with the form factor $F_{\alpha\beta}(\vec{q}) = \langle\alpha|e^{i\vec{q}\cdot\vec{r}}|\beta\rangle$ and $\gamma$ is the line broadening which can be attributed to disorder [46]. We use the same value of the line broadening $\gamma = 10^{13}$ $s^{-1}$ here and in all other places where it is included. The value of $\omega$ is determined by $\hbar\omega = \epsilon_\gamma - \epsilon_\alpha$ in $V_{\alpha\beta\gamma\delta}$ [50]. The occupation factors $f_{\alpha,\beta}$ in Eq. (5.19) are determined self-consistently from the steady-state solutions to the rate equations (5.36) with screening included.

The rate of the Auger scattering from state $|a,b\rangle$ to state $|c,d\rangle$ is calculated from the Fermi's golden rule; it is symmetric with respect to the initial and final states:

$$\Gamma_{ab\leftrightarrow cd} = \frac{2\pi}{\hbar} |\langle cd|V_C|ab\rangle|^2 \, \delta(\epsilon_c + \epsilon_d - \epsilon_a - \epsilon_b), \tag{5.20}$$

where the matrix element is

$$\langle cd|V_C|ab\rangle = \frac{1}{2} \left(V_{cdab} - V_{dcab} + V_{dcba} - V_{cdba}\right) \ . \tag{5.21}$$

So, there are essentially four terms because electrons are indistinguishable particles. The state $|a,b\rangle$ in Eq. (5.21) only means that both $|a\rangle$ and $|b\rangle$ are occupied, instead of specifying that electron 1 is in $|a\rangle$, and electron 2 is in $|b\rangle$. One can find mistakes in the literature with some of the terms missing.

### *5.4.2 Auger Scattering between Landau Levels in Graphene*

For graphene in a transverse magnetic field, an electron state can be written as $|\alpha\rangle$ $= |n_\alpha, k_\alpha, s_\alpha, \xi_\alpha\rangle$, with notations explained in Sec. II. We will address the screening

effect first. The form factor in Eq. (5.19) can be evaluated to be

$$F_{\alpha\beta}(\vec{q}) = \langle\alpha|e^{i\vec{q}\cdot\vec{r}}|\beta\rangle = \delta_{s_\alpha,s_\beta}\delta_{\xi_\alpha,\xi_\beta}\delta_{q_y,k_\alpha-k_\beta}e^{-iq_x l_c^2 k_\beta}G_{n_\alpha n_\beta}(q_y,q_x), \tag{5.22}$$

where we have defined

$$G_{n_\alpha n_\beta}(q_y,q_x) \equiv \int dx \Phi^\dagger_{n_\alpha}(q_y,x)e^{iq_x x}\Phi_{n_\beta}(0,x)\ . \tag{5.23}$$

So the polarizability becomes

$$\Pi^0(\vec{q},\omega) = \frac{2A}{\pi l_c^2}\sum_{n_\alpha n_\beta}\frac{f_{n_\alpha}-f_{n_\beta}}{\epsilon_{n_\alpha}-\epsilon_{n_\beta}+\hbar\omega+i\delta}|G_{n_\alpha n_\beta}(q_y,q_x)|^2\ . \tag{5.24}$$

One can check that $|G_{n_\alpha n_\beta}(q_y,q_x)|$ only depends on the magnitude of $\vec{q}$, so $\Pi^0(\vec{q},\omega)$ and $V_s(\vec{q},\omega)$ are only functions of $q=|\vec{q}|$. We calculated the form factor numerically and checked that it agreed with the analytical expression in [46].

Then, using Eq. (5.17) and Eq. (5.30), the Coulomb matrix element is

$$\begin{aligned}
V_{abcd} &= \delta_{s_a,s_c}\delta_{s_b,s_d}\delta_{\xi_a,\xi_c}\delta_{\xi_b,\xi_d} \\
&\quad\times\sum_{\vec{q}} V_s(\vec{q},\omega)\delta_{q_y,k_a-k_c}e^{-iq_x l_c^2 k_c}G_{n_a n_c}(q_y,q_x)\delta_{-q_y,k_b-k_d}e^{iq_x l_c^2 k_d}G_{n_b n_d}(-q_y,-q_x) \\
&= \delta_{s_a,s_c}\delta_{s_b,s_d}\delta_{\xi_a,\xi_c}\delta_{\xi_b,\xi_d}\delta_{k_a+k_b,k_c+k_d} \\
&\quad\times\sum_{q_x} V_s\left(\vec{q},\omega\right)e^{-iq_x l_c^2(k_c-k_d)}G_{n_a n_c}(q_y,q_x)G_{n_b n_d}(-q_y,-q_x)\Big|_{q_y=k_a-k_c}\ .
\end{aligned} \tag{5.25}$$

For a fixed $k_a$, this matrix element decays quickly when $k_c - k_a$ is large, since $G_{n_a n_c}(q_y,q_x) \propto \exp(-(ql_c)^2/4)$ when $q$ is large [46]. If $k_c$ is bounded, then $k_b$ is bounded too, otherwise the term $e^{-iq_x l_c^2(k_c-k_d)}$ would oscillate too fast with $q_x$, which essentially makes the summation over $q_x$ to vanish.

The Auger scattering rate between two pairs of Landau levels $(n_a, n_b)$ and $(n_c, n_d)$ is

$$\Gamma_{n_a n_b \leftrightarrow n_c n_d} = \frac{1}{2A/\pi l_c^2} \sum_{\xi_a, k_a, s_a} \sum_{\xi_b, k_b, s_b} \sum_{\xi_c, k_c, s_c} \sum_{\xi_d, k_d, s_d} \Gamma_{ab \leftrightarrow cd} \left( \times \frac{1}{2} \text{ if } n_a = n_b \text{ or } n_c = n_d \right), \tag{5.26}$$

where the factor 1/2 in the parenthesis is because of the double counting the initial or final states. In Eq. (5.26), one of the summations can be dropped immediately, since the result from the other three summations will be independent of the forth set of quantum numbers. This summation will give exactly the degeneracy $2A/\pi l_c^2$, so it will cancel with the pre-factor. One summation of $k$ can also be eliminated due to the conservation of momentum $k_a + k_b = k_c + k_d$. As the energy is fully quantized, we will replace the $\delta$ function in Eq. (5.20) with a Lorentzian of line width $\gamma$.

## 5.5 Phonon Scattering

### *5.5.1 General Formulas*

The interaction Hamiltonian between phonons and electrons can generally be written as

$$H_{int}^{ph} = \sum_{\vec{k},\ \vec{q}} F(q) c_{\vec{k}+\vec{q}}^{\dagger} c_{\vec{k}} (b_{\vec{q}} + b_{-\vec{q}}^{\dagger}), \tag{5.27}$$

where $c$ and $c^{\dagger}$ are annihilation and creation operators for electrons, $b$ and $b^{\dagger}$ are annihilation and creation operators for phonons, and $F(q)$ is defined below. Using Fermi's golden rule, the scattering rate from an initial electronic state $|\varphi_i\rangle$ to a final

state $|\varphi_f\rangle$ is

$$\Gamma^{ph}_{i\to f} = \frac{2\pi}{\hbar}\sum_{\vec{q}}(n_q+1)|F(q)|^2|M_{fi}(\vec{q})|^2\delta(\epsilon_f+\epsilon^{ph}_q-\epsilon_i) + \frac{2\pi}{\hbar}\sum_{\vec{q}} n_q|F(q)|^2|M_{fi}(\vec{q})|^2\delta(\epsilon_f-\epsilon^{ph}_q-\epsilon_i), \tag{5.28}$$

where the first term is for the phonon emission, the second term is for the phonon absorption, and the matrix element is given by

$$\begin{aligned} M_{fi}(\vec{q}) &= \langle\varphi_f|\sum_{\vec{k}} c^\dagger_{\vec{k}+\vec{q}}c_{\vec{k}}|\varphi_i\rangle \\ &= \int d\vec{r}\varphi^\dagger_f(\vec{r})e^{i\vec{q}\cdot\vec{r}}\varphi_i(\vec{r}) \end{aligned} \tag{5.29}$$

Using the wave functions in Eq. (5.2), the matrix element $M_{fi}(\vec{q})$ for $|i\rangle = |n_i, k_i, s, \xi\rangle$ and $|f\rangle = |n_f, k_f, s, \xi\rangle$ is calculated to be

$$\delta_{q_y,k_f-k_i}e^{-iq_xl_c^2k_i}G_{n_fn_i}(q_y,q_x)\ . \tag{5.30}$$

The averaged scattering rate from an initial Landau level $n_i$ to a a final Landau level $n_f$ is

$$\begin{aligned} \Gamma^{ph}_{n_i\to n_f} &= \sum_{k_f}\Gamma^{ph}_{i\to f} \\ &= \frac{2\pi}{\hbar}\sum_{\vec{q}}(n_q+1)|F(q)|^2|G_{n_fn_i}(q_y,q_x)|^2\delta(\epsilon_f+\epsilon^{ph}_q-\epsilon_i) \\ &+ \frac{2\pi}{\hbar}\sum_{\vec{q}} n_q|F(q)|^2|G_{n_fn_i}(q_y,q_x)|^2\delta(\epsilon_f-\epsilon^{ph}_q-\epsilon_i)\ . \end{aligned} \tag{5.31}$$

We will only consider the case of low enough temperatures, when phonon absorp-

tion is unimportant and only phonon emission processes contribute to the scattering rate. At room temperature this is still a reasonable approximation; it can be easily dropped if a greater accuracy is needed. We include the screening effect by carriers in graphene in the phonon scattering processes. This can be done by replacing $F(q)$ with $F_s(q,\omega) = F(q)/\varepsilon(q,\omega)$, where the dielectric function $\varepsilon(q,\omega)$ is given in Eq. (5.18) and Eq. (5.24), where again the occupation factors are determined self-consistently from the steady-state solutions to the rate equations (5.36) with screening included.

### *5.5.2 LA Phonon Scattering*

For longitudinal acoustic (LA) phonon scattering, the expression for $F(q)$ is [51]

$$F_{LA}(q) = -\sqrt{\frac{\hbar}{2\rho A v_s}} D\sqrt{q}, \tag{5.32}$$

where $\rho = 7.6 \times 10^{-8}$ g/cm$^2$ is the area mass density of graphene, $v_s = 2 \times 10^6$ cm/s is the sound velocity, and the deformation potential $D$ is in the 10−50 eV range. Also, the energy of a LA phonon is $E_q^{LA} = \hbar v_s q$. Plugging these expressions into Eq. (5.31), we get the scattering rate by LA phonons:

$$\Gamma^{LA}_{n_i \to n_f} = \frac{D^2 q_0^2}{4\pi\rho\hbar v_s^2} \int_0^{2\pi} d\theta |G_{n_f n_i}(q_0 \sin\theta, q_0 \cos\theta)|^2, \tag{5.33}$$

where $q_0 = (\epsilon_{n_i} - \epsilon_{n_f})/\hbar v_s$. The coefficient is of the order of $10^{14}$ s$^{-1}$ for B $\sim$ 1 T. However, the integrand in Eq. (5.33) is roughly of the order of $\exp[-(q_0 l_c)^2/2]$, which is extremely small, since $q_0 l_c \sim \omega_c l_c / v_s = \sqrt{2} v_F / v_s = 50\sqrt{2}$. So, the LA phonon scattering does not contribute significantly to electronic transitions between Landau levels due to a large ratio $v_f/v_s \gg 1$.

### 5.5.3 Surface Optical Phonon Scattering

Since we want to use phonon scattering to our advantage in order to facilitate electron relaxation to the upper laser state, we consider graphene on a polar substrate or sandwiched between two substrates. In this case, the electrons in graphene can couple to the surface or interface modes of optical phonons [44, 52], which we will call the surface optical (SO) phonons for brevity. If the two substrates on both sides of the graphene layer are the same, the SO phonon energy is equal to the longitudinal optical (LO) phonon energy of the substrate [52]. If there is vacuum on one side, the SO phonon energy is slightly shifted from the LO phonon energy [44]. We will assume the former case for definiteness, but note that it would be straightforward to calculate interface optical phonon modes for an arbitrarily complex structure. If we assume that the graphene layer does not affect the SO phonon modes, then the expression of $F(q)$ can be written as

$$F_{SO}(q) = \left[\frac{2\pi e^2 \hbar\omega_{SO}}{A}\left(\frac{1}{\kappa_\infty^{sub}} - \frac{1}{\kappa_0^{sub}}\right)\right] \Big/ \sqrt{2q}\,, \tag{5.34}$$

where $A$ is the area of graphene, $\kappa_0^{sub}$ ($\kappa_\infty^{sub}$) is the low (high) frequency dielectric constant of the substrate, and $\hbar\omega_{SO}$ is the energy of the surface optical phonon. Since it has a flat dispersion, we replace the $\delta$ functions with a Lorentzian $\mathcal{L}_\gamma(E)$ $= \gamma/\pi(E^2 + \gamma^2)$, where $\gamma$ is the broadening of Landau levels, which can be again attributed to disorder. Using again Eq. (5.31), we find the SO phonon scattering rate to be

$$\begin{aligned}\Gamma^{SO}_{n_i\to n_f} = {} & \frac{1}{2}e^2\omega_{SO}\left(\frac{1}{\kappa_\infty^{sub}} - \frac{1}{\kappa_0^{sub}}\right)\mathcal{L}_\gamma(\epsilon_{n_i} - \epsilon_{n_f} - \hbar\omega_{SO}) \\ & \times \int_0^\infty dq \frac{q^2}{(q - \frac{2\pi e^2}{\kappa_0 A}\Pi^0(q,\omega))^2}\int_0^{2\pi} d\theta |G_{n_f n_i}(q\sin\theta, q\cos\theta)|^2,\end{aligned} \tag{5.35}$$

where the screening effect is included, and $\omega = (\epsilon_{n_i} - \epsilon_{n_f})/\hbar$.

## 5.6 Landau Level Populations under Optical Pumping

After the expressions for the optical transition rates and the scattering rates due to SO phonon emission and Auger processes have been found, we can write the density matrix equations with adiabatically eliminated optical polarizations to arrive at the set of rate equations for the filling factors of the Landau levels:

$$\frac{d}{dt}f_{n_a} = \left.\frac{d}{dt}f_{n_a}\right|^{op} + \left.\frac{d}{dt}f_{n_a}\right|^{SO} + \left.\frac{d}{dt}f_{n_a}\right|^{Auger}, \tag{5.36}$$

where

$$\left.\frac{d}{dt}f_{n_a}\right|^{op} = -\sum_{n_b}\Gamma^{op}_{n_a n_b}(f_{n_a} - f_{n_b}), \tag{5.37}$$

$$\left.\frac{d}{dt}f_{n_a}\right|^{SO} = -\sum_{n_b}\Gamma^{SO}_{n_a\to n_b}f_{n_a}(1 - f_{n_b}) + \sum_{n_b}\Gamma^{SO}_{n_b\to n_a}f_{n_b}(1 - f_{n_a}), \tag{5.38}$$

and

$$\left.\frac{d}{dt}f_{n_a}\right|^{Auger} = \sum_{n_b} t_{n_a,n_b} \times \sum_{n_c}\sum_{n_d\geq n_c}\Gamma_{n_a n_b\leftrightarrow n_c n_d}\left(-f_{n_a}f_{n_b}(1 - f_{n_c})(1 - f_{n_d}) + f_{n_c}f_{n_d}(1 - f_{n_a})(1 - f_{n_b})\right), \tag{5.39}$$

where $t_{n_a,n_b} = 2$ if $n_b = n_a$, and 1 otherwise. Here the subscript "op" denotes the optical transition rates.

Using these rate equations, we can simulate the dynamics of the graphene system for an arbitrary optical excitation. Note that the system is highly nonlinear, firstly because of the state filling and secondly, because the matrix elements depend on the

dynamic screening, which depends in turn on the instantaneous distribution of electrons in Landau levels. Therefore, time dependent simulations are time consuming. Here we present the steady state results for the continuous-wave optical pumping.

## 5.7 Results and Discussion

For a GaAs substrate, the SO phonon energy is 36 meV, which requires the magnetic field to be around 1 T. In the simulations, broadenings of all transitions are set to be 5 meV, and $T_2$ is 0.1 ps. Also, we consider intrinsic (undoped) graphene as an example, so without pumping the $n = 0$ LL is half-filled, all LLs below are fully filled, and all LLs above are empty. We define the gain between $n = -1$ and $-2$ as the left-hand side of Eq. (5.13): $g_{-1,-2} = -(2\pi\omega/\sqrt{\kappa}c)\mathrm{Im}[\chi(\omega_{-1,-2})]$. To minimize the absorption of the THz field by the polar substrate, we would like to reduce its thickness to a few $\mu$m to be much smaller than the wavelength of the THz field but at the same time, thick enough to be considered bulk for SO phonon scattering. The gain is maximized when there is air outside the active layer so that $\kappa = 1$.

The dependence of the steady state filling factors and gain per graphene monolayer on the pump intensity are shown in Fig. 5.4 and Fig. 5.5.

As can be seen from the figures, one can achieve a significant steady-state population inversion between states $n = -1$ and $-2$ and the gain value of about 0.05 per monolayer of graphene. For comparison, the right-hand side of Eq. (5.13) which describes mirror losses is equal to 0.025 when the reflectivities $r_1 = r_2 = 0.95$, which is easily achievable. The closest allowed transition at the $\hat{l}_{\ominus}$ polarization is from $n = -3$ to $n = -2$ LLs. It is detuned from the laser transition frequency by about 4 meV in a magnetic field of 1 T. Therefore its contribution to losses is lower than the gain. Since the electron motion is quantized, there are no other losses in graphene associated with free carriers. The undoped GaAs is a popular material for the nonlinear

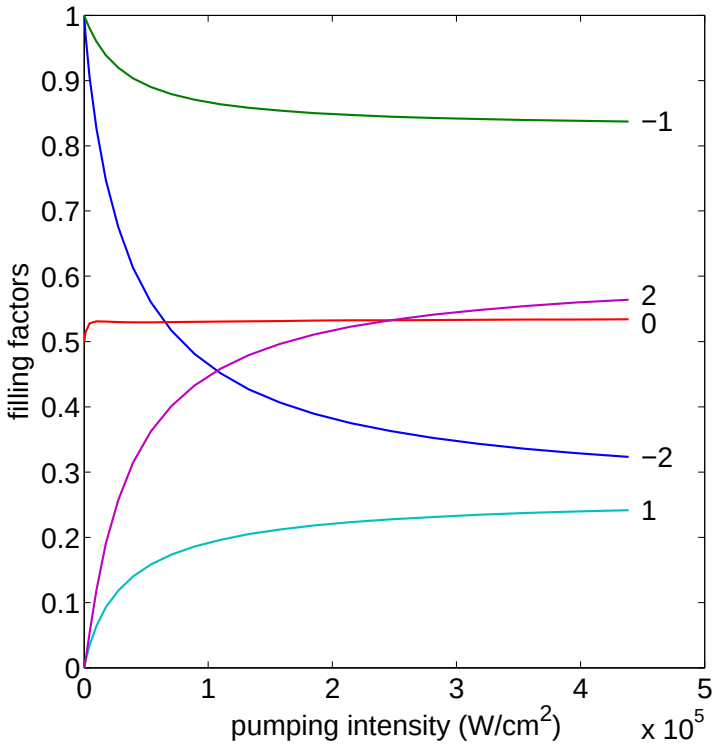


Figure 5.4: Dependence of the steady state filling factors on the pumping intensity. Landau level numbers are shown to the right of the curves.

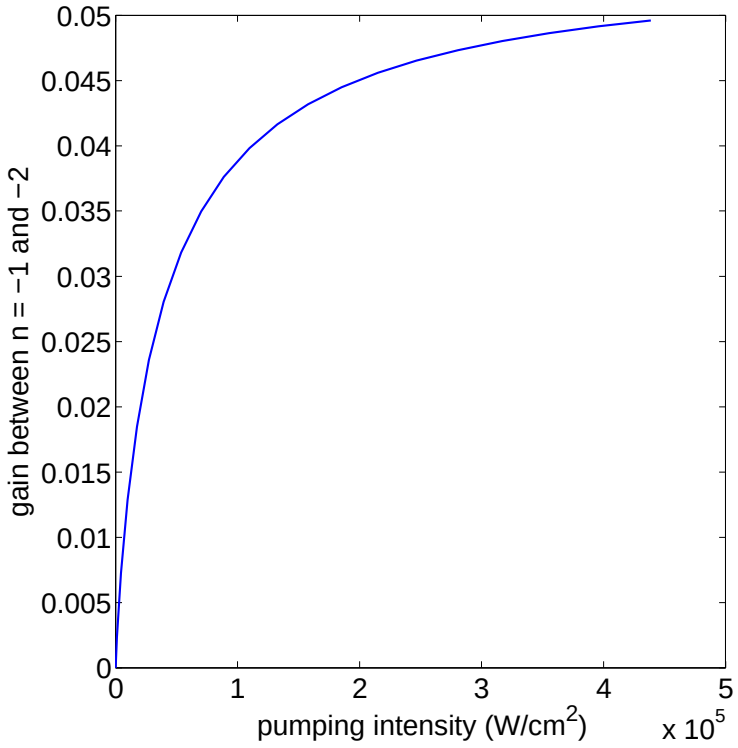


Figure 5.5: Dependence of the gain between n = −1 and −2 LLs per graphene monolayer on the pumping intensity.

THz generation and its THz losses are rather low, especially since the polar substrate can be thinned down to a few $\mu$m. Therefore, one can operate in the desirable regime where the losses are dominated by mirror losses. Note that the gain of 0.05 is higher than the maximum value of $\pi\alpha \simeq 0.023$ in graphene without a magnetic field. This is because energy quantization in a magnetic field condenses the continuous density of states into discrete LLs, leading to the maximum gain enhancement scaling as the ratio of the transition frequency to linewidth. One can further scale the gain up by stacking several graphene-on-GaAs layers.

For surface states in 3D topological insulators such as $Bi_2Se_3$ or $Bi_2Te_3$, the Fermi velocity has a similar value but there is no spin or valley degeneracy. Therefore, a similar laser scheme with a thin film of $Bi_2Se_3$ (i.e. two surfaces) placed on a polar substrate will give about two times smaller gain. Additional free-carrier THz losses may exist in this case due to unintentional doping of the bulk $Bi_2Se_3$.

One can also see in Fig. 5.4 that the population inversion exists also between states $n = 2$ and 1, albeit at a two times lower level. This seems unexpected, given that the optical pumping brings carriers only to state 1. However, a closer look at the rate equations shows that the population inversion between levels 1 and 2 is a consequence of a strongly non-equilibrium carrier distribution below the Fermi level created by the optical pumping, namely the population inversion between states $-2$ and $-1$. Indeed, when $f_{-1} > f_{-2}$, the Auger scattering rate from states $(1, -1)$ to states $(2, -2)$ is greater than the scattering rate in the opposite direction. This creates the population inversion $f_2 > f_1$ and the gain for the $\hat{l}_{\oplus}$ polarization, which is about two times smaller than the $\hat{l}_{\ominus}$ gain.

In conclusion, we show the feasibility of the Landau level THz laser in a magnetized graphene. Despite ultrafast Auger relaxation, steady-state operation of the laser under continuous wave optical pumping is possible by utilizing surface or in-

terface phonon relaxation. The scheme is scalable to thin films of 3D topological insulators such as $Bi_2Se_3$ or $Bi_2Te_3$.

# 6. SECOND-HARMONIC GENERATION FROM SINGLE-LAYER GRAPHENE

## 6.1 Introduction

This work is inspired by the experimental observations. The experiment of second-harmonic generation (SHG) in graphene was conducted in Dr. Heinz's group in Columbia University. The second-order nonlinear susceptibility is measured, and the dependence on configurations of polarizations of the fundamental and SHG light is obtained. The dependence cannot be understood intuitively, so we conduct a calculation based on quantum mechanical model, and the results agree with the observation. We first show the experimental results, and then the calculation.

## 6.2 Experimental Measurements

The basic setup of the experiment is shown in Fig. 6.1. Two layers of graphene are fabricated in a graphene/hBN/graphene sandwich device on fused silica substrate. The fundamental light with wavelength 800 nm is incident obliquely on the graphene layer, and the generated second-harmonic (SH) light is collected in a reflection geometry. Figure 6.2 shows the SH signal measured for four different polarization configurations. The electric field is parallel and perpendicular to the plane of incidence for the P- and S-polarizations, respectively. Interestingly, the measurement shows a clear SH signal for the S-in P-out polarization configuration. The SH signal is diminishingly small for all three other polarization configurations. In order to explain the polarization dependence, we conduct a theoretical calculation for the SHG in graphene.

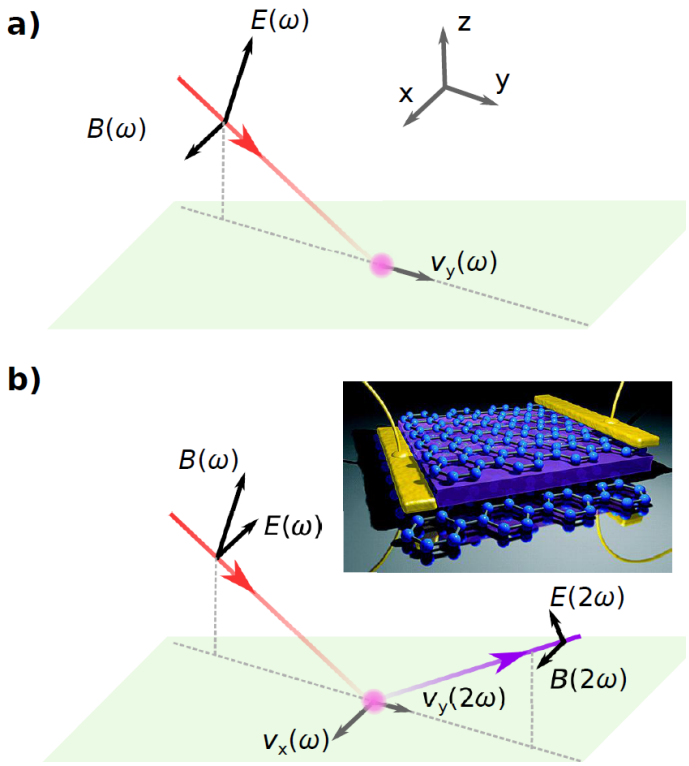


Figure 6.1: Illustration of the experimental configuration for the measurement of second-order nonlinear response from graphene with (a) P-polarized excitation and (b) S-polarized excitation. The inset in (b) shows our device structure for the doping dependence measurement.

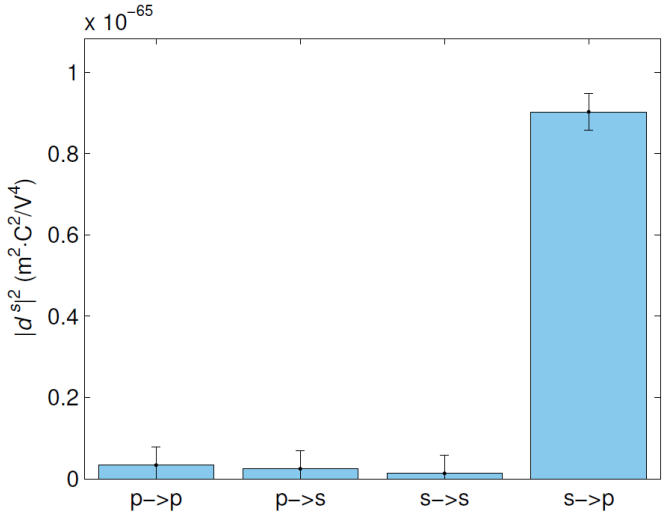


Figure 6.2: Second-order nonlinear susceptibility of graphene measured for different polarization configurations. The first letter in the polarization configuration denotes the incidence polarization and the second letter denotes the collection polarization..

## 6.3 Basics about Optical Transition in Graphene

The Hamiltonian of graphene near the Dirac point $\vec{K}$ is

$$H = v_F \vec{\sigma} \cdot \hat{\vec{p}} = v_F \begin{pmatrix} 0 & \hat{p}_x - i\hat{p}_y \\ \hat{p}_x + i\hat{p}_y & 0 \end{pmatrix}, \tag{6.1}$$

where $\hat{p}$ is the momentum operator relative to $\vec{K}$. The eigenenergies are $E_{\pm}(\vec{k}) = \pm\hbar v_F k$, and eigen-wavefunctions are

$$\langle \vec{\rho} | s, \vec{k} \rangle = \frac{1}{\sqrt{2A}} \exp(i\vec{k} \cdot \vec{\rho}) \begin{pmatrix} s \\ e^{i\theta(\vec{k})} \end{pmatrix}, \tag{6.2}$$

where $s = 1$ for conduction band, $s = -1$ for valence band, $A$ is the area of graphene, and $\theta(\vec{k})$ is the angle of wave vector $\vec{k}$ with respect to the $x$-axis.

The interaction Hamiltonian between graphene and the optical field which has an in-plane component of the electric field can be written directly as

$$\hat{H}_{int}^{op} = v_F \frac{e}{c} \vec{\sigma} \cdot \vec{A} = \frac{e}{c} \hat{\vec{v}} \cdot \vec{A}, \tag{6.3}$$

where $\hat{\vec{v}} = v_F \vec{\sigma}$ is the velocity operator, and $\vec{A}$ is the vector potential of the optical field, which is related to electric field by $\vec{E}^{op} = (-1/c)\partial \vec{A}/\partial t$. Using this Hamiltonian, the equation for off-diagonal density matrix element is written as

$$\begin{aligned} i\hbar \frac{\partial}{\partial t} \rho_{mn} = (\epsilon_m - \epsilon_n)\rho_{mn} + \frac{e}{c}(\hat{\vec{v}} \cdot \vec{A})_{mn}(\rho_{nn} - \rho_{mm}) \\ + \frac{e}{c} \sum_{l \neq m,n} \left( (\hat{\vec{v}} \cdot \vec{A})_{ml} \rho_{ln} - \rho_{ml} (\vec{v} \cdot \vec{A})_{ln} \right), \end{aligned} \tag{6.4}$$

where both linear and nonlinear effects are included. We are going to calculate the current in response of the optical field. The current operator is given by $\hat{\vec{j}} = -e v_F \vec{\sigma}$.

A monochromatic optical field with an in-plane component of the electric field along $\hat{\eta}$ can be expressed by the vector potential $\vec{A} = 1/2(\hat{\eta} A_\omega e^{i(\vec{q}\cdot\vec{\rho} - \omega t)} + \text{c.c.})$. When the light is obliquely incident on the graphene surface with an incidence angle $\alpha$, we have $q = (\omega/c)\sin\alpha$. Also, $e^{-i\omega t}$ corresponds to photon annihilation, and $e^{i\omega t}$ corresponds to photon creation. With this expression, we can write down the matrix elements of the interaction between optical field and graphene as below

$$\left( (\hat{\vec{v}} \cdot \hat{\eta}) e^{i\vec{q}\cdot\vec{\rho}} \right)_{mn} = \frac{1}{2} v_F \left[ (\eta_x - i\eta_y) s_m e^{i\theta_n} + (\eta_x + i\eta_y) s_n e^{-i\theta_m} \right] \delta_{\vec{k}_m, \vec{k}_n + \vec{q}}, \tag{6.5}$$

$$\left( (\hat{\vec{v}} \cdot \hat{\eta}^*) e^{-i\vec{q}\cdot\vec{\rho}} \right)_{mn} = \frac{1}{2} v_F \left[ (\eta_x^* - i\eta_y^*) s_m e^{i\theta_n} + (\eta_x^* + i\eta_y^*) s_n e^{-i\theta_m} \right] \delta_{\vec{k}_m, \vec{k}_n - \vec{q}}. \tag{6.6}$$

Notice that there will be no plane wave factor in the density matrix, since the spatial variation in the optical field has been absorbed into the matrix elements of

interaction Hamiltonian. This approach includes higher-order terms beyond dipole approximation.

## 6.4 Linear Response

For the linear response, we have

$$\rho^{\omega}_{mn} = \frac{e/(2c)\left((\hat{\vec{v}}\cdot\hat{\eta})e^{i\vec{q}\cdot\vec{\rho}}\right)_{mn}(\rho_{nn}-\rho_{mm})A_{\omega}e^{-i\omega t}}{\hbar\omega-(\epsilon_m-\epsilon_n)} + \frac{e/(2c)\left((\hat{\vec{v}}\cdot\hat{\eta}^*)e^{-i\vec{q}\cdot\vec{\rho}}\right)_{mn}(\rho_{nn}-\rho_{mm})A^*_{\omega}e^{i\omega t}}{-\hbar\omega-(\epsilon_m-\epsilon_n)}. \tag{6.7}$$

We will only need the $e^{-i\omega t}$ term, since it contains all the information. According to Falkovsky's paper [53], the response of density matrix to the optical field should be zero when $\omega = 0$, and this condition is applied with $\vec{q} \neq 0$ fixed. So, we subtract the $\omega = 0$ term from the above expression, namely

$$\begin{aligned}\frac{1}{\hbar\omega-(\epsilon_m-\epsilon_n)} &\to \frac{1}{\hbar\omega-(\epsilon_m-\epsilon_n)} - \frac{1}{-(\epsilon_m-\epsilon_n)} \\ &= \frac{\hbar\omega}{[\hbar\omega-(\epsilon_m-\epsilon_n)]\,[(\epsilon_m-\epsilon_n)]}.\end{aligned} \tag{6.8}$$

So, $\rho_{mn}$ becomes

$$\rho^{\omega}_{mn} = \frac{e/(2c)\left((\hat{\vec{v}}\cdot\hat{\eta})e^{i\vec{q}\cdot\vec{\rho}}\right)_{mn}(\rho_{nn}-\rho_{mm})\hbar\omega A_{\omega}e^{-i\omega t}}{[\hbar\omega-(\epsilon_m-\epsilon_n)]\,[(\epsilon_m-\epsilon_n)]}. \tag{6.9}$$

Let

$$\hat{\vec{j}}^{\omega} = \frac{1}{2}\hat{\vec{J}}^{\omega}e^{i(\vec{q}\cdot\vec{\rho}-\omega t)} + \text{c.c.}, \tag{6.10}$$

then $\vec{J}^{\omega} = -2e\mathrm{Tr}[\hat{\rho}\hat{\vec{v}}e^{-i(\vec{q}\cdot\vec{\rho}-\omega t)}] = -2e\sum_{mn}\rho_{mn}(\hat{\vec{v}}e^{-i\vec{q}\cdot\vec{\rho}})_{nm}e^{i\omega t}$. Since $\hat{\vec{J}}^{\omega}$ varies with time slowly, only the $e^{-i\omega t}$ term in the density matrix is relevant. We also replace $\omega \to \omega + i\gamma$ to include dissipation. Then, we get

$$\vec{J}^{\omega} = -\frac{e^2}{c}\sum_{mn}\frac{(\hat{\vec{v}}e^{-i\vec{q}\cdot\vec{\rho}})_{nm}\left((\hat{\vec{v}}\cdot\hat{\eta})e^{i\vec{q}\cdot\vec{\rho}}\right)_{mn}(\rho_{nn}-\rho_{mm})\hbar\omega A_{\omega}}{[\hbar\omega-(\epsilon_m-\epsilon_n)+i\hbar\gamma]\,[(\epsilon_m-\epsilon_n)]}, \tag{6.11}$$

and it is evaluated to be

$$\begin{aligned}
\vec{J}^{\omega} &= -g\frac{e^2v_F^2\hbar\omega A_{\omega}}{4c\hbar^2}\frac{1}{(2\pi)^2} \\
&\times\sum_{s_m,s_n}\int d^2\vec{k}\frac{f(s_n,|\vec{k}|)-f(s_m,|\vec{k}+\vec{q}|)}{\left(\omega-v_F(s_m|\vec{k}+\vec{q}|-s_n|\vec{k}|)+i\gamma\right)\left(v_F(s_m|\vec{k}+\vec{q}|-s_n|\vec{k}|)\right)} \\
&\left[(\eta_x-i\eta_y)s_me^{i\theta(\vec{k})}+(\eta_x+i\eta_y)s_ne^{-i\theta(\vec{k}+\vec{q})}\right]\left[(\hat{x}+i\hat{y})s_me^{-i\theta(\vec{k})}+(\hat{x}-i\hat{y})s_ne^{i\theta(\vec{k}+\vec{q})}\right],
\end{aligned} \tag{6.12}$$

where $g = 4$ is the spin-valley degeneracy. We will discuss the case $T \to 0$ in this work. For interband transitions, the contribution of $\vec{J}^{\omega}$ is from $k > k_F$. And for intraband transition, the contribution is from $k \sim k_F$. Assuming the Fermi level is far from the Dirac points, where $\epsilon = 0$, or $k_F \gg q$ quantitatively, then we can make the expansions like below

$$\begin{aligned}
|\vec{k}+\vec{q}| &\simeq k + q\cos\theta + \frac{1}{2}\frac{\sin^2\theta}{k}q^2, \\
f(|\vec{k}+\vec{q}|) &\simeq f(k) + \frac{\partial f}{\partial k_x}q + \frac{1}{2}\frac{\partial^2 f}{\partial k_x^2}q^2 + \frac{1}{6}\frac{\partial^3 f}{\partial k_x^3}q^3, \\
\theta(\vec{k}+\vec{q}) &\simeq \theta(\vec{k}) - \frac{q}{k}\sin\theta(\vec{k}), \\
e^{i\theta(\vec{k}+\vec{q})} &\simeq e^{i\theta}\left(1 - i\frac{q}{k}\sin\theta\right),
\end{aligned} \tag{6.13}$$

where we have $\vec{q} = (q, 0)$, and $\theta \equiv \theta(\vec{k})$. The partial derivatives of $f$ are given below in polar coordinates:

$$\begin{aligned}
\frac{\partial f}{\partial k_x} &= \cos\theta \frac{\partial f}{\partial k}, \\
\frac{\partial^2 f}{\partial k_x^2} &= \cos^2\theta \frac{\partial^2 f}{\partial k^2} + \frac{\sin^2\theta}{k}\frac{\partial f}{\partial k}, \\
\frac{\partial^3 f}{\partial k_x^3} &= \cos^3\theta \frac{\partial^3 f}{\partial k^3} + \frac{3\cos\theta\sin^2\theta}{k}\frac{\partial^2 f}{\partial k^2} - \frac{3\cos\theta\sin^2\theta}{k^2}\frac{\partial f}{\partial k}.
\end{aligned} \tag{6.14}$$

### *6.4.1 Interband Transitions*

For interband contribution, the dominant term is for $s_m = 1$ and $s_n = -1$, since these transitions are in resonant with the optical field. We can evaluate $\vec{J}^{\omega}$ to the zeroth order of q,

$$\vec{J}^{\omega} = -g\frac{e^2 v_F^2 \hbar\omega A_\omega}{4c\hbar^2}\frac{1}{(2\pi)^2}4\pi(\eta_x\hat{x} + \eta_y\hat{y})\int_{k_F}^{\infty} kdk\frac{1}{(\omega - 2v_F k + i\gamma)2v_F k}. \tag{6.15}$$

Using $E^{\omega} = (i\omega/c)A^{\omega}$, we get the optical conductivity to be

$$\sigma^{(1)}(\omega) = \frac{e^2 v_F}{2\pi\hbar}\int_{k_F}^{\infty} dk\frac{i}{\omega - 2v_F k + i\gamma}. \tag{6.16}$$

The imaginary part of the integration diverges at large $k$, but one has to consider the actual electron dispersion in graphene far from the Dirac point. The real part of optical conductivity is calculated to be

$$\sigma_r^{(1)}(\omega) = \frac{e^2 v_F}{2\pi\hbar}\int_{k_F}^{\infty} dk\pi\delta(\omega - 2v_F k) = \frac{e^2}{4\hbar}\theta(\omega - 2v_F k_F), \tag{6.17}$$

where $\theta(x)$ is the Heaviside function. This result is the well know constant absorbance of graphene.

### 6.4.2 Intraband Transitions

For intraband transitions, $s_m = s_n$. Expansion of numerator and denominator in Eq. (6.12) starts from terms linear in $q$:

$$\begin{aligned}\frac{f(s_n,|\vec{k}|)-f(s_n,|\vec{k}+\vec{q}|)}{\left(|\vec{k}+\vec{q}|-|\vec{k}|\right)} &\simeq -\frac{q\cos\theta\frac{\partial f}{\partial k}+\frac{1}{2}q^2\left(\cos^2\theta\frac{\partial^2 f}{\partial k^2}+\frac{\sin^2\theta}{k}\frac{\partial f}{\partial k}\right)}{q\cos\theta+\frac{1}{2}\frac{\sin^2\theta}{k}q^2} \\ &= -\frac{\partial f}{\partial k}-\frac{1}{2}\frac{q\cos^2\theta}{\cos\theta+\frac{q}{2k}\sin^2\theta}\frac{\partial^2 f}{\partial k^2}, \end{aligned} \tag{6.18}$$

where $f = f(s_n, k)$. The second term is of the order of $\sim q^2$ when $\cos\theta \sim q/k$, so we can drop it. Finally, the intraband contribution to $\vec{J}^{\omega}$ to the zeroth order of $q$ is

$$\begin{aligned}\vec{J}^{\omega} = -g\frac{e^2 v_F^2 \hbar\omega A_\omega}{4c\hbar^2}\frac{1}{(2\pi)^2}\sum_{s_n}\int d^2\vec{k}\frac{-1}{(\omega+i\gamma)\,v_F s_n}\frac{\partial f(s_n,k)}{\partial k} \\ \left[(\eta_x - i\eta_y)s_m e^{i\theta(\vec{k})}+(\eta_x+i\eta_y)s_n e^{-i\theta(\vec{k})}\right]\left[(\hat{x}+i\hat{y})s_m e^{-i\theta(\vec{k})}+(\hat{x}-i\hat{y})s_n e^{i\theta(\vec{k})}\right].\end{aligned} \tag{6.19}$$

The above equation can be integrated analytically,

$$\vec{J}^{\omega} = -g\frac{e^2 v_F^2 \hbar\omega A_\omega}{4c\hbar^2}\frac{1}{(2\pi)^2}\frac{k_F}{(\omega+i\gamma)\,v_F s(\epsilon_F)}4\pi(\eta_x\hat{x}+\eta_y\hat{y}), \tag{6.20}$$

where $s(\epsilon_F)$ means the band index at the energy of Fermi level $\epsilon_F$. Using $E^{\omega} = (i\omega/c)A^{\omega}$, we get the optical conductivity to be

$$\sigma^{(1)}(\omega) = \frac{e^2 v_F k_F s(\epsilon_F)}{\pi\hbar}\frac{i}{\omega+i\gamma}. \tag{6.21}$$

This result agrees with the Drude formula.

## 6.5 Second Harmonic Generation

The second-harmonic response of the off-diagonal density matrix elements is calculated to be

$$\rho_{mn}^{2\omega} = \left(\frac{e}{2c}\right)^2 \frac{A_\omega^2 e^{-2i\omega t}}{2\hbar\omega - (\epsilon_m - \epsilon_n) + i\hbar\gamma} \sum_{l\neq m,n} \left((\hat{\vec{v}}\cdot\hat{\eta})e^{i\vec{q}\cdot\vec{\rho}}\right)_{ml} \left((\hat{\vec{v}}\cdot\hat{\eta})e^{i\vec{q}\cdot\vec{\rho}}\right)_{ln}$$
$$\times \left[\frac{(\rho_{nn}-\rho_{ll})\hbar\omega}{[\hbar\omega - (\epsilon_l - \epsilon_n) + i\hbar\gamma]\,[(\epsilon_l - \epsilon_n)]} - \frac{(\rho_{ll}-\rho_{mm})\hbar\omega}{[\hbar\omega - (\epsilon_m - \epsilon_l) + i\hbar\gamma]\,[((\epsilon_m - \epsilon_l)]}\right]. \quad (6.22)$$

$\rho_{mn}^{2\omega}$ is automatically zero when $\omega = 0$, since the proper form of the linear response density matrix has been used.

Let

$$\hat{\vec{j}}^{2\omega} = \frac{1}{2}\hat{\vec{J}}^{2\omega} e^{i(2\vec{q}\cdot\vec{\rho}-2\omega t)} + \text{c.c.}, \quad (6.23)$$

then $\vec{J}^{2\omega} = -2e\mathrm{Tr}[\hat{\rho}\hat{\vec{v}}e^{-i(2\vec{q}\cdot\vec{\rho}-2\omega t)}] = -2e\sum_{mn}\rho_{mn}(\hat{\vec{v}}e^{-2i\vec{q}\cdot\vec{\rho}})_{nm}e^{2i\omega t}$. Since $\hat{\vec{J}}^{2\omega}$ varies with time slowly, only the $e^{-2i\omega t}$ term in the density matrix is relevant. The result is

$$\vec{J}^{2\omega} = -\frac{e^3}{2c^2}A_\omega^2 \sum_{mnl} \frac{\left(\hat{\vec{v}}e^{-2i\vec{q}\cdot\vec{\rho}}\right)_{nm}\left((\hat{\vec{v}}\cdot\hat{\eta})e^{i\vec{q}\cdot\vec{\rho}}\right)_{ml}\left((\hat{\vec{v}}\cdot\hat{\eta})e^{i\vec{q}\cdot\vec{\rho}}\right)_{ln}}{2\hbar\omega - (\epsilon_m - \epsilon_n) + i\hbar\gamma}$$
$$\times \left[\frac{(\rho_{nn}-\rho_{ll})\hbar\omega}{[\hbar\omega - (\epsilon_l - \epsilon_n) + i\hbar\gamma]\,[(\epsilon_l - \epsilon_n)]} - \frac{(\rho_{ll}-\rho_{mm})\hbar\omega}{[\hbar\omega - (\epsilon_m - \epsilon_l) + i\hbar\gamma]\,[((\epsilon_m - \epsilon_l)]}\right]. \quad (6.24)$$

It is evaluated to be

$$\vec{J}^{2\omega} = -g\frac{e^3}{2c^2\hbar^3}A_\omega^2\hbar\omega\frac{1}{(2\pi)^2}\frac{v_F^3}{2^3}\sum_{s_m,s_n,s_l}\int d^2\vec{k}\frac{1}{2\omega - v_F(s_m|\vec{k}+2\vec{q}| - s_n|\vec{k}|)+i\gamma}$$
$$\times\left[\frac{f(s_n,|\vec{k}|)-f(s_l,|\vec{k}+\vec{q}|)}{\left(\omega - v_F(s_l|\vec{k}+\vec{q}| - s_n|\vec{k}|)+i\gamma\right)\left(v_F(s_l|\vec{k}+\vec{q}| - s_n|\vec{k}|)\right)}\right.$$
$$\left. - \frac{f(s_l,|\vec{k}+\vec{q}|)-f(s_m,|\vec{k}+2\vec{q}|)}{\left(\omega - v_F(s_m|\vec{k}+2\vec{q}| - s_l|\vec{k}+\vec{q}|)+i\gamma\right)\left(v_F(s_m|\vec{k}+2\vec{q}| - s_l|\vec{k}+\vec{q}|)\right)}\right]$$
$$\times\left[(\eta_x - i\eta_y)s_m e^{i\theta(\vec{k}+\vec{q})} + (\eta_x + i\eta_y)s_l e^{-i\theta(\vec{k}+2\vec{q})}\right]\left[(\eta_x - i\eta_y)s_l e^{i\theta(\vec{k})} + (\eta_x + i\eta_y)s_n e^{-i\theta(\vec{k}+\vec{q})}\right]$$
$$\times\left[(\hat{x}+i\hat{y})s_m e^{-i\theta(\vec{k})} + (\hat{x}-i\hat{y})s_n e^{i\theta(\vec{k}+2\vec{q})}\right]. \qquad (6.25)$$

Due to the integration over $\theta$, it is apparent that $\vec{J}^{2\omega}$ vanishes in the zeroth order of $q$. There are two kinds of SHG processes, one of which only contains intraband transitions, and the other contain both intraband and interband transitions. For the latter, there are three types. All the SHG processes are illustrated in Fig. 6.3.

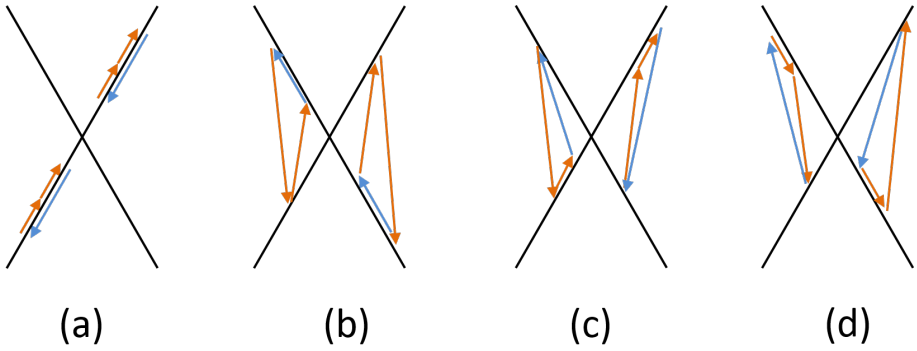


Figure 6.3: The various SHG processes. In each figure, the two orange arrows indicate the fundamental transitions, and the blue arrow indicates the second-harmonic transition. (a), Intraband processes. (b,c,d), Three types of processes which contain both intraband and interband transitions.

### 6.5.1 Intraband Contribution

Intraband means $s_m = s_l = s_n$, so we will just sum over $s_n$. First, we will try to calculate $\vec{J}^{2\omega}$ to the first order in $q$, so we need to expand each factor in the integrand to order $q$. Let's assume $\omega \gg v_F q \gg \gamma$, which seems reasonable for high frequencies, non-plasmonic modes, and low temperatures. In this case, we can drop the term $i\gamma$. For the terms in "[...]" in Eq. 6.25, we expand them in powers of $q$:

$$\frac{1}{s_n v_F}\left[-\frac{1}{\omega - s_n v_F\left(q\cos\theta + \frac{1}{2k}q^2\sin^2\theta\right)}\frac{\frac{\partial f}{\partial k_x} + \frac{1}{2}\frac{\partial^2 f}{\partial k_x^2}q + \frac{1}{6}\frac{\partial^3 f}{\partial k_x^3}q^2}{\cos\theta + \frac{1}{2}\frac{\sin^2\theta}{k}q}\right.$$
$$\left. + \frac{1}{\omega - s_n v_F\left(q\cos\theta + \frac{3}{2k}q^2\sin^2\theta\right)}\frac{\frac{\partial f}{\partial k_x} + \frac{3}{2}\frac{\partial^2 f}{\partial k_x^2}q + \frac{7}{6}\frac{\partial^3 f}{\partial k_x^3}q^2}{\cos\theta + \frac{3}{2}\frac{\sin^2\theta}{k}q}\right]. \tag{6.26}$$

Notice we expand all the terms up to $q^2$, because the denominators can be of order $q$ if $\cos\theta = 0$. If we further expand the denominators that contain $\omega$, then the above expression becomes

$$\frac{1}{s_n v_F \omega}\left[-\left(1 + \frac{s_n v_F}{\omega}q\cos\theta + \frac{v_F}{\omega}\left(\frac{s_n}{2k}\sin^2\theta + \frac{v_F}{\omega}\cos^2\theta\right)q^2\right)\frac{\frac{\partial f}{\partial k_x} + \frac{1}{2}\frac{\partial^2 f}{\partial k_x^2}q + \frac{1}{6}\frac{\partial^3 f}{\partial k_x^3}q^2}{\cos\theta + \frac{1}{2}\frac{\sin^2\theta}{k}q}\right.$$
$$\left. + \left(1 + \frac{s_n v_F}{\omega}q\cos\theta + \frac{v_F}{\omega}\left(\frac{3s_n}{2k}\sin^2\theta + \frac{v_F}{\omega}\cos^2\theta\right)q^2\right)\frac{\frac{\partial f}{\partial k_x} + \frac{3}{2}\frac{\partial^2 f}{\partial k_x^2}q + \frac{7}{6}\frac{\partial^3 f}{\partial k_x^3}q^2}{\cos\theta + \frac{3}{2}\frac{\sin^2\theta}{k}q}\right]. \tag{6.27}$$

Using the same argument as we did in the linear and intraband case, we get the result of the above expression to be simply

$$\frac{1}{s_n v_F \omega}\frac{\partial^2 f}{\partial k^2}q\cos\theta. \tag{6.28}$$

As it is already of order $q$, we just need to keep the zeroth order of $q$ in other factors, as long as the result of integration is nonzero. So, to the first order in $q$, $\vec{J}^{2\omega}$ is evaluated to be

$$\begin{aligned}
\vec{J}^{2\omega} &= -gq\frac{e^3}{2c^2\hbar^3}A_\omega^2\hbar\omega\frac{1}{(2\pi)^2}\frac{v_F^3}{2^3}\frac{1}{2\omega}\frac{1}{s_n v_F\omega}\sum_{s_n}\int_0^\infty kdk\frac{\partial^2 f}{\partial k^2}\int_0^{2\pi}d\theta\cos\theta \\
&\times s_n^3\left[(\eta_x-i\eta_y)e^{i\theta}+(\eta_x+i\eta_y)e^{-i\theta}\right]\left[(\eta_x-i\eta_y)e^{i\theta}+(\eta_x+i\eta_y)e^{-i\theta}\right] \\
&\times\left[(\hat{x}+i\hat{y})e^{-i\theta}+(\hat{x}-i\hat{y})e^{i\theta}\right] \\
&= -A_\omega^2\frac{e^3v_F^2q}{32\pi^2\hbar^2c^2\omega}s(\epsilon_F)f(0) \\
&\times\int_0^{2\pi}d\theta\cos\theta\left[(\hat{x}+i\hat{y})e^{-i\theta}+(\hat{x}-i\hat{y})e^{i\theta}\right] \\
&\times\left[(\eta_x-i\eta_y)e^{i\theta}+(\eta_x+i\eta_y)e^{-i\theta}\right]\left[(\eta_x-i\eta_y)e^{i\theta}+(\eta_x+i\eta_y)e^{-i\theta}\right]. \qquad (6.29)
\end{aligned}$$

And the SHG optical conductivity is

$$\begin{aligned}
\sigma^{(2)}(2\omega) &= \frac{e^3v_F^2q}{32\pi^2\hbar^2\omega^3}s(\epsilon_F) \\
&\times\int_0^{2\pi}d\theta\cos\theta\left[(\hat{x}+i\hat{y})e^{-i\theta}+(\hat{x}-i\hat{y})e^{i\theta}\right] \\
&\times\left[(\eta_x-i\eta_y)e^{i\theta}+(\eta_x+i\eta_y)e^{-i\theta}\right]\left[(\eta_x-i\eta_y)e^{i\theta}+(\eta_x+i\eta_y)e^{-i\theta}\right] \\
&= \frac{e^3v_F^2q}{16\pi\hbar^2\omega^3}s(\epsilon_F)\left[(3\eta_x^2+\eta_y^2)\hat{x}+2\eta_x\eta_y\hat{y}\right] \qquad (6.30)
\end{aligned}$$

So, without considering the effect of projection of the electric field onto the graphene plane, the intraband optical conductivity of $P\to P$ is three times larger than the $S\to P$ one. Using classical kinetic equations, our collaborator Dr. Tokman obtained the same results.

### 6.5.2 Interband Contribution

Interband contribution includes three types of combination of $s_m, s_n, s_l$. They are

Type 1: $s_m = s_n = -s_l$;

Type 2: $s_m = s_l = -s_n$;

Type 3: $s_n = s_l = -s_m$.

We will analyze them one by one. Again, we assume $k_F \gg q$.

**Type 1**: $s_m = s_n = -s_l$, so $\vec{J}^{2\omega}$ is given by

$$\begin{aligned}
\vec{J}^{2\omega} &= -g\frac{e^3}{2c^2\hbar^3}A_\omega^2\hbar\omega\frac{1}{(2\pi)^2}\frac{v_F^3}{2^3}\sum_{s_n}\int d^2\vec{k}\frac{1}{2\omega - s_n v_F(|\vec{k}+2\vec{q}|-|\vec{k}|)+i\gamma} \\
&\times \left[\frac{f(s_n,|\vec{k}|)-f(-s_n,|\vec{k}+\vec{q}|)}{\Big(\omega+s_n v_F(|\vec{k}+\vec{q}|+|\vec{k}|)+i\gamma\Big)\Big(-s_n v_F(|\vec{k}+\vec{q}|+|\vec{k}|)\Big)}\right. \\
&\left. - \frac{f(-s_n,|\vec{k}+\vec{q}|)-f(s_n,|\vec{k}+2\vec{q}|)}{\Big(\omega-s_n v_F(|\vec{k}+2\vec{q}|+|\vec{k}+\vec{q}|)+i\gamma\Big)\Big(s_n v_F(|\vec{k}+2\vec{q}|+|\vec{k}+\vec{q}|)\Big)}\right] \\
&\times s_n\left[(\eta_x-i\eta_y)e^{i\theta(\vec{k}+\vec{q})}-(\eta_x+i\eta_y)e^{-i\theta(\vec{k}+2\vec{q})}\right]\left[-(\eta_x-i\eta_y)e^{i\theta(\vec{k})}+(\eta_x+i\eta_y)e^{-i\theta(\vec{k}+\vec{q})}\right] \\
&\times \left[(\hat{x}+i\hat{y})e^{-i\theta(\vec{k})}+(\hat{x}-i\hat{y})e^{i\theta(\vec{k}+2\vec{q})}\right]. \qquad (6.31)
\end{aligned}$$

Expanding all the quantities to order $q$, this expression becomes

$$\begin{aligned}
\vec{J}^{2\omega} &= -g\frac{e^3}{2c^2\hbar^3}A_\omega^2\hbar\omega\frac{1}{(2\pi)^2}\frac{v_F^3}{2^3}\sum_{s_n}\int_0^\infty kdk\int_0^{2\pi}d\theta\frac{1}{2\omega}\left(1+\frac{s_n v_F q\cos\theta}{\omega}\right)\\
&\times\left[\frac{f(s_n,k)-f(-s_n,k)-q\cos\theta\frac{\partial f(-s_n,k)}{\partial k}}{(\omega+s_n v_F(2k+q\cos\theta)+i\gamma)\,(-s_n v_F(2k+q\cos\theta))}\right.\\
&\left.-\frac{f(-s_n,k)+q\cos\theta\frac{\partial f(-s_n,k)}{\partial k}-f(s_n,k)-2q\cos\theta\frac{\partial f(s_n,k)}{\partial k}}{(\omega-s_n v_F(2k+3q\cos\theta)+i\gamma)\,(s_n v_F(2k+3q\cos\theta))}\right]\\
&\times s_n\left[(\eta_x-i\eta_y)e^{i\theta}\left(1-i\frac{q}{k}\sin\theta\right)-(\eta_x+i\eta_y)e^{-i\theta}\left(1+2i\frac{q}{k}\sin\theta\right)\right]\\
&\times\left[-(\eta_x-i\eta_y)e^{i\theta}+(\eta_x+i\eta_y)e^{-i\theta}\left(1+i\frac{q}{k}\sin\theta\right)\right]\\
&\times\left[(\hat{x}+i\hat{y})e^{-i\theta}+(\hat{x}-i\hat{y})e^{i\theta}\left(1-2i\frac{q}{k}\sin\theta\right)\right]. \qquad (6.32)
\end{aligned}$$

There are linear in $q$ terms in the denominators which may not be expanded, since the other terms in the denominator can vanish. So, we will change the integration variable $k$ to treat this problem. Then, we need to integrate the two terms in [...] separately. Let's drop the coefficient and denote them as ① and ②. The first term is

$$\begin{aligned}
①\simeq&\int_0^{2\pi}d\theta\int_0^\infty(k-\frac{1}{2}q\cos\theta)dk\frac{1}{2\omega}\left(1+\frac{s_n v_F q\cos\theta}{\omega}\right)\\
&\times\frac{f(s_n,k)-\frac{1}{2}q\cos\theta\frac{\partial f(s_n,k)}{\partial k}-f(-s_n,k)-\frac{1}{2}q\cos\theta\frac{\partial f(-s_n,k)}{\partial k}}{(\omega+2s_n v_F k+i\gamma)\,(-2s_n v_F k)}\\
&\times s_n\left[(\eta_x-i\eta_y)e^{i\theta}\left(1-i\frac{q}{k}\sin\theta\right)-(\eta_x+i\eta_y)e^{-i\theta}\left(1+2i\frac{q}{k}\sin\theta\right)\right]\\
&\times\left[-(\eta_x-i\eta_y)e^{i\theta}+(\eta_x+i\eta_y)e^{-i\theta}\left(1+i\frac{q}{k}\sin\theta\right)\right]\\
&\times\left[(\hat{x}+i\hat{y})e^{-i\theta}+(\hat{x}-i\hat{y})e^{i\theta}\left(1-2i\frac{q}{k}\sin\theta\right)\right]. \qquad (6.33)
\end{aligned}$$

Here we only keep the terms of order $q$, and we are safe to keep the integration limit of $k$ unchanged, since the main contribution is from either around or larger than $k_F$.

Similarly, we can get the second term as

$$
\begin{aligned}
② \simeq & -\int_0^{2\pi} d\theta \int_0^{\infty} (k - \frac{3}{2} q\cos\theta) dk \frac{1}{2\omega}\left(1 + \frac{s_n v_F q\cos\theta}{\omega}\right) \\
& \times \frac{f(-s_n,k) - \frac{1}{2}q\cos\theta \frac{\partial f(-s_n,k)}{\partial k} - f(s_n,k) - \frac{1}{2}q\cos\theta\frac{\partial f(s_n,k)}{\partial k}}{(\omega - 2s_n v_F k + i\gamma)(2s_n v_F k)} \\
& \times s_n\left[(\eta_x - i\eta_y)e^{i\theta}\left(1 - i\frac{q}{k}\sin\theta\right) - (\eta_x + i\eta_y)e^{-i\theta}\left(1 + 2i\frac{q}{k}\sin\theta\right)\right] \\
& \times \left[-(\eta_x - i\eta_y)e^{i\theta} + (\eta_x + i\eta_y)e^{-i\theta}\left(1 + i\frac{q}{k}\sin\theta\right)\right] \\
& \times \left[(\hat{x} + i\hat{y})e^{-i\theta} + (\hat{x} - i\hat{y})e^{i\theta}\left(1 - 2i\frac{q}{k}\sin\theta\right)\right]. \qquad (6.34)
\end{aligned}
$$

Using Mathematica to integrate over $\theta$, we can find the term ① to order $q$:

$$
\begin{aligned}
① \simeq & \frac{\pi q}{4v_F\omega^2}\int_0^{\infty} dk \frac{(\omega + 2s_n v_F k)(f(-s_n,k) - f(s_n,k)) + \omega k\left(\frac{\partial f(-s_n,k)}{\partial k} + \frac{\partial f(s_n,k)}{\partial k}\right)}{k(\omega + 2s_n v_F k + i\gamma)} \\
& \times \left[(\eta_x^2 + 3\eta_y^2)\hat{x} - 2\eta_x\eta_y\hat{y}\right]. \qquad (6.35)
\end{aligned}
$$

Similarly, the term ② to order $q$ is

$$
\begin{aligned}
② \simeq & \frac{\pi q}{4v_F\omega^2}\int_0^{\infty} dk \frac{(\omega - 2s_n v_F k)(f(-s_n,k) - f(s_n,k)) + \omega k\left(\frac{\partial f(-s_n,k)}{\partial k} + \frac{\partial f(s_n,k)}{\partial k}\right)}{k(\omega - 2s_n v_F k + i\gamma)} \\
& \times \left[(\eta_x^2 + 3\eta_y^2)\hat{x} - 2\eta_x\eta_y\hat{y}\right]. \qquad (6.36)
\end{aligned}
$$

Then, we get

$$
\begin{aligned}
\sum_{s_n}(① + ②) &= \frac{\pi q}{v_F\omega}\left[(\eta_x^2 + 3\eta_y^2)\hat{x} - 2\eta_x\eta_y\hat{y}\right]\sum_{s_n}\int_0^{\infty} dk \frac{\left(\frac{\partial f(-1,k)}{\partial k} + \frac{\partial f(+1,k)}{\partial k}\right)}{(\omega + 2s_n v_F k + i\gamma)} \\
&= \frac{\pi q}{v_F\omega}\left[(\eta_x^2 + 3\eta_y^2)\hat{x} - 2\eta_x\eta_y\hat{y}\right]\sum_{s_n}\int_0^{\infty} dk \frac{-s(\epsilon_F)\delta(k - k_F)}{(\omega + 2s_n v_F k + i\gamma)} \\
&= -s(\epsilon_F)\frac{\pi q}{v_F\omega}\left[(\eta_x^2 + 3\eta_y^2)\hat{x} - 2\eta_x\eta_y\hat{y}\right]\frac{2\omega}{(\omega + i\gamma)^2 - 4v_F^2 k_F^2}. \qquad (6.37)
\end{aligned}
$$

Here $T \to 0$,is assumed, so $f(s,k) = \theta(s(\epsilon_F)k_F - sk)$. It contains $k_F$, but we will see if other types of combination of $s_m$, $s_n$ ans $s_l$ will cancel it.

**Type 2**: $s_m = s_l = -s_n$, so $\vec{J}^{2\omega}$ is given by

$$\begin{aligned}
\vec{J}^{2\omega} &= -g\frac{e^3}{2c^2\hbar^3}A_\omega^2\hbar\omega\frac{1}{(2\pi)^2}\frac{v_F^3}{2^3}\sum_{s_n}\int d^2\vec{k}\frac{1}{2\omega + s_n v_F(|\vec{k}+2\vec{q}|+|\vec{k}|)+i\gamma} \\
&\times \left[\frac{f(s_n,|\vec{k}|)-f(-s_n,|\vec{k}+\vec{q}|)}{\left(\omega+s_nv_F(|\vec{k}+\vec{q}|+|\vec{k}|)+i\gamma\right)\left(-s_nv_F(|\vec{k}+\vec{q}|+|\vec{k}|)\right)}\right. \\
&\left. - \frac{f(-s_n,|\vec{k}+\vec{q}|)-f(-s_n,|\vec{k}+2\vec{q}|)}{\left(\omega+s_nv_F(|\vec{k}+2\vec{q}|-|\vec{k}+\vec{q}|)+i\gamma\right)\left(-s_nv_F(|\vec{k}+2\vec{q}|-|\vec{k}+\vec{q}|)\right)}\right] \\
&\times s_n^3\left[-(\eta_x-i\eta_y)e^{i\theta(\vec{k}+\vec{q})}-(\eta_x+i\eta_y)e^{-i\theta(\vec{k}+2\vec{q})}\right]\left[-(\eta_x-i\eta_y)e^{i\theta(\vec{k})}+(\eta_x+i\eta_y)e^{-i\theta(\vec{k}+\vec{q})}\right] \\
&\times \left[-(\hat{x}+i\hat{y})e^{-i\theta(\vec{k})}+(\hat{x}-i\hat{y})e^{i\theta(\vec{k}+2\vec{q})}\right]. \qquad (6.38)
\end{aligned}$$

To the linear order in $q$, we first get

$$\begin{aligned}
\vec{J}^{2\omega} &= -g\frac{e^3}{2c^2\hbar^3}A_\omega^2\hbar\omega\frac{1}{(2\pi)^2}\frac{v_F^3}{2^3}\sum_{s_n}\int_0^\infty kdk\int_0^{2\pi}d\theta\frac{1}{2\omega+2s_nv_F(k+q\cos\theta)+i\gamma} \\
&\times \left[\frac{f(s_n,k)-f(-s_n,k)-q\cos\theta\frac{\partial f(-s_n,k)}{\partial k}}{(\omega+s_nv_F(2k+q\cos\theta)+i\gamma)\,(-s_nv_F(2k+q\cos\theta))}\right. \\
&\left. + \frac{\frac{\partial f(-s_n,k)}{\partial k}+\frac{3q}{2}\cos\theta\frac{\partial^2 f(-s_n,k)}{\partial k^2}}{(\omega+s_nv_Fq\cos\theta+i\gamma)\,(-s_nv_F)}\right] \\
&\times s_n\left[-(\eta_x-i\eta_y)e^{i\theta}\left(1-i\frac{q}{k}\sin\theta\right)-(\eta_x+i\eta_y)e^{-i\theta}\left(1+2i\frac{q}{k}\sin\theta\right)\right] \\
&\times \left[-(\eta_x-i\eta_y)e^{i\theta}+(\eta_x+i\eta_y)e^{-i\theta}\left(1+i\frac{q}{k}\sin\theta\right)\right] \\
&\times \left[-(\hat{x}+i\hat{y})e^{-i\theta}+(\hat{x}-i\hat{y})e^{i\theta}\left(1-2i\frac{q}{k}\sin\theta\right)\right]. \qquad (6.39)
\end{aligned}$$

As we did in type 1, the two terms are analyzed separately. Without the coefficient,

the first term is

$$
\begin{aligned}
① = & \int_0^\infty k dk \int_0^{2\pi} d\theta \frac{1}{2\omega + 2s_n v_F (k + q\cos\theta) + i\gamma} \\
& \times \frac{f(s_n,k) - f(-s_n,k) - q\cos\theta \frac{\partial f(-s_n,k)}{\partial k}}{(\omega + s_n v_F (2k + q\cos\theta) + i\gamma)(-s_n v_F 2k)} \left(1 - \frac{q}{2k}\cos\theta\right) \\
& \times s_n \left[ -(\eta_x - i\eta_y) e^{i\theta} \left(1 - i\frac{q}{k}\sin\theta\right) - (\eta_x + i\eta_y) e^{-i\theta} \left(1 + 2i\frac{q}{k}\sin\theta\right) \right] \\
& \times \left[ -(\eta_x - i\eta_y) e^{i\theta} + (\eta_x + i\eta_y) e^{-i\theta} \left(1 + i\frac{q}{k}\sin\theta\right) \right] \\
& \times \left[ -(\hat{x} + i\hat{y}) e^{-i\theta} + (\hat{x} - i\hat{y}) e^{i\theta} \left(1 - 2i\frac{q}{k}\sin\theta\right) \right] \\
& = \frac{-1}{2s_n v_F} \int_0^\infty dk \int_0^{2\pi} d\theta \left( f(s_n,k) - f(-s_n,k) - q\cos\theta \frac{\partial f(-s_n,k)}{\partial k} \right) \left(1 - \frac{q}{2k}\cos\theta\right) \\
& \times \frac{1}{\omega + s_n v_F q \cos\theta} \left( \frac{1}{\omega + s_n v_F (2k + q\cos\theta) + i\gamma} - \frac{1}{2\omega + 2s_n v_F (k + q\cos\theta) + i\gamma} \right) \\
& \times s_n \left[ -(\eta_x - i\eta_y) e^{i\theta} \left(1 - i\frac{q}{k}\sin\theta\right) - (\eta_x + i\eta_y) e^{-i\theta} \left(1 + 2i\frac{q}{k}\sin\theta\right) \right] \\
& \times \left[ -(\eta_x - i\eta_y) e^{i\theta} + (\eta_x + i\eta_y) e^{-i\theta} \left(1 + i\frac{q}{k}\sin\theta\right) \right] \\
& \times \left[ -(\hat{x} + i\hat{y}) e^{-i\theta} + (\hat{x} - i\hat{y}) e^{i\theta} \left(1 - 2i\frac{q}{k}\sin\theta\right) \right]. \qquad (6.40)
\end{aligned}
$$

In this form, we can change the integration variable $k$ for each of the two terms. The relevant factor becomes

$$
\left( f(s_n,k) - \frac{1}{2} q\cos\theta \frac{\partial f(s_n,k)}{\partial k} - f(-s_n,k) - \frac{1}{2} q\cos\theta \frac{\partial f(-s_n,k)}{\partial k} \right) \frac{1}{\omega + 2s_n v_F k + i\gamma} \qquad (6.41)
$$

$$
- \left( f(s_n,k) - q\cos\theta \frac{\partial f(s_n,k)}{\partial k} - f(-s_n,k) \right) \frac{1}{2\omega + 2s_n v_F k + i\gamma}. \qquad (6.42)
$$

Integrate over $\theta$, the result to order $q$ is

$$
\begin{aligned}
①|_x^{two} &= \int_0^\infty dk \frac{\pi q}{2v_F k\omega(\omega + 2s_n v_F k + i\gamma)(2\omega + 2s_n v_F k + i\gamma)} \\
&\times \left[ -\left(\eta_x^2(5\omega - 2s_n v_F k) + \eta_y^2(3\omega + 2s_n v_F k)\right)\left(f(-s_n,k) - f(s_n,k)\right)\right. \\
&\left. + (\eta_x^2 - \eta_y^2)k\left(-2(\omega + s_n v_F k)\frac{\partial f(-s_n,k)}{\partial k} + 2s_n v_F k \frac{\partial f(s_n,k)}{\partial k}\right)\right], \\
①|_y^{two} &= \int_0^\infty dk \frac{\eta_x\eta_y \pi q}{v_F k\omega(\omega + 2s_n v_F k + i\gamma)(2\omega + 2s_n v_F k + i\gamma)} \\
&\times \left[ -\left(\omega - 2s_n v_F k\right)\left(f(-s_n,k) - f(s_n,k)\right)\right. \\
&\left. + k\left(-2(\omega + s_n v_F k)\frac{\partial f(-s_n,k)}{\partial k} + 2s_n v_F k \frac{\partial f(s_n,k)}{\partial k}\right)\right].
\end{aligned} \tag{6.43}
$$

We will not evaluate the integration over $k$ at this time, we would like to see if some of the terms can be canceled. The second term is

$$
\begin{aligned}
② &= \int_0^\infty k dk \int_0^{2\pi} d\theta \frac{1}{2\omega + 2s_n v_F(k + q\cos\theta) + i\gamma} \\
&\times \frac{1}{(\omega + s_n v_F q\cos\theta + i\gamma)(-s_n v_F)}\left(\frac{\partial f(-s_n,k)}{\partial k} + \frac{3q}{2}\cos\theta\frac{\partial^2 f(-s_n,k)}{\partial k^2}\right) \\
&\times s_n\left[-(\eta_x - i\eta_y)e^{i\theta}\left(1 - i\frac{q}{k}\sin\theta\right) - (\eta_x + i\eta_y)e^{-i\theta}\left(1 + 2i\frac{q}{k}\sin\theta\right)\right] \\
&\times \left[-(\eta_x - i\eta_y)e^{i\theta} + (\eta_x + i\eta_y)e^{-i\theta}\left(1 + i\frac{q}{k}\sin\theta\right)\right] \\
&\times \left[-(\hat{x} + i\hat{y})e^{-i\theta} + (\hat{x} - i\hat{y})e^{i\theta}\left(1 - 2i\frac{q}{k}\sin\theta\right)\right] \\
&= \frac{-1}{s_n v_F}\int_0^{2\pi} d\theta \frac{1}{\omega}\left(1 - \frac{s_n v_F q}{\omega}\cos\theta\right)\int_0^\infty (k - q\cos\theta)dk \\
&\frac{1}{2\omega + 2s_n v_F k + i\gamma}\left(\frac{\partial f(-s_n,k)}{\partial k} + \frac{q}{2}\cos\theta\frac{\partial^2 f(-s_n,k)}{\partial k^2}\right) \\
&\times s_n\left[-(\eta_x - i\eta_y)e^{i\theta}\left(1 - i\frac{q}{k}\sin\theta\right) - (\eta_x + i\eta_y)e^{-i\theta}\left(1 + 2i\frac{q}{k}\sin\theta\right)\right] \\
&\times \left[-(\eta_x - i\eta_y)e^{i\theta} + (\eta_x + i\eta_y)e^{-i\theta}\left(1 + i\frac{q}{k}\sin\theta\right)\right] \\
&\times \left[-(\hat{x} + i\hat{y})e^{-i\theta} + (\hat{x} - i\hat{y})e^{i\theta}\left(1 - 2i\frac{q}{k}\sin\theta\right)\right].
\end{aligned} \tag{6.44}
$$

Integrate over $\theta$, and keep only terms to order $q$, we get

$$
\begin{aligned}
②|_x^{two} &= \frac{\pi q}{v_F\omega^2}\int_0^\infty dk \frac{1}{2\omega + 2s_n v_F k + i\gamma} \\
&\quad \times \left[\left(-2(\eta_x^2-\eta_y^2)s_n v_F k + 4(\eta_x^2+\eta_y^2)\omega\right)\frac{\partial f(-s_n,k)}{\partial k} + (\eta_x^2-\eta_y^2)k\omega\frac{\partial^2 f(-s_n,k)}{\partial k^2}\right], \\
②|_y^{two} &= \frac{2\eta_x\eta_y\pi q}{v_F\omega^2}\int_0^\infty k dk \frac{1}{2\omega + 2s_n v_F k + i\gamma}\left[-2s_n v_F\frac{\partial f(-s_n,k)}{\partial k} + \omega\frac{\partial^2 f(-s_n,k)}{\partial k^2}\right].
\end{aligned}
\tag{6.45}
$$

We will leave it like that at the moment.

**Type 3**: $s_n = s_l = -s_m$, so $\vec{J}^{2\omega}$ is given by

$$
\begin{aligned}
\vec{J}^{2\omega} &= -g\frac{e^3}{2c^2\hbar^3}A_\omega^2\hbar\omega\frac{1}{(2\pi)^2}\frac{v_F^3}{2^3}\sum_{s_n}\int d^2\vec{k}\frac{1}{2\omega + s_n v_F(|\vec{k}+2\vec{q}|+|\vec{k}|)+i\gamma} \\
&\times \left[\frac{f(s_n,|\vec{k}|)-f(s_n,|\vec{k}+\vec{q}|)}{\left(\omega - s_n v_F(|\vec{k}+\vec{q}|-|\vec{k}|)+i\gamma\right)\left(s_n v_F(|\vec{k}+\vec{q}|-|\vec{k}|)\right)}\right. \\
&\left. - \frac{f(s_n,|\vec{k}+\vec{q}|)-f(-s_n,|\vec{k}+2\vec{q}|)}{\left(\omega + s_n v_F(|\vec{k}+2\vec{q}|+|\vec{k}+\vec{q}|)+i\gamma\right)\left(-s_n v_F(|\vec{k}+2\vec{q}|+|\vec{k}+\vec{q}|)\right)}\right] \\
&\times s_n^3\left[-(\eta_x - i\eta_y)e^{i\theta(\vec{k}+\vec{q})} + (\eta_x+i\eta_y)e^{-i\theta(\vec{k}+2\vec{q})}\right]\left[(\eta_x-i\eta_y)e^{i\theta(\vec{k})} + (\eta_x+i\eta_y)e^{-i\theta(\vec{k}+\vec{q})}\right] \\
&\times \left[-(\hat{x}+i\hat{y})e^{-i\theta(\vec{k})} + (\hat{x}-i\hat{y})e^{i\theta(\vec{k}+2\vec{q})}\right].
\end{aligned}
\tag{6.46}
$$

To linear order in $q$, we first get

$$\begin{aligned}
\vec{J}^{2\omega} &= -g\frac{e^3}{2c^2\hbar^3}A_\omega^2\hbar\omega\frac{1}{(2\pi)^2}\frac{v_F^3}{2^3}\sum_{s_n}\int_0^\infty kdk\int_0^{2\pi}d\theta\frac{1}{2\omega+2s_nv_F(k+q\cos\theta)+i\gamma} \\
&\times\left[-\frac{\frac{\partial f(s_n,k)}{\partial k}+\frac{1}{2}q\cos\theta\frac{\partial^2 f(s_n,k)}{\partial k^2}}{(\omega-s_nv_Fq\cos\theta+i\gamma)\,(s_nv_F)}\right. \\
&\left.-\frac{f(s_n,k)+q\cos\theta\frac{\partial f(s_n,k)}{\partial k}-f(-s_n,k)-2q\cos\theta\frac{\partial f(-s_n,k)}{\partial k}}{(\omega+s_nv_F(2k+3q\cos\theta)+i\gamma)\,(-s_nv_F(2k+3q\cos\theta))}\right] \\
&\times s_n\left[-(\eta_x-i\eta_y)e^{i\theta}\left(1-i\frac{q}{k}\sin\theta\right)+(\eta_x+i\eta_y)e^{-i\theta}\left(1+2i\frac{q}{k}\sin\theta\right)\right] \\
&\times\left[(\eta_x-i\eta_y)e^{i\theta}+(\eta_x+i\eta_y)e^{-i\theta}\left(1+i\frac{q}{k}\sin\theta\right)\right] \\
&\times\left[-(\hat{x}+i\hat{y})e^{-i\theta}+(\hat{x}-i\hat{y})e^{i\theta}\left(1-2i\frac{q}{k}\sin\theta\right)\right]. \qquad (6.47)
\end{aligned}$$

Following the same method,

$$
\begin{aligned}
① = & \int_0^\infty k dk \int_0^{2\pi} d\theta \frac{1}{2\omega + 2s_n v_F(k + q\cos\theta) + i\gamma} \\
& \times \frac{f(s_n,k) + q\cos\theta \frac{\partial f(s_n,k)}{\partial k} - f(-s_n,k) - 2q\cos\theta \frac{\partial f(-s_n,k)}{\partial k}}{(\omega + s_n v_F(2k + 3q\cos\theta) + i\gamma)\,(s_n v_F 2k)} \left(1 - \frac{3q}{2k}\cos\theta\right) \\
& \times s_n \left[-(\eta_x - i\eta_y)e^{i\theta}\left(1 - i\frac{q}{k}\sin\theta\right) + (\eta_x + i\eta_y)e^{-i\theta}\left(1 + 2i\frac{q}{k}\sin\theta\right)\right] \\
& \times \left[(\eta_x - i\eta_y)e^{i\theta} + (\eta_x + i\eta_y)e^{-i\theta}\left(1 + i\frac{q}{k}\sin\theta\right)\right] \\
& \times \left[-(\hat{x} + i\hat{y})e^{-i\theta} + (\hat{x} - i\hat{y})e^{i\theta}\left(1 - 2i\frac{q}{k}\sin\theta\right)\right] \\
= & \frac{1}{2s_n v_F}\int_0^\infty dk \int_0^{2\pi} d\theta \left(f(s_n,k) + q\cos\theta\frac{\partial f(s_n,k)}{\partial k} - f(-s_n,k) - 2q\cos\theta\frac{\partial f(-s_n,k)}{\partial k}\right) \\
& \times \left(1 - \frac{3q}{2k}\cos\theta\right)\frac{1}{\omega - s_n v_F q\cos\theta} \\
& \times \left(-\frac{1}{2\omega + 2s_n v_F(k + q\cos\theta) + i\gamma} + \frac{1}{(\omega + s_n v_F(2k + 3q\cos\theta) + i\gamma)}\right) \\
& \times s_n \left[-(\eta_x - i\eta_y)e^{i\theta}\left(1 - i\frac{q}{k}\sin\theta\right) + (\eta_x + i\eta_y)e^{-i\theta}\left(1 + 2i\frac{q}{k}\sin\theta\right)\right] \\
& \times \left[(\eta_x - i\eta_y)e^{i\theta} + (\eta_x + i\eta_y)e^{-i\theta}\left(1 + i\frac{q}{k}\sin\theta\right)\right] \\
& \times \left[-(\hat{x} + i\hat{y})e^{-i\theta} + (\hat{x} - i\hat{y})e^{i\theta}\left(1 - 2i\frac{q}{k}\sin\theta\right)\right]. \qquad (6.48)
\end{aligned}
$$

Some of the factors can be written as

$$
\begin{aligned}
& - \left(f(s_n,k) - f(-s_n,k) - q\cos\theta\frac{\partial f(-s_n,k)}{\partial k}\right)\frac{1}{2\omega + 2s_n v_F k + i\gamma} \\
& + \left(f(s_n,k) - \frac{1}{2}q\cos\theta\frac{\partial f(s_n,k)}{\partial k} - f(-s_n,k) - \frac{1}{2}q\cos\theta\frac{\partial f(-s_n,k)}{\partial k}\right)\frac{1}{\omega + 2s_n v_F k + i\gamma}. \qquad (6.49)
\end{aligned}
$$

Integrating over $\theta$ and keeping the terms to order $q$, we obtain

$$
\begin{aligned}
①|_x^{three} &= \int_0^\infty dk \frac{\pi q}{2v_F k\omega(\omega + 2s_n v_F k + i\gamma)(2\omega + 2s_n v_F k + i\gamma)} \\
&\times \left[ \left(\eta_x^2(5\omega - 2s_n v_F k) + \eta_y^2(3\omega + 2s_n v_F k)\right) \left(f(-s_n,k) - f(s_n,k)\right) \right. \\
&\left. + (\eta_x^2 - \eta_y^2)k \left( 2s_n v_F k \frac{\partial f(-s_n,k)}{\partial k} - 2(\omega + s_n v_F k)\frac{\partial f(s_n,k)}{\partial k} \right) \right], \\
①|_y^{three} &= \int_0^\infty dk \frac{\eta_x \eta_y \pi q}{v_F k\omega(\omega + 2s_n v_F k + i\gamma)(2\omega + 2s_n v_F k + i\gamma)} \\
&\times \left[ (\omega - 2s_n v_F k) \left(f(-s_n,k) - f(s_n,k)\right) \right. \\
&\left. + k \left( 2s_n v_F k \frac{\partial f(-s_n,k)}{\partial k} - 2(\omega + s_n v_F k)\frac{\partial f(s_n,k)}{\partial k} \right) \right].
\end{aligned} \tag{6.50}
$$

The second term can be written as

$$
\begin{aligned}
② &= -\int_0^\infty k dk \int_0^{2\pi} d\theta \frac{1}{2\omega + 2s_n v_F(k + q\cos\theta) + i\gamma} \\
&\times \frac{\frac{\partial f(s_n,k)}{\partial k} + \frac{1}{2}q\cos\theta \frac{\partial^2 f(s_n,k)}{\partial k^2}}{\left(\omega - s_n v_F q\cos\theta + i\gamma\right)\left(s_n v_F\right)} \\
&\times s_n \left[ -(\eta_x - i\eta_y)e^{i\theta}\left(1 - i\frac{q}{k}\sin\theta\right) + (\eta_x + i\eta_y)e^{-i\theta}\left(1 + 2i\frac{q}{k}\sin\theta\right) \right] \\
&\times \left[ (\eta_x - i\eta_y)e^{i\theta} + (\eta_x + i\eta_y)e^{-i\theta}\left(1 + i\frac{q}{k}\sin\theta\right) \right] \\
&\times \left[ -(\hat{x} + i\hat{y})e^{-i\theta} + (\hat{x} - i\hat{y})e^{i\theta}\left(1 - 2i\frac{q}{k}\sin\theta\right) \right] \\
&= -\frac{1}{s_n v_F}\int_0^{2\pi} d\theta \int_0^\infty (k - q\cos\theta) dk \frac{1}{\omega}\left(1 + \frac{s_n v_F q}{\omega}\cos\theta\right) \\
&\times \left( \frac{\partial f(s_n,k)}{\partial k} - \frac{1}{2}q\cos\theta\frac{\partial^2 f(s_n,k)}{\partial k^2} \right) \frac{1}{2\omega + 2s_n v_F k + i\gamma} \\
&\times s_n \left[ -(\eta_x - i\eta_y)e^{i\theta}\left(1 - i\frac{q}{k}\sin\theta\right) + (\eta_x + i\eta_y)e^{-i\theta}\left(1 + 2i\frac{q}{k}\sin\theta\right) \right] \\
&\times \left[ (\eta_x - i\eta_y)e^{i\theta} + (\eta_x + i\eta_y)e^{-i\theta}\left(1 + i\frac{q}{k}\sin\theta\right) \right] \\
&\times \left[ -(\hat{x} + i\hat{y})e^{-i\theta} + (\hat{x} - i\hat{y})e^{i\theta}\left(1 - 2i\frac{q}{k}\sin\theta\right) \right].
\end{aligned} \tag{6.51}
$$

Integrating over $\theta$ and keeping only the terms to order $q$, we get

$$\begin{aligned}
②|_x^{three} &= \frac{\pi q}{v_F\omega^2}\int_0^\infty dk \frac{1}{2\omega + 2s_n v_F k + i\gamma} \\
&\times \left[\left(-2(\eta_x^2-\eta_y^2)s_n v_F k + 4(\eta_x^2+\eta_y^2)\omega\right)\frac{\partial f(s_n,k)}{\partial k} + (\eta_x^2-\eta_y^2)k\omega\frac{\partial^2 f(s_n,k)}{\partial k^2}\right], \\
②|_y^{three} &= \frac{2\eta_x\eta_y\pi q}{v_F\omega^2}\int_0^\infty kdk \frac{1}{2\omega + 2s_n v_F k + i\gamma}\left[-2s_n v_F\frac{\partial f(s_n,k)}{\partial k} + \omega\frac{\partial^2 f(s_n,k)}{\partial k^2}\right].
\end{aligned} \tag{6.52}$$

**Sum over types 2 and 3.** As we can see, the results from types 2 and 3 are very similar. Summing them over, we get

$$\begin{aligned}
\sum_{s_n}\left(①_x^{two} + ①_x^{three}\right) &= (\eta_x^2-\eta_y^2)(-\frac{\pi q}{v_F})\sum_{s_n}\int_0^\infty dk \frac{1}{(\omega + 2s_n v_F k + i\gamma)(2\omega + 2s_n v_F k + i\gamma)} \\
&\times\left(\frac{\partial f(-s_n,k)}{\partial k} + \frac{\partial f(s_n,k)}{\partial k}\right) \\
&= (\eta_x^2-\eta_y^2)s(\epsilon_F)\frac{\pi q}{v_F}\sum_{s_n}\frac{1}{(\omega + 2s_n v_F k_F + i\gamma)(2\omega + 2s_n v_F k_F + i\gamma)},
\end{aligned} \tag{6.53}$$

and

$$\begin{aligned}
\sum_{s_n}\left(①_y^{two} + ①_y^{three}\right) &= -2\eta_x\eta_y\frac{\pi q}{v_F}\sum_{s_n}\int_0^\infty dk \frac{1}{(\omega + 2s_n v_F k + i\gamma)(2\omega + 2s_n v_F k + i\gamma)} \\
&\times\left(\frac{\partial f(-s_n,k)}{\partial k} + \frac{\partial f(s_n,k)}{\partial k}\right) \\
&= 2\eta_x\eta_y s(\epsilon_F)\frac{\pi q}{v_F}\sum_{s_n}\frac{1}{(\omega + 2s_n v_F k_F + i\gamma)(2\omega + 2s_n v_F k_F + i\gamma)},
\end{aligned} \tag{6.54}$$

and

$$\sum_{s_n}\left(②_x^{two}+②_x^{three}\right)=\frac{\pi q}{v_F\omega^2}\sum_{s_n}\int_0^\infty dk\frac{1}{2\omega+2s_nv_Fk+i\gamma}$$
$$\times\left[\left(-2(\eta_x^2-\eta_y^2)s_nv_Fk+4(\eta_x^2+\eta_y^2)\omega\right)\left(\frac{\partial f(-s_n,k)}{\partial k}+\frac{\partial f(s_n,k)}{\partial k}\right)\right.$$
$$\left.+\,(\eta_x^2-\eta_y^2)k\omega\left(\frac{\partial^2 f(-s_n,k)}{\partial k^2}+\frac{\partial^2 f(s_n,k)}{\partial k^2}\right)\right]$$
$$=-\frac{\pi q}{v_F\omega^2}s(\epsilon_F)\sum_{s_n}\left[\frac{-2(\eta_x^2-\eta_y^2)s_nv_Fk_F+4(\eta_x^2+\eta_y^2)\omega}{2\omega+2s_nv_Fk_F+i\gamma}\right.$$
$$\left.-\,(\eta_x^2-\eta_y^2)\omega\frac{2\omega}{(2\omega+2s_nv_Fk_F+i\gamma)^2}\right],\qquad(6.55)$$

and

$$\sum_{s_n}\left(②_y^{two}+②_y^{three}\right)=\frac{2\eta_x\eta_y\pi q}{v_F\omega^2}\sum_{s_n}\int_0^\infty kdk\frac{1}{2\omega+2s_nv_Fk+i\gamma}$$
$$\left[-2s_nv_F\left(\frac{\partial f(-s_n,k)}{\partial k}+\frac{\partial f(s_n,k)}{\partial k}\right)+\omega\left(\frac{\partial^2 f(-s_n,k)}{\partial k^2}+\frac{\partial^2 f(s_n,k)}{\partial k^2}\right)\right]$$
$$=-\frac{2\eta_x\eta_y\pi q}{v_F\omega^2}s(\epsilon_F)\sum_{s_n}\left[(-2s_nv_F)\frac{k_F}{2\omega+2s_nv_Fk+i\gamma}\right.$$
$$\left.-\,\omega\frac{2\omega}{(2\omega+2s_nv_Fk_F+i\gamma)^2}\right].\qquad(6.56)$$

Now we have essentially everything to calculate the magnitude and polarization dependence of the SH signal in graphene.

## 6.6 Theoretical Results and Discussion

For definiteness, we assume that the Fermi level is in the conduction band, and $\omega\gg v_Fk_F$. Then the contribution of $\vec{J}^{2\omega}$ from interband processes is (the coefficient $-g\frac{e^3}{2c^2\hbar^3}A_\omega^2\hbar\omega\frac{1}{(2\pi)^2}\frac{v_F^3}{2^3}$ is dropped):

Type 1:

$$\frac{\pi q}{v_F \omega^2}\left(-2\eta_x^2 - 6\eta_y^2,\ 4\eta_x\eta_y\right). \tag{6.57}$$

Type 2 and type 3:

$$\frac{\pi q}{v_F \omega^2}\left(-2\eta_x^2 - 6\eta_y^2,\ 4\eta_x\eta_y\right). \tag{6.58}$$

We recall that the intraband contribution is

$$\frac{\pi q}{v_F \omega^2}\left(3\eta_x^2 + \eta_y^2,\ 2\eta_x\eta_y\right). \tag{6.59}$$

So, the total is

$$\frac{\pi q}{v_F \omega^2}\left(-\eta_x^2 - 11\eta_y^2,\ 10\eta_x\eta_y\right). \tag{6.60}$$

Adding the coefficient, and using $E_\omega = i\omega A_\omega/c$, we can get an equation like $\vec{J}^{2\omega} = \sigma^{2\omega} E_\omega^2$, where $\sigma^{2\omega}$ is the SHG optical conductivity, and it is given by

$$\sigma^{(2)}(2\omega) = \frac{e^3 v_F^2 q}{16\pi\hbar^2\omega^3}\left[(-\eta_x^2 - 11\eta_y^2)\hat{x} + 10\eta_x\eta_y\hat{y}\right]. \tag{6.61}$$

This result is consistent with the experiment as it shows that the S-polarized incident field $\eta_x = 0$, $\eta_y = 1$ generates the SH signal which is more than 100 times stronger than the P-polarized incident field $\eta_x = 1$, $\eta_y = 0$.

For completeness, we will get the relation between the intensities of fundamental light and SH light. Since the graphene layers are put on a substrate, the fundamental light is reflected on the interface between air and substrate. The electric field

contributing to the SHG process is the summation of the in-plane components of the incident field and reflected field. This is shown in Fig. 6.4. On the other hand, the current $J_{2\omega}$ can radiate optical fields into both the air and the substrate, as shown in Fig. 6.5. So, we also need to find the relation between the fields and the current.

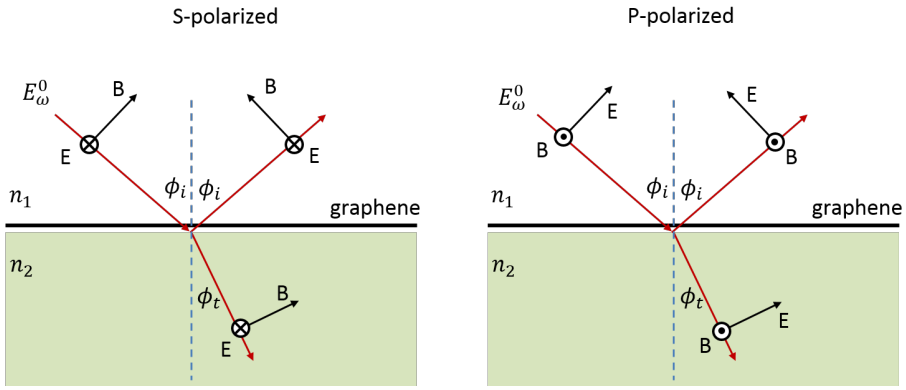


Figure 6.4: The geometry of the incident fundamental light. The incident and refractive angles are labeled by $\phi_i$ and $\phi_t$, respectively. The electric field at the graphene layer can be related to the incident fundamental light by the boundary conditions between two dielectric materials. Only the inplane electric field contributes to the SHG processes.

Define some notations: $n_1$: refractive index of the air; $n_2$: refractive index of the substrate; $\phi_i$: incident angle; $\phi_t$: refractive angle; $E_\omega^0$: amplitude of the fundamental light; $E_{2\omega}^1$: amplitude of the SH light in the air; $E_{2\omega}^2$: amplitude of the SH light in the substrate. If we ignore the effect of graphene on reflection and refraction, then we have the relation $n_1 \sin\phi_i = n_2 \sin\phi_t$. Using the boundary conditions, we have

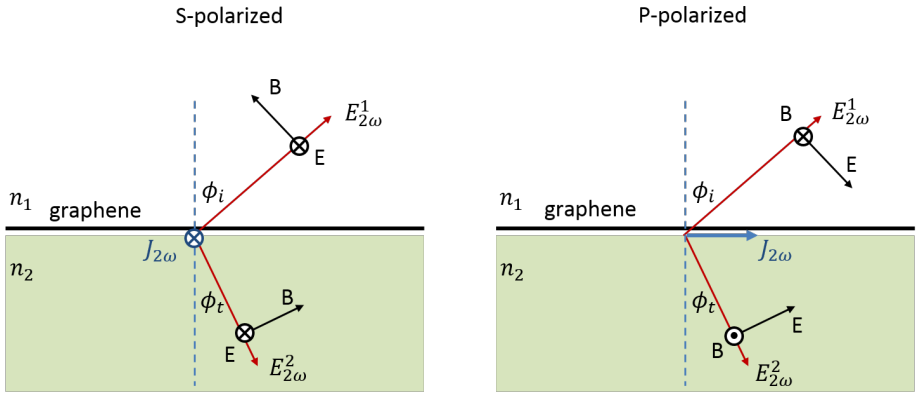


Figure 6.5: The geometry of the radiated SHG light. $\phi_i$ and $\phi_t$ are the incident and refractive angles for the fundamental light. The radiation goes into both the air ($E^1_{2\omega}$) and the substrate ($E^2_{2\omega}$). They can be related to $J_{2\omega}$ by the standard boundary conditions. If we assume the refractive indices at the fundamental and SH frequencies are the same, then the direction of radiated field is the same as the reflected or refracted fundamental light.

the in-plane electric field of the fundamental light as

$$\begin{aligned} \text{S-pol.}: \quad & E^0_\omega \frac{2n_1 \cos\phi_i}{n_1 \cos\phi_i + n_2 \cos\phi_t}, \\ \text{P-pol.}: \quad & E^0_\omega \frac{2n_1 \cos\phi_i \cos\phi_t}{n_1 \cos\phi_t + n_2 \cos\phi_i}. \end{aligned} \tag{6.62}$$

Also, we can get the relations between $J_{2\omega}$ and $E_{2\omega}$ as

$$\begin{aligned} \text{S-pol.}: \quad E^1_{2\omega} &= -\frac{1}{n_1 \cos\phi_i + n_2 \cos\phi_t} \frac{4\pi}{c} J_{2\omega}, \\ E^2_{2\omega} &= E^1_{2\omega}, \\ \text{P-pol.}: \quad E^1_{2\omega} &= -\frac{\cos\phi_t}{n_1 \cos\phi_t + n_2 \cos\phi_i} \frac{4\pi}{c} J_{2\omega}, \\ E^2_{2\omega} &= -\frac{\cos\phi_i}{n_1 \cos\phi_t + n_2 \cos\phi_i} \frac{4\pi}{c} J_{2\omega}. \end{aligned} \tag{6.63}$$

Here the the direction of the electric field is chosen in the way that it has a component

in the direction of $\vec{J}_{2\omega}$. These effects are considered in measuring the SHG optical conductivity, so the experimental results are directly compared with Eq. 6.61.

The coefficient in Eq. 6.61 has a value of $3.12 \times 10^{-18} S \cdot m/V$, so the SHG optical conductivity for $S \rightarrow P$ is $3.4 \times 10^{-17} S \cdot m/V$. The measured value is $1.4 \times 10^{-17} S \cdot m/V$. So, the calculated value is about 2.4 times the measured one. Considering some uncounted effects in the measurement, we think the agreement between theory and experiment is acceptable. Most importantly, the polarization dependence is explained by our theory. Also, our result shows that if the fundamental light has polarization which is neither parallel nor perpendicular to the incident plane, then S-polarized SH light can also be generated.

The reason SHG processes can happen in graphene is because the fundamental light is incident on the graphene plane obliquely, so the q vector breaks the inversion symmetry. We also see that only P-polarized SH light can be generated when the fundamental field is either S- or P-polarized, this is because there is still a reflection symmetry in the direction perpendicular to the incident plane. If the fundamental light is neither S- nor P-polarized, then this reflection symmetry is also broken, and S-polarized SH light can also be generated. Also, we see S-polarized fundamental light can generate P-polarized SH light, this is due to the selection rules for circularly polarized light.

The inversion symmetry in graphene can also be broken by other mechanisms. For example, SHG in graphene is achieved by introducing a direct electric current [54]. In these cases, the SHG processes can happen to the zeroth order of $q$.

## 6.7 Conclusion

The SHG susceptibility is measured by Dr. Heinz's group. In the experiment, fundamental light is incident on the graphene layer obliquely, and SHG light is col-

lected in the reflected geometry. The SHG susceptibility is found to be dominant when the fundamental light is S-polarized, and SH light is P-polarized. The theoretical calculation based on quantum mechanical model shows the SHG susceptibility for S $\rightarrow$ P is 11 times the P $\rightarrow$ P one, while S-polarized SH light cannot be generated if the fundamental light is either S- or P-polarized. These agree with the experimental observations. When fundamental light it neither S- nor P-polarized, S-polarized SH light can also be generated. The reason for SHG processes to happen in graphene is because the inversion symmetry is broken due to the $q$ vector of the obliquely incident light. For SHG processes to happen at zeroth order of $q$, other mechanism to break the inversion symmetry should be explored.

# 7. SUMMARY

In this dissertation, the optical properties of QW structures and single-layer graphene are studied. In QW structures, we specially investigated the effects of Coulomb interaction between carriers. In optically excited electron-hole magneto-plasma, delayed burst of optical pulses (Superfluorescence) has been observed. The time and energy-resolved measurement shows that the center frequency of the pulse decreases with time. In order to explain it, we developed a generalized semiconductor Bloch equations, and show that the maximum gain occurs at the Fermi edges for electron-hole plasma in quasi-equilibrium. When the carriers are recombined into photons, the Fermi energies of both electrons and holes decrease, so the photon energy also decreases. This explains the red-shifting of the center frequency of pulse.

Coulomb interaction can also affects intersubband optical transitions. We developed a theoretical framework to study the effect of Coulomb interaction on second-order nonlinear optical processes. We show that the DFG susceptibility is enhanced by the intersubband plasmonic effect. This can help optimizing the design of devices for second-order nonlinear processes.

QCLs are devices composed by many QWs, and they are an important kind of mid-IR sources. We showed that pulse can be generated by active modulation in mid-IR QCLs with vertical optical transition, where the lifetime of upper laser state is $\sim$1 ps. We show that active modulation of QCLs with short gain recovery time is more robust than long gain recovery time. By tuning the modulation period, mode-locked pulses can be achieved too.

When single-layer graphene is under a transverse magnetic field, its linear band is discretized into Landau levels, the energy separations between neighboring LLs are

unequal, and the optical selection rules are unique. We utilized these properties to propose a scheme for continuous-wave lasing between graphene LLs, where infrared pumping can lead to THz gain. In the proposed scheme, coupling of electrons to the SO phonons from the substrate is utilized to efficiently populate the upper laser state. If a cavity is introduced, THz lasing can be achieved for mirrors with reflectivity that can be easily fabricated.

We also studied the SHG in graphene, inspired by experimental observations. The experiment shows the SHG susceptibility is dominant for fundamental light with S-polarization, and second-harmonic light with P-polarization. We developed a quantum theory which can explain this. We found that the contributions for SHG are from two channels. In one of them only intraband transitions are involved, and the other one contains both intraband and interband transitions. The amplitudes from those two contributions are added, and this addition can be either constructive or destructive, depending on the polarization configurations. The result shows that the optical conductivity for S $\rightarrow$ P is 11 times larger than P $\rightarrow$ P, and S-polarized SH light cannot be generated if fundamental light is either S or P-polarized. However, S-polarized SH light can still be generated if the electric field of fundamental light is neither parallel nor perpendicular to the incident plane.

REFERENCES


[1] T. Ando, A. B. Fowler, and F. Stern, Rev. Mod. Phys. **54**, 437 (1982).

[2] E. Rosencher and B. Vinter, *Optoelectronics* (Cambridge University Press, Cambridge, UK, 2002).

[3] R. F. Kazarinov and R. A. Suris, Soviet Physics Semiconductors-USSR **6**, 120 (1972).

[4] J. Faist *et al.*, Science **264**, 553 (1994).

[5] Y. Yao, A. J. Hoffman, and C. F. Gmachl, Nature Photonics **6**, 432 (2012).

[6] W. E. Lamb, Phys. Rev. **134**, A1429 (1964).

[7] V.-M. Gkortsas *et al.*, Opt. Express **18**, 13616 (2010).

[8] A. H. Castro Neto, F. Guinea, N. M. R. Peres, K. S. Novoselov, and A. K. Geim, Rev. Mod. Phys. **81**, 109 (2009).

[9] R. H. Dicke, Phys. Rev. **93**, 99 (1954).

[10] N. Skribanowitz, I. P. Herman, J. C. MacGillivray, and M. S. Feld, Phys. Rev. Lett. **30**, 309 (1973).

[11] G. T. Noe II *et al.*, Nature Physics **8**, 219 (2012).

[12] Y. D. Jho *et al.*, Phys. Rev. Lett. **96**, 237401 (2006).

[13] Y. D. Jho *et al.*, Phys. Rev. B **81**, 155314 (2010).

[14] Y. D. Jho *et al.*, Phys. Rev. B **72**, 045340 (2005).

[15] H. Haug and S. Koch, *Quantum Theory of the Optical and Electronic Properties of Semiconductors* (World Scientific, Singapore, 2009).

[16] F. Vasko and A. Kuznetsov, *Electronic States and Optical Transitions in Semiconductor Heterostructures* (Springer, New York, 1999).

[17] E. Anderson *et al.*, *LAPACK Users' Guide*, Third ed. (Society for Industrial and Applied Mathematics, Philadelphia, PA, 1999).

[18] I. Vurgaftman, J. R. Meyer, and L. R. Ram-Mohan, Journal of Applied Physics **89**, 5815 (2001).

[19] M. Sugawara, N. Okazaki, T. Fujii, and S. Yamazaki, Phys. Rev. B **48**, 8102 (1993).

[20] M. S. Skolnick *et al.*, Phys. Rev. Lett. **58**, 2130 (1987).

[21] L. Wendler and E. Kndler, Physica Status Solidi (b) **177**, 9 (1993).

[22] A. Delteil *et al.*, Phys. Rev. Lett. **109**, 246808 (2012).

[23] G. Pegolotti, A. Vasanelli, Y. Todorov, and C. Sirtori, Phys. Rev. B **90**, 035305 (2014).

[24] S. Barbieri *et al.*, Nat. Photonics **5**, 306 (2011).

[25] J. Freeman *et al.*, Appl. Phys. Lett. **101**, 181115 (2012).

[26] C. Y. Wang *et al.*, Opt. Express **17**, 12929 (2009).

[27] A. Gordon *et al.*, Phys. Rev. A **77**, 053804 (2008).

[28] A. K. Wójcik *et al.*, Appl. Phys. Lett. **103**, (2013).

[29] R. Terazzi, T. Gresch, A. Wittmann, and J. Faist, Phys. Rev. B **78**, 155328 (2008).

[30] G. Nusinovich, *Introduction to the Physics of Gyrotrons* (Johns Hopkins University Press, Baltimore, MD, 2004).

[31] H. Aoki, Applied Physics Letters **48**, 559 (1986).

[32] A. Wade *et al.*, Nature Photonics **3**, 41 (2008).

[33] Y. B. Vasil'ev and Y. L. Ivanov, Sov. Tech. Phys. Lett. **10**, 398 (1984).

[34] K. Unterrainer *et al.*, Phys. Rev. Lett. **64**, 2277 (1990).

[35] T. Morimoto, Y. Hatsugai, and H. Aoki, Phys. Rev. B **78**, 073406 (2008).

[36] F. Wendler, A. Knorr, and E. Malic, Nature communications **5**, 3703 (2014).

[37] M. Mittendorff *et al.*, Nature Physics **11**, 75 (2014).

[38] F. Wendler and E. Malic, ArXiv e-prints (2014), 1410.2080.

[39] P. Cheng *et al.*, Phys. Rev. Lett. **105**, 076801 (2010).

[40] Y. Jiang *et al.*, Phys. Rev. Lett. **108**, 016401 (2012).

[41] X. Yao, M. Tokman, and A. Belyanin, Opt. Express **23**, 795 (2015).

[42] V. Ryzhii, M. Ryzhii, and T. Otsuji, Journal of Applied Physics **101**, (2007).

[43] U. Stberl, U. Wurstbauer, W. Wegscheider, D. Weiss, and J. Eroms, Applied Physics Letters **93**, (2008).

[44] L. H. Dubois and G. P. Schwartz, Phys. Rev. B **26**, 794 (1982).

[45] M. Orlita *et al.*, Phys. Rev. Lett. **101**, 267601 (2008).

[46] M. O. Goerbig, Rev. Mod. Phys. **83**, 1193 (2011).

[47] Y. Zheng and T. Ando, Phys. Rev. B **65**, 245420 (2002).

[48] D. S. L. Abergel and V. I. Fal'ko, Phys. Rev. B **75**, 155430 (2007).

[49] W. Nolting and W. Brewer, *Fundamentals of Many-body Physics: Principles and Methods* (Springer, Berlin, 2009).

[50] A. Tomadin, D. Brida, G. Cerullo, A. C. Ferrari, and M. Polini, Phys. Rev. B **88**, 035430 (2013).

[51] J. K. Viljas and T. T. Heikkilä, Phys. Rev. B **81**, 245404 (2010).

[52] N. Mori and T. Ando, Phys. Rev. B **40**, 6175 (1989).

[53] L. A. Falkovsky and A. A. Varlamov, The European Physical Journal B **56**, 281 (2007).

[54] A. Y. Bykov, T. V. Murzina, M. G. Rybin, and E. D. Obraztsova, Phys. Rev. B **85**, 121413 (2012).